Tuning the Low-Energy Physics in Kitaev Magnets

Faranak Bahrami

A dissertation

submitted to the Faculty of

the department of Physics

in partial fulfillment

of the requirements

for the degree of

Doctor of Philosophy

Boston College

Morrissey College of Arts and Sciences

Graduate School

May 2023

Tuning the Low-Energy Physics in Kitaev Magnets

Faranak Bahrami

Advisor: Fazel Tafti, Ph.D.

The search for an ideal quantum spin-liquid (QSL) material which can host a QSL ground state as well as exotic excitations has been one of the leading research topics in condensed matter physics over the past few decades. Out of all the proposals to realize the physics of a QSL, the Kitaev model is the most promising proposal with a QSL ground state. The Kitaev Hamiltonian is exactly solvable via fractionalization of its spin degrees of freedom into Majorana excitations, and it can be engineered in real materials. Among all the proposed Kitaev candidates, α-Li$_2$IrO$_3$, Na$_2$IrO$_3$, Li$_2$RhO$_3$, and α-RuCl$_3$ are the most promising candidates. During my Ph.D. research I explored new physics related to Kitaev materials via modification of the symmetry and structural properties of these known Kitaev candidates.

First, I studied how modification of the inter-layer chemistry can alter the thermodynamic properties of Kitaev candidate α-Li$_2$IrO$_3$ via an enhancement of the spin-orbit coupling (SOC) effect. The light, octahedrally-coordinated inter-layer Li atoms are replaced with heavier, linearly-coordinated Ag atoms to synthesize Ag$_3$LiIr$_2$O$_6$. In addition to these structural modifications to the parent compound α-Li$_2$IrO$_3$, having heavier elements between the honeycomb layers in the Ag compound increased the effect of SOC in the honeycomb layers and led to a decrease in the long-range ordering temperature in Ag$_3$LiIr$_2$O$_6$ compared to its parent compound.

Second, I studied the effect of local crystal distortion in the presence of a weak SOC effect to explore a new spin-orbital state different from the $J_{\text{eff}} = \frac{1}{2}$ state.

Based on theoretical predictions, the ground states of Kitaev materials can be tuned to other exotic spin-orbital states such as an Ising spin-1/2 state. To provide the proper conditions for a competition between the trigonal crystal distortion and the SOC effect, I modified the crystal environment around the magnetic elements in the parent compound Li_2RhO_3 via a topo-chemical method and synthesized $Ag_3LiRh_2O_6$. An increase in the strength of trigonal distortion in $Ag_3LiRh_2O_6$, in the presence of weak SOC, led to a transition from the $J_{\text{eff}} = \frac{1}{2}$ ground state (Kitaev limit) in the parent compound to an Ising spin-1/2 ground state (Ising limit) in the product. This change in spin-orbital state resulted in a dramatic change in magnetic behavior. Whereas Li_2RhO_3 shows a spin-freezing transition at 6 K, $Ag_3LiRh_2O_6$ reveals a robust long-range antiferromagnetic transition at 94 K. This is the first realization of a change of ground state between the Kitaev and Ising limits in the same structural family.

Lastly, I studied how the crystal symmetry can be an important factor in the physics of Kitaev materials. Honeycomb layered materials can be crystallized in space groups $C2/m$, $C2/c$, and $P6_322$. However, the crystal symmetry of most Kitaev candidates is described by the $C2/m$ space group. We successfully synthesized a polymorph of a $3d$ Kitaev candidate, hexagonal $Na_2Co_2TeO_6$ ($P6_322$ space group) in space group $C2/m$. The change in crystal symmetry of this cobalt tellurate replaced three anti-ferromagnetic (AFM) orders at 27, 15, 7 K in the hexagonal polymorph by a single AFM peak at 9.6 K in the monoclinic $Na_2Co_2TeO_6$.

TABLE OF CONTENTS

LIST OF FIGURES

LIST OF TABLES

LIST OF ABBREVIATIONS

AFM anti-ferromagnetic

FM ferromagnetic

ZFC zero-field-cooled

FC field-cooled

CEF crystal electric field

CW Curie-Weiss

ED electron diffraction

HAADF-STEM high-angle annular dark-field scanning transmission electron microscopy

ABF-STEM annular bright-field scanning transmission electron microscopy

PSI Paul Scherrer Institute

PXRD powder x-ray diffraction

XRD x-ray diffraction

XAS x-ray absorption spectroscopy

QMC quantum Monte Carlo

QSL quantum spin-liquid

SOC spin-orbit coupling

TEM transmission electron microscopy

DFT density functional theory

CIF crystallographic information file

NC norm-conserving

PBE Perdew-Burke-Ernzerhof

PZ Perdew-Zunger

XANES x-ray absorption near edge structure

TEY total electron yield

PFY partial fluorescence yield

FT Fourier transform

VRH variable range hopping

ZF zero-field

LF longitudinal field

NMR nuclear magnetic resonance

GPS General Purpose Surface-Muon

DOS density of states

LDA local density approximation

MPMS3 Magnetic Property Measurement System

SQUID superconducting quantum interference device

PPMS Physical Property Measurement System

EDX energy dispersive x-ray

RVB resonating valence-bond

NN nearest-neighbour

TOF time-of-flight

NPD neutron powder diffraction

ACKNOWLEDGEMENTS

I would like to dedicate my dissertation to my wonderful grandparents, Nader Jahangiri and Shirin Foroutan, and my amazing parents Noorali Bahrami and Behnaz Jahangiri. I deeply appreciate all of their support and their belief in me from childhood until now. We have been far from each other for almost six years, but they have been always my biggest supporters through the ups and downs in my life. I would also like to thank my lovely sisters, Flora, Roshanak, and Rayka for being my best friends. I really appreciate you for always helping me to move forward, even during the most challenging times in my life. I love you all so much!

I would like to thank my advisor Professor Fazel Tafti for helping me to become an experimentalist, and more than that, a better scientist. I learned a lot from him and I will always remember that. I always appreciated his enthusiasm for solving scientific challenges. I am grateful for having received the opportunity to be a mentor in his lab and trained several graduate and undergraduate students. I would also like to thank my committee members, Professor Michael Graf, Professor Natalia Perkins, and Professor Kenneth Burch for agreeing to be part of this important event in my life. I was lucky that Professor Graf was my academic advisor during my Ph.D. program and I had great support from an amazing mentor. I will always remember this pleasant memory after my Research Proposal Exam, when he told me to always try to enjoy presenting the results of your hard work instead of being worried about unimportant points. I am also very grateful for having a very successful and amazing female scientist, Professor Perkins, in

my committee, whom I had the honor of hearing acknowledge the completion of my Ph.D. degree from. I would also like to thank Professor Burch for being very supportive during my Ph.D. at Boston College. One time I had the chance to attend one of his group meetings, and I really appreciate him for respecting me and valuing my opinion.

To my best friend, great partner, and wonderful physicist, Gavin B. Osterhoudt: I really appreciate your endless support and help during my Ph.D. and I am really happy that we found each other at Boston College. I would also like to thank Lori Barnes and Jim Clark for being great friends and supporting me. Thank you to them for being with me during my Ph.D. defense and for making the absence of my parents easier for me. I would also like to thank Jerry Osterhoudt for his support, his kindness, and his humor. I should also thank our annoying pet birds, Tonic and JoJo, for waking me up every morning.

The Boston College physics department is like a second home to me, and I love every single person that I met there. I would especially like to thank the physics staff: Jane Carter, Nancy Chevry, Scott Bortolotto, and Sile Ni Scanlain. It is impossible to be able to thank Jane Carter in just a few words, but I just want to say that during all this lonely time far from my family that having her support helped me to feel safe. She is like a second mother to me. Thank you so much for helping me to become a stronger woman. I loved all my conversations with Nancy Chevry, she has the best laugh in the world and the most positive energy. I really appreciate her for cheering me up any time that we had a brief chat - these are very valuable for an international student. I am really grateful for Scott Bortolotto, he was always very supportive. Thank you for helping me to deliver my samples to their destinations safe and on time. Lastly, I would like to thank Sile Ni Scanlain for her caring attitude.

I was lucky to find several friends at Boston College. I would like to thank all

CHAPTER I

Introduction

Magnetic frustration can create exotic properties in quantum materials. This frustration is the product of magnetic competition between different interactions. A specific example of magnetic fluctuations in a quantum material is the quantum spin-liquid (QSL) phase, a state in which there is no ultimate resolution between the different interactions, even down to zero temperature. The QSL phase is one of the most sought-after quantum phases in condensed matter physics [1–5]. The presence of significant magnetic frustration leads to a large number of degenerate ground states which creates a long-range entanglement in the system. A highly degenerate ground state is the main criteria of a QSL phase and is one in which the spins are free to be oriented along many different directions at the same time, essentially forming in a coherent manner similar to a liquid [3–5]. The physics of the QSL phase has been heavily investigated in different classes of quantum materials due to their potential to host exotic excitations which can form the basis for topological quantum computation [6, 7].

The first studies to search for a QSL candidate started on a geometrically frustrated spin-1/2 system: a triangular lattice in the presence of AFM interactions. The original prediction for the ground-state of an AFM triangular model was based on the resonating valence-bond (RVB) states which refer to the super-

position of spin-singlet dimer configurations [8]. Although the ground state of the classical Heisenberg Hamiltonian for a triangular lattice is a 120° Néel state (with three sub-lattices); the combination of geometrical frustration and strong enough quantum fluctuations can lead to a breaking of the conventional classical ground state to form a QSL state [9, 10]. A few promising examples of QSL candidates with spin-1/2 configuration on a triangular lattice are κ-(BEDT-TTF)$_2$Cu$_2$(CN)$_3$, EtMe$_3$Sb[(Pd(dmit)$_2$)]$_2$, and NaYbO$_2$ [11–14].

The search for a QSL phase in geometrically frustrated systems was not limited only to triangular lattice structures. The so-called kagome lattice is another geometrically frustrated system that can potentially host a QSL phase. The ground state of the classical Heisenberg Hamiltonian for a kagome lattice is opposite to what is observed for a triangular lattice is highly degenerated. A spin-1/2 configuration AFM system on a kagome lattice is one of the potential candidates for a U(1) QSL state [5, 10, 15] and makes this lattice structure a strong candidate to search for a QSL phase. Some of the promising kagome and hyperkagome structure QSL candidates are ZnCu$_3$(OH)$_6$Cl$_6$ and Na$_4$Ir$_3$O$_8$ [16–19].

Investigations for a QSL phase in a geometrically frustrated system rely on a combination of quantum and geometric frustration to create a QSL state; however, designing a solvable Hamiltonian with a QSL ground state is a more powerful method to engineer QSL materials. Nearly two decades ago, Alexei Kitaev proposed a model for spin-1/2 particles with bond-directional Ising interactions on a two-dimensional honeycomb lattice which had the potential to host a QSL ground state [20]. The Kitaev model is especially appealing because the Hamiltonian for this model is exactly solvable, its ground-state hosts a QSL phase, and it can be engineered in real materials. This work initiated numerous investigations to design and synthesize materials that would physically realize the Kitaev Hamiltonian [20–22]. My Ph.D. research was mainly focused on studying the thermodynamic prop-
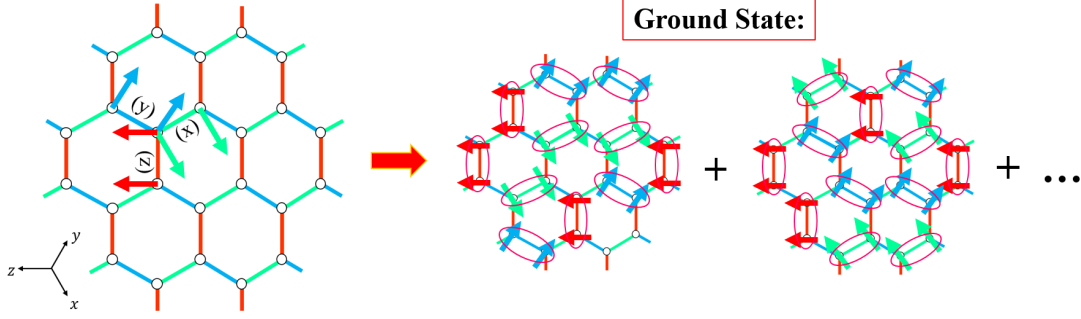
Figure 1.1: The Kitaev model on a honeycomb lattice. The spins are located on the vertices of each hexagon. This model is highly anisotropic and the bond-directional Ising interactions for NN interactions along the x, y, or z directions are presented in green, blue, and red, respectively. Superposition of different spin configurations (with two examples) for the ground-state are presented on the right.

erties of Kitaev materials and tuning the low-energy physics of the known Kitaev candidates towards QSL phase.

1.1 Kitaev Model

The Kitaev model is defined on a two-dimensional honeycomb lattice. The spin-1/2 particles are located on the vertices of each hexagon. Only the NN spin-spin interactions are considered in this model. These interactions are bond-dependent Ising interactions which means each spin can only be aligned with its NN along the x, y, or z directions, Fig. 1.1. These bond-directional interactions lead to a strong anisotropy which is the main ingredient for the frustration in this model. Different from what is discussed in the geometrically frustrated systems, the interactions here are ferromagnetic (FM)-type Ising interactions, rather than AFM-type Heisenberg interactions. The Hamiltonian for this model is:

$$H = \sum_{<i,j>} -K^x S_i^x S_j^x - K^y S_i^y S_j^y - K^z S_i^z S_j^z = \sum_{<i,j>} -K^\gamma S_i^\gamma S_j^\gamma \qquad (1.1)$$

where $< i,j >$ refers to all the possible NN spin-spin interactions and K^x, K^y, and K^z are the coupling constant coefficients [20, 23, 24]. Based on the Kitaev

Hamiltonian, spins can only be aligned with their NN 1/3 of the time (and add to the energy of the system) which leads to an infinite number of spin configurations that all can satisfy the Kitaev Hamiltonian for its ground-state energy in the thermodynamic limit, Fig. 1.1. The superposition of all these possible spin configurations generates a highly degenerate ground state for this model where the system can tunnel between any of these spin configurations and create a coherent liquid phase.

Each hexagon creates a plaquette or flux operator (W_P) which is defined by the product of six spin operators (Pauli matrices) for each bond on the hexagon. The W_P operators commute with the Hamiltonian which suggests they can have simultaneous eigenstates. However, if we have N number of spins in the honeycomb lattice, the Hilbert space dimension for the Kitaev Hamiltonian will be 2^N. Meanwhile, the number of W_P operators for the associated model is half of the degrees of freedom (N/2) and makes the Hilbert space dimension for the flux operators $2^{N/2}$. Thus, using the plaquette operators, one cannot completely solve the Kitaev Hamiltonian [5, 22].

The solution for the Kitaev Hamiltonian is instead obtained via fractionalization of the spin degree of freedom (S_i^γ) into four types of Majorana fermions: three localized and one itinerant ($\{b^x{}_i, b^y{}_i, b^z{}_i, c_i\}$) where $S_i^\gamma = \frac{i}{2} b_i^\gamma c_i$.

$$H = \frac{-1}{4} \sum_{<i,j>} K^\gamma b_i^\gamma b_j^\gamma c_i c_j \underset{u_{ij}=b_i^\gamma b_j^\gamma}{=} \frac{-1}{4} \sum_{<i,j>} K^\gamma u_{ij} c_i c_j \tag{1.2}$$

Here the Hamiltonian is presented in Majorana fermion form which contains two important parts: the flux (u_{ij}) and mater (c_i) parts. For the ground state, all the u_{ij} operators are equal and the system is in a flux-free state thus mater fermions (c_i) are free to move throughout the honeycomb lattice. One of the most interesting aspects of this theoretical model is when a small perturbation creates a protected

gap where the model can host anyonic excitations with non-abelian statistics [23, 24]. For a more detailed discussion of the Kitaev model the following references are suggested [20, 24–26].

1.2 Kitaev Materials

Engineering the Kitaev model in real quantum materials has become one of the greatest interests in condensed matter physics. Finding suitable candidates requires a clear understanding of the important features of the Kitaev model from an experimental point of view. The main features to implement in a Kitaev candidate are as follows: a honeycomb structure, a spin-1/2 configuration, and a high degree of anisotropy. Mott insulators in the presence of a strong repulsive Coulomb energy can be treated as spin-only systems which make them desirable candidates to search for Kitaev physics [21, 24, 27]. Mott insulators are a class of materials that, based on the conventional band theory of solids, are expected to behave like a metal, yet they show insulating behavior specifically in the low temperature regime. Among the Mott insulators, those comprised of transition metals with a partially filled d orbital are of the most interest as potential candidate materials to host Kitaev interactions.

The d orbitals have five degenerate energy levels. However, in an actual material the transition metal finds itself in a specific crystal field structure that has a specific geometry with lower symmetry than the spherical symmetry of the d orbitals. The electric field created by the crystal environment will thus partially lift the degeneracy of the d orbitals. This effect, known as crystal electric field (CEF) splitting or the Jahn-Teller effect, splits the five-fold degenerate d-orbitals into triply degenerate t_{2g} levels and doubly degenerate e_g levels. For $4d$ and $5d$ transition metals such as Ir, Os, Rh, and Ru where the effect of SOC is very strong (SOC $\propto Z^2$ where Z is atomic number), the degeneracy of the t_{2g} levels is further
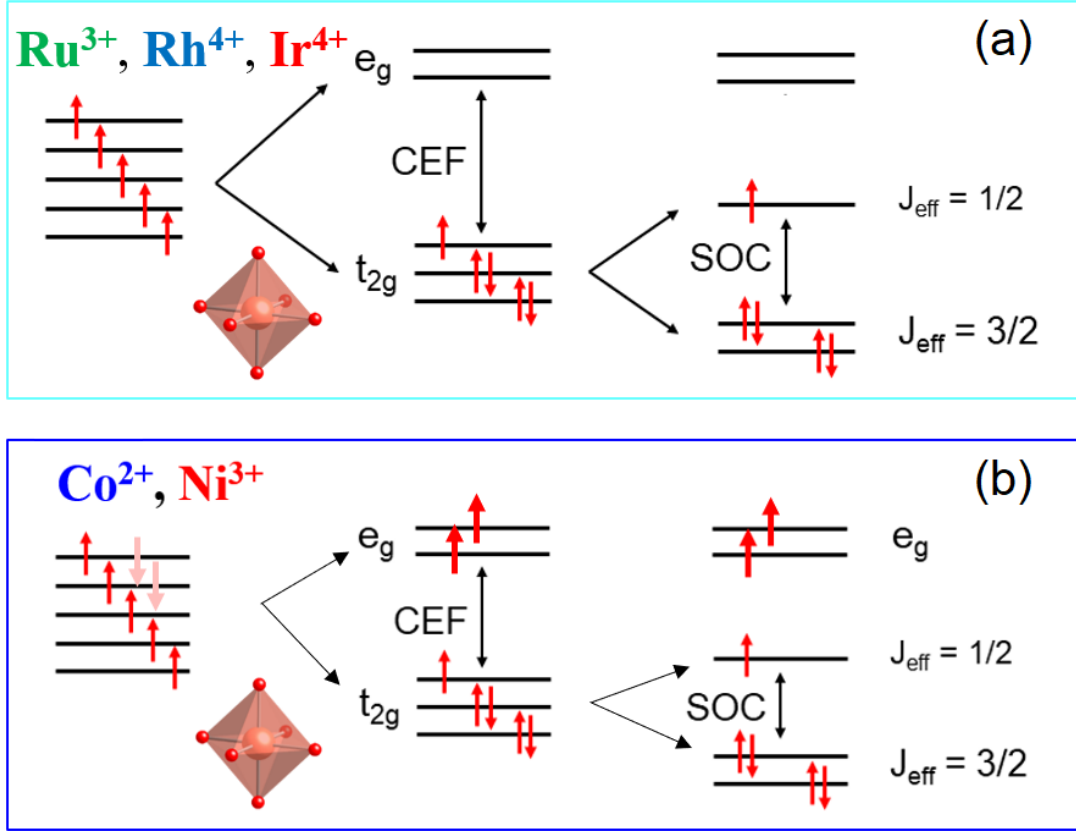
Figure 1.2: (a) Ir^{4+}, Rh^{4+}, and Ru^{3+} each has five electrons in the d orbital. The effect of crystal electric field (CEF) from the environment around these elements splits the five degenerate d levels into doubly degenerate e_g and triply degenerate t_{2g} levels. Finally, the effect of SOC lifts the degeneracy of the t_{2g} levels and splits it into $J_{\text{eff}} = \frac{1}{2}$ and $J_{\text{eff}} = \frac{3}{2}$ spin-orbital states. For the case of Ir^{4+}, Rh^{4+}, and Ru^{3+}, only one single electron remains in the $J_{\text{eff}} = \frac{1}{2}$ state and creates the spin-1/2 configuration required for the Kitaev model. (b) For the case of Co^{2+} and Ni^{3+}, the main differences are weaker CEF (more localized case) and SOC (smaller atomic number) effects and active electrons in the e_g levels. Weaker CEF and SOC effects bring the t_{2g} and e_g levels closer.

reduced and they are split into $J_{\text{eff}} = \frac{1}{2}$ and $J_{\text{eff}} = \frac{3}{2}$ spin-orbital states, Fig. 1.2(a). Specifically for Ir^{4+}, Rh^{4+}, and Ru^{3+}, which have only five electrons in their d orbitals, the combination of CEF and SOC leads to a single electron (or equivalent to that a single hole) in their $J_{\text{eff}} = \frac{1}{2}$ states, and its low energy physics can therefore be described by a spin-orbit Kramers doublet state [21]. Having a spin-1/2 system is one of the main criteria for the Kitaev model, which can be achieved via Ir^{4+}, Rh^{4+}, and Ru^{3+} transition metals in a Mott insulating compound [21, 23, 28, 29].

The presence of a strong SOC effect can fulfill two essential criteria for the Kitaev model: providing a pseudospin-1/2 ($J_{\text{eff}} = \frac{1}{2}$) spin-orbital state as discussed above, and the creation of anisotropy and bond-dependent interactions [23, 29]. Therefore, the $4d$ and $5d$ transition-metal honeycomb structures are better candidates for the QSL phase compared to the $3d$ transition-metals due to having a stronger SOC effect. The $3d$ transition-metals are lighter elements and they are more localized thus both CEF and SOC effects are weaker for this family. However, recent theoretical studies have suggested that the two criteria of anisotropic exchange interactions and a pseudospin-1/2 state can also be realized in $3d^7$ transition-metals such as Co^{2+} and Ni^{3+} ions. These ions possess a high-spin electron configuration ($t_{2g}^5 e_g^2$), S = 3/2 and L = 1, and octahedral CEF splitting that can also form a pseudospin-1/2 Kramers doublet state, Fig. 1.2(b). In this case, in addition to the single electron in the $J_{\text{eff}} = \frac{1}{2}$ states, the e_g levels are also not quenched. For the $3d$ transition-metals, the effect of CEF and SOC are weaker which leads to a proximity of the t_{2g} and e_g levels; therefore in addition to NN t_{2g} interactions, t_{2g}-e_g and e_g-e_g hopping interactions are also present. The Hund's coupling influences the interactions between the $J_{\text{eff}} = \frac{1}{2}$ and e_g electrons and forms ferromagnetic interactions which are in favor of Kitaev interactions [24]. Thus, the $3d^7$ Co^{2+}/Ni^{3+} honeycomb layered materials are equally as likely as $4d^5$

and $5d^5$ transition-metal honeycomb materials to host a QSL phase [30–32].

The transition metals in a honeycomb structure are located within an octahedral environment. The NN transition metals through the shared ligands can form a 90° bond (edge-shared octahedra) or 180° bond (corner-shared octahedra). For Kitaev physics, the edge-shared octaherda are more suitable. The hopping or charge transfer between two NN t_{2g} orbitals happens through shared ligands. For the edge-shared octahedra, the hopping interactions between d_{xz} and d_{yx} of adjacent transition metals is through p_z orbitals of the shared ligands. The only possible hopping paths are via the only two shared ligands between NN transition metals and for the ideal 90° connection between M-L-M (M and L are transition metal and ligand), the two paths cancel the Heisenberg interactions and the only remaining interactions are Kitaev terms [21, 24].

The above discussion is mainly for the ideal octahedral environment around the transition metals; however, it is not realistic to ignore the effect of local distortion in the octahedral environment of the transition metals. Any local distortion in the crystal field environment of a transition metal can heavily change the low energy physics of the system. The lattice distortion can reduce the degeneracy of the t_{2g} levels and change the spin-orbital state from the $J_{\text{eff}} = \frac{1}{2}$ or Kramers doublet state to a different state. A change in the spin-orbital state directly alters the nature of the magnetic interactions in the material. It is important to note that the energy scale of this so-called trigonal distortion should be large enough to compete with the SOC, otherwise its effect can be negligible. The trigonal distortion can manifest in the form of an elongation ($\Delta < 0$) or compression ($\Delta > 0$) of the ideal octahedron [24]. Trigonal elongation stretches the ideal octahedron along its polar ligands. This local distortion can lift the degeneracy of the t_{2g} levels and split them into a_{1g} (higher energy) and doubly degenerate e'_g (lower energy) levels. Then, the SOC effect completely removes the degeneracy of the doubly

8

degenerate e'_g levels. In the trigonal elongation case, the NN interactions from the pure Kitaev interaction limit change toward the Heisenberg interaction limit. Opposite to the elongation case, trigonal compression ($\Delta > 0$) splits the t_{2g} levels into a_{1g} (lower energy) and doubly degenerate e'_g (higher energy) levels. These local alterations change the NN interactions toward Heisenberg-Ising interactions [24]. For $5d$ transition metals such as Ir, the overwhelming effect of SOC retains the spin-orbital $J_{\text{eff}} = \frac{1}{2}$ state even in the presence of trigonal distortion; however, the trigonal distortion has more chance to compete with the SOC effect for the $4d$ and $3d$ transition metals [33].

1.3 Kitaev Candidates

The prime Kitaev candidates are α-Li$_2$IrO$_3$, Na$_2$IrO$_3$, Li$_2$RhO$_3$, and α-RuCl$_3$ [34–42]. In the case of oxides, the transition metal form an octahedral environment with O atoms. Then, these octahedrally coordinated transition metals form edge-shared connections with their adjacent transition metals and create honeycomb networks. At the center of each hexagon, an alkali atom (Li/Na) is located. Finally, these honeycomb structured layers are connected via octahedrally coordinated inter-layer alkali atoms. For α-RuCl$_3$, everything follows similarly with two main differences: first, there are no atoms at the center of the honeycomb networks of octahedrally coordinated Ru atoms and second, the connections between the layers are van der Waals (no inter-layer atoms). The oxidation state of all these magnetic elements in these honeycomb structured compounds are exactly what is required for creation of a spin-orbital Kramers doublet state. The edge-shared octaherally coordinated magnetic elements in α-Li$_2$IrO$_3$, Na$_2$IrO$_3$, Li$_2$RhO$_3$, and α-RuCl$_3$ make 93.66°, 99.2° ($\pm$ 0.2), 93.98°, and 92.59° bond angles, respectively [33, 43–48]. In all these compounds, the bond angle deviates from the ideal 90° bond condition which is required to retain only the Kitaev interactions. In addition to

bond angle deviation from the ideal 90°, the octahedral environment around the magnetic element undergoes a local distortion. The trigonal distortion strength in each compound can be estimated via bond-angle variance calculation (σ) [49]. The calculated σ for α-Li$_2$IrO$_3$, Na$_2$IrO$_3$, Li$_2$RhO$_3$, and α-RuCl$_3$ are 3.46°, 5.79°, 3.1°, and 2.16° , respectively [33, 43–48]. The combination of deviation of the bond angle connection from 90° and trigonal distortion suggests all these materials host other magnetic interactions in addition to the Kitaev interactions.

For an ideal Kitaev system, the candidate material is not expected to show any signs of long-range magnetic ordering down to zero temperature due to strong magnetic frustration in the system. However, when we study the magnetic properties of these prime Kitaev candidates all are magnetically ordered at low temperature. The long-range order for α-Li$_2$IrO$_3$ and Na$_2$IrO$_3$ sets in at 15 K, for Li$_2$RhO$_3$ it is $\sim$ 6 K, and α-RuCl$_3$ orders at 7 K [33, 36, 38, 40]. From the paramagnetic region of the magnetic susceptibility data, where the inverse of the magnetic susceptibility shows a linear behavior, the Curie-Weiss (CW) equation can be fitted to the data to extract important information such as the expected ordering temperature or the strength of interactions (Θ_{CW}) and effective moments (information about the spin-orbital state) in a material. Table 1.1 summarizes the effective moment (μ_{eff}), the CW temperature (Θ_{CW}), ordering temperature (T_c), and the type of magnetic order for these Kitaev candidates. By comparing the Θ_{CW} and T_c, we observe that a strong magnetic frustration is present in these compounds which suppresses the ordering temperature by an order of magnitude. However, this magnetic frustration is not strong enough to suppress the long-range order all the way to zero temperature. Different experimental work and theoretical calculations support the proximity of these prime Kitaev candidates to the Kitaev limit [23, 35, 36, 39, 42, 50–54]; therefore, developing new techniques for a structural modification of these materials and acquiring a deeper understanding

Table 1.1: The summary of the thermodynamic properties of the prime Kitaev candidates. The space group for all these compounds is $C2/m$.

Material	μ_{eff} (μ_B)	Θ_{CW} (K)	T_c (K)	Magnetic Type	Ref.
α-Li$_2$IrO$_3$	1.8	-105	$T_{\text{N}} = 15$	Incomm. Spiral	[34, 36]
Na$_2$IrO$_3$	1.9	-123	$T_{\text{N}} = 15$	Zig-zag	[35, 36, 55]
Li$_2$RuO$_3$	2.2	-44	$T_{\text{g}} = 6$	Spin-glass	[40, 41, 56, 57]
α-RuCl$_3$	2.0(ab)	$+68$(ab)	$T_{\text{N}} = 7$	Zig-zag	[48, 53, 58]
	2.3(c)	-145(c)			

about the relationship between the structural and magnetic properties of these compounds will help to explore the new physics related to the Kitaev materials as well as establish a clear method to design an ideal Kitaev candidate.

In chapter III, I explain how structural modification of the inter-layer chemistry of the parent compound α-Li$_2$IrO$_3$ changes the thermodynamic properties of the product compound Ag$_3$LiIr$_2$O$_6$. Using a topo-chemical synthesis method helps keep the honeycomb layers similar, while the inter-layer octahedral coordination in α-Li$_2$IrO$_3$ is replaced by a linear inter-layer coordination in Ag$_3$LiIr$_2$O$_6$. The replacement of inter-layer Li atoms with Ag atoms increases the SOC effect in the honeycomb layers and lowers the long-range ordering temperature in the exchange system and puts this honeycomb iridate compound closer to the Kitaev limit compared to its parent compound [44, 59–61].

The low energy physics of all prime Kitaev candidates is described by the $J_{\text{eff}} = \frac{1}{2}$ state that drives Kitaev interactions. Despite all the theoretical proposals for a diverse global phase diagram for the physics related to the Kitaev materials, the Kitaev candidates thus far are all in the $J_{\text{eff}} = \frac{1}{2}$ limit [21, 23, 62]. In chapter V, I explain how by only tuning the competition between the spin-orbit interaction and the trigonal crystal field splitting we restructure the spin-orbital wave function into a novel $\mu = \frac{1}{2}$ state that drives Ising interactions. This is done via a topo-chemical reaction that converts Li$_2$RhO$_3$ to Ag$_3$LiRh$_2$O$_6$, leading to an enhanced trigonal distortion and a diminished spin-orbit coupling in the latter compound.

The change of ground state is accompanied by a dramatic change of magnetism from a 6 K spin-glass in Li_2RhO_3 to a 94 K AFM in $Ag_3LiRh_2O_6$ which is one order of magnitude larger than all the studied Kitaev candidates. This experimental work is the first demonstration of tuning between the Kitaev and Ising limits in the same family of materials [33].

Although the topo-chemical synthesis method is a powerful technique to modify the low energy physics of Kitaev candidates, it can also increase the structural disorders such as stacking faults, in some cases unwanted rows of atoms, and change in the oxidation state of the magnetic elements in the honeycomb networks [55, 63]. In chapter IV, I present a comparative study of the magnetic susceptibility, heat capacity, and muon spin relaxation (μSR) between two different quality samples of $Ag_3LiIr_2O_6$, one high quality and one disordered. In the disordered sample, the absence of a peak in either susceptibility or heat capacity and the lack of zero field muon precession in the μSR signal gives the impression of proximity to a QSL state. However, in the clean sample, peaks are resolved in both susceptibility and heat capacity, and spontaneous oscillations appear in the μSR signal, confirming long-range antiferromagnetic order in the ground state. In this chapter I explain the importance of sample quality in the interpretation of experimental results for the physics related to Kitaev candidates [44, 64]. In chapter VII, I will provide an example of significant change in the oxidation state of magnetic elements in the honeycomb layers as a result of replacing intra-layer and inter-layer Li atoms in the parent compound, Li_2RhO_3 with the Cu atoms in product compound, Cu_2RhO_3.

As discussed above, recent theoretical studies on the $3d$ transition-metal honeycomb systems have suggested that the high-spin configuration $3d^7$ ions, when formed in a honeycomb structure, can potentially create Kitaev candidate materials in the limit of weak SOC [30–32]. One such material which has recently attracted a lot of attention as a Kitaev magnet is $Na_2Co_2TeO_6$. This honeycomb

compound crystallizes in space group $P6_322$ and shows three AFM ordering temperatures at 27, 15, and 7 K [65–69]. In chapter VI, I report our findings of a new polymorph of $Na_2Co_2TeO_6$ which is crystallized in the $C2/m$ structure more commonly found among the Kitaev materials. The change in crystal symmetry of the cobalt tellurate compound replaces the three transition temperatures of hexagonal $Na_2Co_2TeO_6$ by a single AFM transition at $T_N = 9.6$ K in the monoclinic polymorph.

CHAPTER II

Methodology

2.1 Material Synthesis

The first-generation of Kitaev spin-liquid candidates such as α-Li$_2$IrO$_3$, Na$_2$IrO$_3$, Li$_2$RhO$_3$, and α-RuCl$_3$ were synthesized under high-temperature conditions via a solid-state method [34, 36, 38, 57]. Unfortunately, all these layered materials are magnetically ordered and do not satisfy all the required criteria for an ideal candidate. Attempts to find a new Kitaev material beyond the first-generation candidates led to the introduction of a second generation of Kitaev materials. The magnetic properties of the first-generation Kitaev materials are tuned via a topo-chemical exchange reaction under mild conditions thus synthesizing the second-generation Kitaev compounds. In the topo-chemical exchange reaction, the inter-layer alkali metals (partial exchange reaction), and sometimes the intra-layer alkali metals (complete exchange reaction), are replaced by Cu, Ag, and H atoms. This synthesis method is performed under mild conditions to avoid any significant changes in the honeycomb structure of the parent compound and to try and keep the honeycomb networks as intact as possible. The quality of these layered honeycomb candidates directly affects the thermodynamic properties of the studied compounds; therefore, synthesizing high-quality samples is necessary for an investigation of these Kitaev candidate materials.

Honeycomb layered materials, α-Li$_2$IrO$_3$, Na$_2$IrO$_3$, and Li$_2$RhO$_3$ are three-dimensional layered systems where the honeycomb networks of Ir/Rh with an occupied center of alkali metals (Li/Na) are connected via octahedrally coordinated alkali metals (Li/Na). In the topo-chemical synthesis method, the octahedrally coordinated inter-layer atoms are replaced via linearly coordinated Cu, Ag, or H atoms. Both first- and second-generation Kitaev materials are layered; thus, they are prone to having more stacking fault disorder, which is the main reason why several steps of annealing are required in their preparation. A higher quality parent compound will help to increase the quality of the synthesized second-generation compound, reduce the amount of stacking fault disorder, prevent rows of unwanted atoms in the honeycomb layers, and reveal the thermodynamic properties of the studied systems more accurately.

During my Ph.D. research, I synthesized different first-generation Kitaev materials as precursors, such as polycrystalline and single crystal specimens of α-Li$_2$IrO$_3$, Na$_2$IrO$_3$, and Li$_2$RhO$_3$ in a simliar manner to the previous reports [35, 36, 52, 70]. I also was able to synthesize the second-generation Kitaev magnets such as polycrystalline samples of Ag$_3$LiIr$_2$O$_6$, Ag$_3$LiRh$_2$O$_6$, Cu$_2$RhO$_3$, and poly-crystalline and single crystal specimens of H$_3$LiIr$_2$O$_6$ [33, 44, 59, 64, 70–72]. In this chapter, I will explain the different steps required to synthesize these materials.

2.1.1 Solid-State Method

The first-generation Kitaev magnets are prepared via a conventional solid-state reaction at high temperatures (T $\geq$ 700 K) in air, under vacuum, or under the flow of O/Ar gas [34, 36, 57]. To improve the sample quality and remove stacking faults, it is necessary to perform successive stages of grinding and heating.

- **Polycrystalline sample of α-Li$_2$IrO$_3$:** A mixture of Li$_2$CO$_3$ and IrO$_2$ is well-ground and mixed together. The prepared mixture is pressed into a
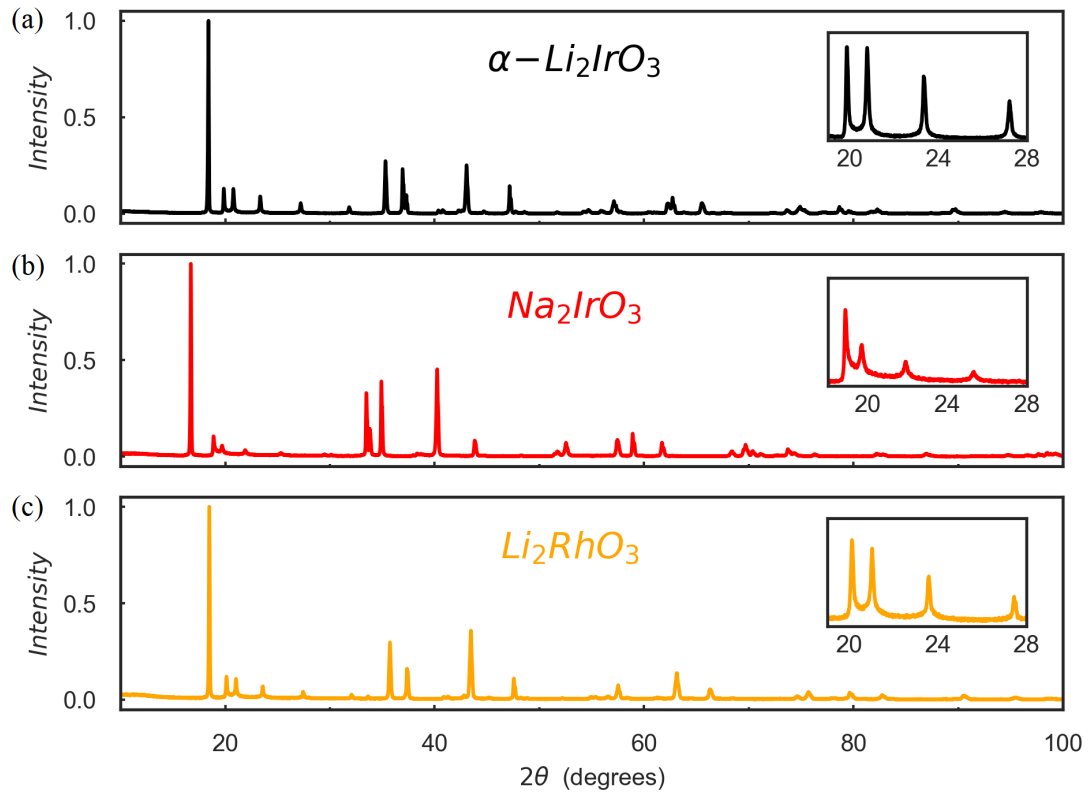
Figure 2.1: PXRD patterns of high-quality samples of α-Li$_2$IrO$_3$ (a), Na$_2$IrO$_3$ (b), and Li$_2$RhO$_3$ (c), respectively. The inset for each panel magnifies the honeycomb ordering peaks.

very loose pressed pellet. The synthesis for α-Li_2IrO_3 is done in air, but to avoid losing Li_2CO_3 (carbonates are very volatile) the furnace is set to start at 150 °C. The pressed pellet is placed in an alumina (Al_2O_3) crucible with a lid in a furnace. The sample is heated to 900 °C for 16 h and quenched at 600 °C to avoid unwanted phases. This procedure needs to be repeated several times and heated to 900 °C + x × 25 °C where x is the number of steps. In order to have a high-quality sample, I repeated the annealing steps until the x-ray pattern showed very sharp and well-separated peaks, especially the Bragg peaks in the range of 20° to 30°, which give information about the quality of the honeycomb structure in the compound, Fig. 2.1(a).

- **Polycrystalline sample of Na_2IrO_3:** The synthesis process for Na_2IrO_3 is done in air via a solid-state reaction. A mixture of Na_2CO_3 and IrO_2 is well-ground and mixed together. The loose powder is placed in an alumina crucible and placed into a furnace set to 150 °C to prevent evaporation of carbonate. The sample is heated to 850 °C for 48 hours, then quenched at 600 °C. The reheating process needs to be done at 900 °C for 24 hours as well. Based on the quality of the honeycomb peaks (peaks in the range of 20° to 28°), it can be decided whether to repeat the process again or not, Fig. 2.1(b). The annealing process for Na_2IrO_3 is shorter compared to α-Li_2IrO_3.

- **Polycrystalline sample of Li_2RhO_3:** The solid-state reaction for Li_2RhO_3 needs to be done under the flow of O gas to create the honeycomb phase. Without the flow of O, the product compound will be crystallized in the delafossite form. A mixture of Li_2CO_3 and Rh_2O_3 is well-mixed together and loose powder is placed in an alumina boat in a tube furnace (the boat is placed at the center of the tube furnace). The O gas should be run for
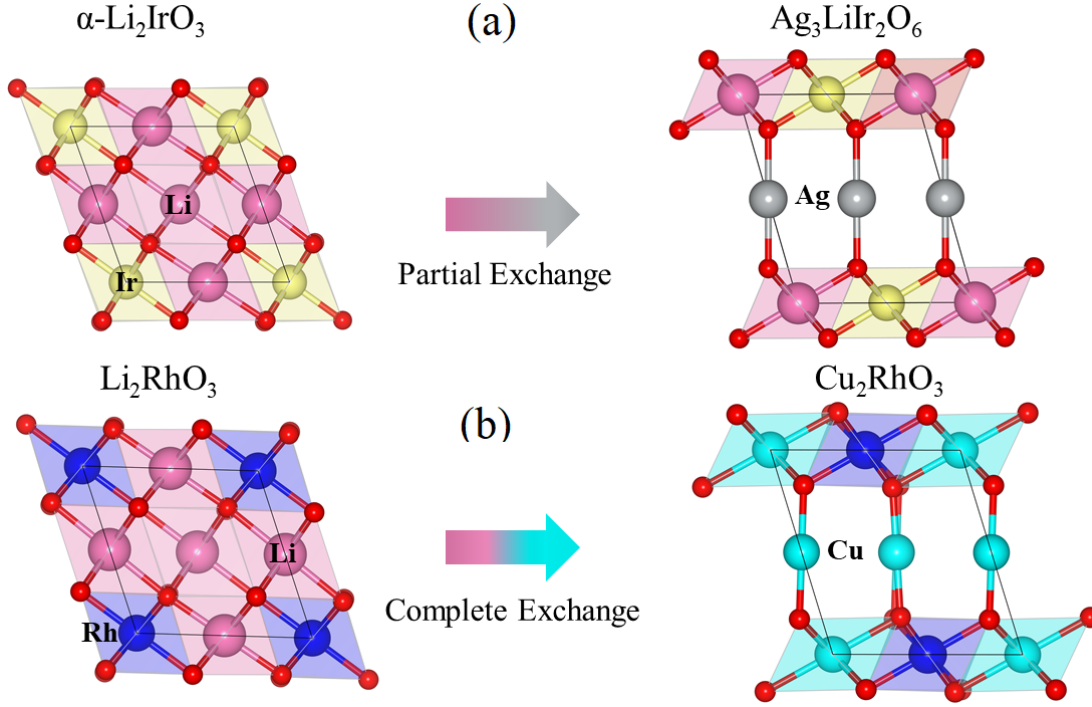
Figure 2.2: Synthesis of the second-generation Kitaev magnets from the first-generation materials through (a) partial and (b) complete exchange reactions. Both generations have honeycomb layers. The topo-chemical change of inter-layer coordination from octahedral to linear modifies the intra-layer M-O-M bond angles due to the change of oxygen positions.

a couple of minutes, then the sample is heated to 850 °C for 24 hours, and quenched at 600 °C. The flow of O gas will help synthesize a high-quality sample in only one round. An x-ray pattern of a high quality sample of Li_2RhO_3 is shown in Figure 2.1(c).

Note: all these honeycomb Kitaev materials are sensitive to humidity and performing any synthesis steps on a humid day causes impurities in the samples where the impurity phase is mostly the transition-metal oxide starting compound (IrO_2 or Rh_2O_3).

2.1.2 Topo-tactic Exchange Reaction

The second-generation Kitaev magnets are metastable compounds, i.e., they have a higher enthalpy of formation and a lower decomposition threshold compared to their stable counterparts [73]. Thus, it is impossible to synthesize them with conventional solid-state methods at high temperatures. Instead, they are stabilized through topo-chemical reactions from the first-generation compounds under mild conditions. As shown schematically in Figure 2.2 the global symmetries of the unit cell do not change during a topo-chemical reaction. The space group remains the same between parent compound and exchange material. However, local parameters such as bond lengths, bond angles, and inter-layer coordination, are modified efficiently. The inter-layer connections are mostly in an octahedral coordination in the parent compound (stronger connections), and are replaced by a linear or dumbbell coordination (weaker connections) in the exchange systems. The change in the inter-layer coordination modifies the O positions in the honeycomb layers and increases the trigonal distortion in the octahedral environment around the magnetic elements in the honeycomb networks. These structural changes are the bases to tune the magnetic properties of the first-generation Kitaev materials.

Topotactic exchange reactions can be either partial (Fig. 2.2(a)) or complete (Fig. 2.2(b)). The most general formulation of a partial exchange reaction is

$$2A_2MO_3 + 3BX \ \rightarrow \ B_3AM_2O_6 + 3AX \tag{2.1}$$
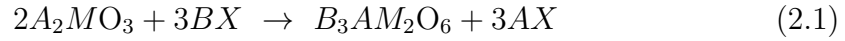
where the inter-layer A-atoms (typically Li or Na) in a stable honeycomb structure A_2MO_3 are exchanged with the B-atoms (typically Cu, Ag, and H) from a halide or nitrate salt BX.

In a complete topotactic exchange reaction, all A-atoms within and between the layers are replaced by the B-atoms.

$$A_2MO_3 + 2BX \rightarrow B_2MO_3 + 2AX \qquad (2.2)$$
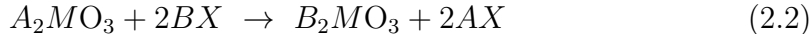
A complete exchange reaction is much less likely to happen.

During my Ph.D. research, I was able to successfully synthesize several second-generation Kitaev materials such as $Ag_3LiIr_2O_6$, $Ag_3LiSn_2O_6$, $Ag_3LiRh_2O_6$, $H_3LiIr_2O_6$ (polycrystalline and single crystal specimens), and a complete exchange system Cu_2RhO_3. Here is a general synthesis approach to synthesize these exchange materials.

- **Cu Exchange:** The Cu exchange reaction is the only reaction that creates a completely exchanged material from the first-generation compounds. CuCl and CuI are used as starting Cu^{1+} materials for the exchange reaction. CuCl works nicely for most of the Cu-exchange reactions, while in the case of $Cu_3NaSn_2O_6$, only CuI works [63]. For a Cu exchange reaction, a pressed pellet comprised of a mixture of the first-generation Kitaev magent and CuCl/CuI is sealed under vacuum in a quartz tube heated under mild conditions (T $\leq$ 350 °C). After the reaction, the product compound needs to be washed to remove any excess of the starting materials (CuCl or CuI) with ammonium hydroxide (NH_4OH, 28%). To remove any residual salt products (combination of Alkeli atoms and Cl/I atoms) after the reaction, the sample should be washed with deionized water. After washing the sample, it can be dried at room temperature under vacuum [55, 63].

- **Ag Exchange:** There is no example of complete exchange reactions for Ag-exchange materials. The starting material for the Ag-exchange reaction is $AgNO_3$. One of the main challenges for the Ag-exchange reaction is decomposition of $AgNO_3$ during the heating process. For the Ag-exchange reaction, a pressed pellet comprised of a mixture of the parent compound and $AgNO_3$ is sealed under a small amount of Ar pressure. After the re-
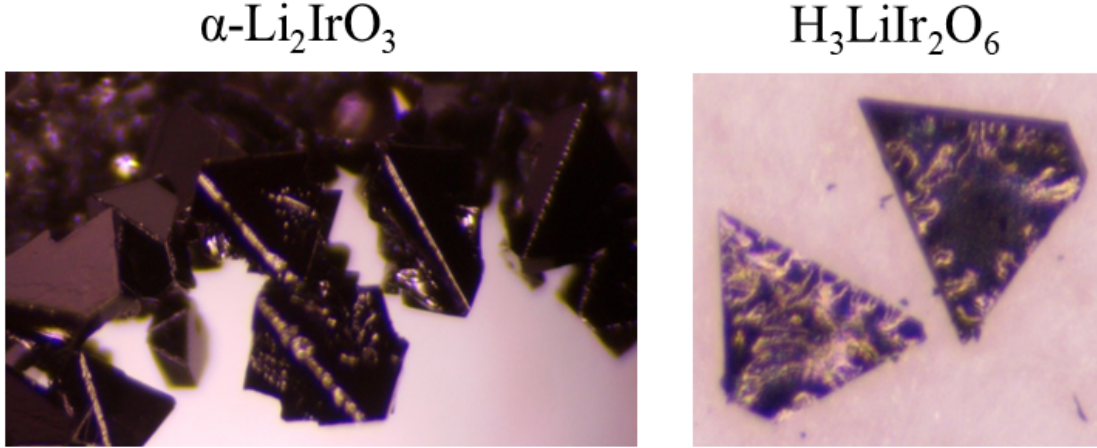
Figure 2.3: Single crystals of α-Li$_2$IrO$_3$ (left) and H$_3$LiIr$_2$O$_6$ (right).

action, the sample needs to be washed with deionized water to remove the residual nitrates. The Ag-exchange is prone to have Ag impurities after the reaction, that is why it is important to perform this synthesis under a mild condition (T $\leq$ 350 °C and slow rate). All the Ag-exchange materials are sensitive to any source of halides and they should be restored in an inert environment [44, 70].

- **H Exchange:** H$_3$LiIr$_2$O$_6$ is the only successful example of H-exchange reaction. The H-exchange reaction is done with a strong sulfuric acid under mild conditions (T $\leq$ 120 °C) [64, 72, 74]. One of the challenges for the H-exchange reaction is not having precise control over the number of H atoms between the layers, which can change the oxidation state of the magnetic element in the honeycomb layers to a non-magnetic version. H atoms are very light and mobile; therefore, the inter-layer connections between honeycomb layers are even weaker in these systems compared to the other second-generation compounds [64], leading to several stacking disorders [72]. Figure 2.3 shows single crystals of α-Li$_2$IrO$_3$ (left) and single crystals of H$_3$LiIr$_2$O$_6$ (right). H$_3$LiIr$_2$O$_6$ displays a purple color.

21

2.2 X-Ray Diffraction

One of the most essential techniques for material characterization is x-ray diffraction. X-ray diffraction scans provide several important pieces of information such as the quality of the sample, different phase impurities, and, most importantly, experimental data required for crystallographic analysis. During my Ph.D., I worked primarily with a powder x-ray diffraction (PXRD) instrument, the Bruker D8 ECO instrument equipped with a copper x-ray source (Cu K_α), a nickel filter to absorb the K_β radiation, and two 2.5° Soller slits after the source and before the LYNXEYE XE 1D energy-dispersive detector.

The x-ray wavelengths for material characterization purposes are between 0.5 to 2.5 $\mathring{A}$, the same order of magnitude as the inter-atomic distances in materials. There are two common x-ray sources for which the conventional sources used in laboratories are x-ray tubes. The x-ray tubes consist of an anode coupled with a cathode sealed inside a metal/ceramic container under high vacuum [75]. The input power of our x-ray tube is 1000 W (40 KV and 25 mA) to electronically heat the cathode filament (typically tungsten) and emit high energy electrons towards the anode. The anode material for our x-ray tube is Cu metal, which is hit by the high-energy electrons and creates x-rays. The heat produced during this process cannot be dissipated by the x-ray tube; thus, chiller water is required to constantly cool down the anode material. During the x-ray creation, some of the high-energy electrons unexpectedly decelerate and produce a continuous background called the white line. Each x-ray spectrum has three characteristic wavelengths: K_{α_1}, K_{α_2}, and K_β, which for a Cu source are 1.54059, 1.54441, and 1.39225 $\mathring{A}$, respectively. The transitions from the L to the K shell create the K_α wavelengths, and the transition from the M to the K shell produces the K_β wavelength. More specifically for the K_α wavelengths, transitions from $2p_{1/2}$ to $1s_{1/2}$ and $2p_{3/2}$ to $1s_{1/2}$ correspond to K_{α_1} and K_{α_2}, respectively. The intensity of
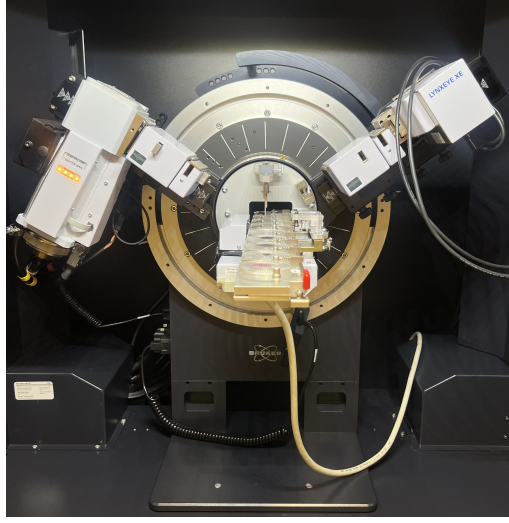
Figure 2.4: Powder x-ray diffraction (PXRD) instrument with Bragg-Brentano geometry.

K_{α_1} is twice larger than that of K_{α_2} and the intensity of the K_α wavelengths are five times larger than K_β [75]. The K_β wavelength can be filtered out, and for a Cu source x-ray tube a Ni filter is used to completely absorb the K_β line [75].

To perform a x-ray diffraction measurement on a synthesized material, the polycrystalline or single crystal specimen needs to be well-ground and prepared in a very fine powder form. The next step is to prepare a very homogeneous layer of material on a standard puck to reduce the background produced during the x-ray measurement. The PXRD instruments for powder diffraction mostly have the Bragg-Brentano geometry where the x-ray tube and detector move in a circular path with a fixed sample position. To obtain the information from different orientations in the sample, the puck can be rotated at its fixed position.

The measured x-ray patterns can be explained by Bragg's law:

$$2d_{hkl}\sin(\theta_{hkl}) = n\lambda \tag{2.3}$$

where d is the inter-planar distance, hkl are the Miller indices, θ_{hkl} is the Bragg angle or diffraction angle, λ is the wavelength of the x-ray source (anode material),

$2d_{hkl} \sin(\theta_{hkl})$ is the path difference between the incident and reflected wavefront, n is the order of reflection which is equal to 1 in calculations, and $n\lambda$ is the condition for constructive interference. Bragg's law makes a clear connection between the Bragg angles, the wavelength of the x-ray source, and the inter-layer spacing [75]. A measured x-ray pattern is unique for each compound and the Bragg peaks have unique relative positions and intensities based on the crystallographic structure, chemical composition, and atomic positions of the measured material. To identify the crystal symmetry (space group), atomic positions and coordination, and the lattice parameters in a newly synthesized compound, a careful crystallographic analysis is required for which Rietveld refinement is a common method used for the structural analysis.

2.2.1 Rietveld Refinement

Rietveld refinement is a method to identify the structural properties of materials. This method can be used for both x-ray diffraction and neutron diffraction data and extracts important features such as space group or crystallographic symmetries, lattice parameters, atomic positions and their coordination. The x-ray or neutron diffraction data consist of a series of reflection peaks with specific relative intensities, peak shapes, and certain peak positions. Through the reflection peak positions, the lattice parameters can be determined. Each reflection peak belongs to one or more Miller indices (hkl) which are used to determine the lattice parameters (a, b, c, α, β, and γ). For instance, the first reflection peak in a x-ray diffraction pattern provides information about the c axis in the unit cell because the Miller indices for this peak only have a non-zero value for l ($00l$). The relative intensities of the reflection peaks provide information about the atomic positions and their coordination. Determination of the correct space group or crystallographic symmetries in a material is the key factor to identify the correct atomic
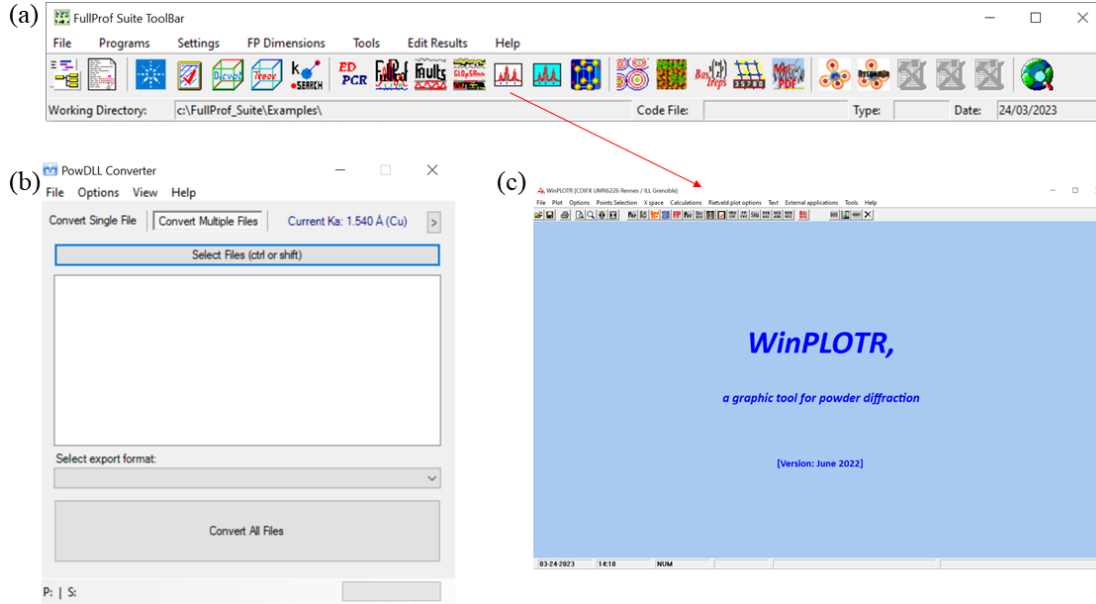
Figure 2.5: (a) FullProf Suit. (b) PowDLL converter. (c) WinPLOTR

positions and coordination. In each space group, there are a set of Wyckoff positions which are described by their multiplicity (the number of points belonging to one of its orbits within a unit cell), and a Wyckoff letter (refers to a specific orbit in a unit cell) written next to the multiplicity number. The Wyckoff letters are labelled by a, b, c, etc. beginning from the position having the highest site symmetry. For example, in space group $C2/m$, 2a, 2b, 2c, 2d are written in order of the highest site symmetry. The shape of the reflection peaks provide information about the crystallinity of the sample. Sharp and well-separated Bragg peaks are a signature for a well-defined crystal structure in a material.

Figure 2.5 shows the required software tools for a Rietveld refinement with FullProf software [76]. A FullProf Suite ToolBar (GUI shown in Fig. 2.5(a)) is required to prepare the essential files, such as the PCR file, to perform a Rietveld refinement. A collected x-ray diffraction pattern needs to be converted to a .xy format for analysis via PowDLL Converter, Fig. 2.5(b). After converting the x-ray file to a .xy format file, then the .xy file is viewed in the FullProf Suite ToolBar: choose the Run WinPlotr option (Fig. 2.5(c)), File → open pattern

file → Points selection → select background points → save background points and create a background point file for Rietveld refinement. To select background points correctly, it is important to keep the number of selected points somewhere close to 20 points, the position of the selected points should not be very close to the Bragg peaks or their shoulders to prevent this from affecting their shape, and avoid selecting points very close to one another. After preparing the x-ray file and the background points, the last piece for Rietveld refinement via FullProf is to prepare the PCR file. There are two approaches for creating the PCR file: modifying a PCR file or converting a cif to a PCR file.

- Method 1: FullProf Suite ToolBar → ED PCR, which opens a new window titled Editor of PCR file. From here, select File → open data file, and select a PCR file from before and edit it according to the new conditions for the synthesized material.

- Method 2: FullProf Suite ToolBar → ED PCR, to open the Editor of PCF file window. Select cif to PCR (type (x-ray), IRF file (the instrumental information), space group, lattice parameters, and the atomic coordination.)

The Editor of PCR file window has different options to include all the important crystallographic features of a studied material, so it is important that every option is modified accordingly, Fig. 2.6. First is the General window where we can select the type of calculation. For example, calculations for an obtained powder x-ray diffraction data are Refinement/calculations of a Powder Diffraction Profile. Patterns option includes Data file/Peak Shape, Background Type, Excluded Regions, and Geometry/IRF, Fig. 2.6.

- Data file/Peak Shape: upload the data file with correct file format (xy file format for x-ray patterns), then the source of the measurement with correct wavelength (for the x-ray data used in this thesis, the x-ray tube is a Cu-

26
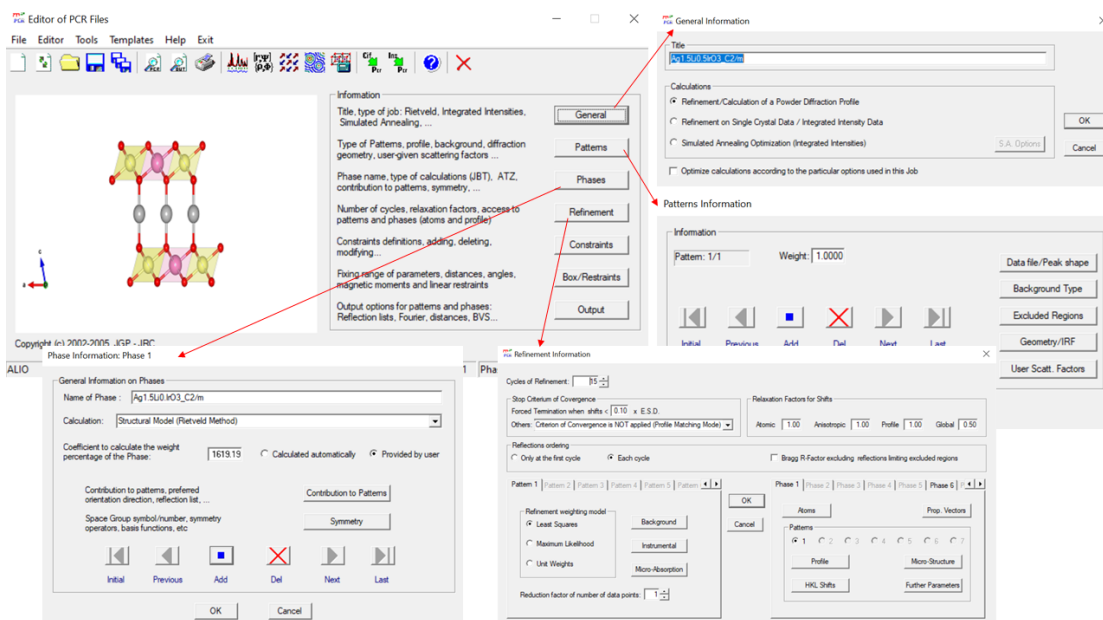
Figure 2.6: The Editor of PCR file has different options to include all the required crystallographic information about the studied material.

K_α source). The peak shape is Thompson-Cox-Hastings pseudo-Voigt $*$ Axial divergence asymmetry which is a correction for powder diffraction peak shapes [77].

- Background Type: It is better to select the background points through the obtained x-ray data. In this case, the correct option is Linear interpolation between a set background points with refinable heights (the height of these background points will refine once the refinement is very close to the correct solution to adjust the y values).

- Excluded Regions: Sometimes to help the refinement correctly identify the unit cell parameters, it is helpful to remove impurity peak regions. However, the excluded regions need to be added to the refinement once the unit cell parameters are determined. It is possible to perform two phases of refinement; thus, if the phase of the impurity peaks are defined the second phase can be added to the refinement.

- Geometry/IRF: This part includes the instrumental parameters for the x-ray diffraction instrument. The x-ray diffraction instrument used for all the studied materials in this thesis has a Bragg-Brentano Geometry and a IRF file (instrumental parameters) is required to be uploaded to create a correct PCR file. In the correction section, the modified March's Functions is required for the powder diffraction analysis. The modified March's Function is a correction function for including the preferred orientation in a material. The equation for this function is

$$P_h = G_2 + (1 - G_2)((G_1 cos\alpha_h)^2 + \frac{sin^2\alpha_h}{G_1})^{-3/2} \tag{2.4}$$

where G_1 and G_2 are refinable parameters for preferred orientation coefficients. In the modified March's function, G_2 sets to 0 and only G_1 is refinable. For the Bragg-Brentano geometry, the G_1 can be in different range values:

- $G_1 < 1$: platy or flat shape, α is the acute angle between the scattering vector and the normal to the crystallites

- $G_1 = 1$: no preferred orientation

- $G_1 > 1$: needle or sharp shape, α is the acute angle between the scattering vector and the fibber axis direction

For neutron powder diffraction instruments which have the Debye-Scherrer geometry, the condition is the opposite. For more details read the FullProf Manual [78].

The Phase option contains calculation method information (structural model (Rietveld method) or magnetic phase (Rietveld method)), different patterns, contribution to patterns (weight), and symmetry (space group) information.

- Contribution to patterns: The refinement on the same data file can be done

for different phases. This is very useful if the x-ray pattern of a material contains the impurity phases. Each phase can have different weights and the correction for peak shape for each phase should be selected based on the measurement conditions. For example, for powder x-ray diffraction data, the correction for peak shape is Thompson-Cox-Hastings pseudo-Voigt * Axial divergence asymmetry. The next point is related to the relative intensities of Bragg peaks. To model the Bragg peaks with correct intensities, the space group and Wyckoff positions need to be selected correctly as we know the relative intensity of the peaks is affected by the atomic positions and coordination in a material. The reflection list is created by Automatically generated from the Space Group symbol.

- Symmetry: The symmetry operators are generated automatically from the space group symbol. The space group name can be written in both number or symbol form; for example, space group 12 or C 1 $2/m$ 1 (in the symbol format the spaces are necessary). After selecting the correct space group, the related information such as Laue class needs to be checked.

The Refinement option contains important information about the refinable parameters. The Rietveld refinement is based on the least squares method to model the obtained experimental data. When we run the refinement, the number of cycles will help the program to converge; therefore, the number of cycles should be large enough to give the program enough time (N = 15). The relaxation factors for atomic, anisotropic, and profile shifts are all 1; however, the global shift is 0.5.

- Background: The selected background points can manually import and a linear interpolation method should be selected similar as in the Pattern option.

- Instrumental: The only correction that we need for 2θ data is the displace-

ment correction on the peak positions which can be due to the change in the depth of the standard puck or the mounting position inside the instrument. This parameter should be smaller than 1.

- Atoms: The information about all the atoms in an unit cell such as atom type, Wyckoff positions (x, y, z), isothermal factors (displacement for each atom), and occupation number is provided here. The thermal factor for similar elements should be the same, the lighter elements have larger values compared to heavier elements. The occupancies for each atom are calculated based on the ratio of the site multiplicity (m) and general multiplicity (M) in a space group.

- Profile: There is a separate Profile option for each phase and pattern. This part contains important refinable parameters such as Scale factor, overall B-factor, lattice parameters, Gaussian and Lorentzian coefficients for the peak shape correction function, and the instrumental parameters. The scale factor affects the relative intensities of Bragg peaks which can be different due to the amount of material used in the x-ray scan. The overall B-factor corrects the underestimation/overestimation in the isothermal factors for each atom in an unit cell. The overall B-factor mostly affects the high-angle 2θ peaks and it is important to be corrected after correcting the y values for background points. The lattice parameters are listed in this part and if the option of cif to PCR for creation Editor of PCR is used the values are already imported, otherwise they need to be manually added. The U, V, and W are the instrumental parameters which are obtained through the refinement of the x-ray diffraction pattern of standard corundum while all the other parameters are fixed. The instrumental parameters are not refinable and are imported through the IRF file in Pattern option. U and W are
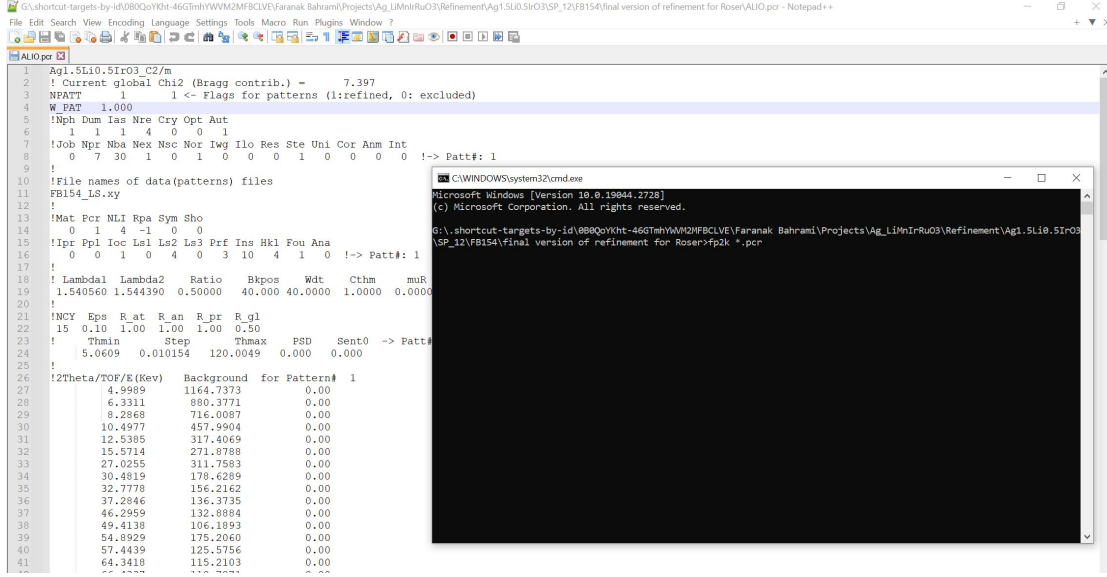
Figure 2.7: Visualization of the Editor of PCR file via Notepad++. The terminal to run the refinement is shown as an inset with the command of fp2k *.pcr.

positive while V is negative. The peak shape correction is a pseudo-Voigt function which is the convolution of Gaussian and Lorentzian functions. X is the coefficient of the Gaussian function and Y is the coefficient of the Lorentzian function. Both X and Y are refinable; however, instead of the Y value, Anisotropic Lorentzian size broadening (Spherical Harmonic) can be refined. The last part is the coefficients for preferred orientation function, the modified March's function, are given here.

- Micro-structure: According to the selected space group, the correct size-model should be chosen. According to the Laue class, there are some conditions on the refinement option of the spherical harmonic coefficients. The spherical harmonic coefficients can be a better option to consider the Lorentzian part in the peak shape correction function compared to Y for honeycomb layered materials.

After modifying the PCR file through the GUI, it is easier to run the refinement via the Notepad++ software, Fig. 2.7. Here, I will summarize the order of the steps

```
81    C 1 2/m 1                    <--Space group symbol
82    !Atom    Typ       X          Y         Z        Biso        Occ       In Fin N_t Spc /Codes
83    O1        O      0.38800   0.33140   0.83240   0.40000    1.00000     0    0    0     0
84        |        |        0.00      0.00      0.00      0.00       0.00
85    O2        O      0.10900   0.50000   0.16700   0.40000    0.50000     0    0    0     0
86        |        |        0.00      0.00      0.00      0.00       0.00
87    Ir1      Ir      0.00000   0.66914   0.00000   0.25000    0.40133     0    0    0     0
88        |        |        0.00    201.00      0.00      0.00      11.00
89    Li1      Li      0.00000   0.66914   0.00000   0.25000    0.09805     0    0    0     0
90        |        |        0.00    201.00      0.00      0.00      21.00
91    Ir2      Ir      0.00000   0.00000   0.00000   0.27000    0.09684     0    0    0     0
92        |        |        0.00      0.00      0.00      0.00      31.00
93    Li2      Li      0.00000   0.00000   0.00000   0.27000    0.15252     0    0    0     0
94        |        |        0.00      0.00      0.00      0.00      41.00
95    Ag1      Ag      0.50000   0.31732   0.50000   0.35000    0.50000     0    0    0     0
96        |        |        0.00    211.00      0.00      0.00       0.00
97    Ag2      Ag      0.00000   0.50000   0.50000   0.35000    0.25000     0    0    0     0
98        |        |        0.00      0.00      0.00      0.00       0.00
99    !-------> Profile Parameters for Pattern #  1
100   !  Scale        Shape1       Bov       Str1       Str2       Str3    Strain-Model
101    0.23194E-03   0.00000  -0.00045   0.00000    0.00000    0.00000       0
102       51.00000      0.000    241.000     0.000      0.000      0.000
103   !     U           V          W          X          Y        GauSiz   LorSiz Size-Model
104      0.003670  -0.003390   0.001370   0.241603   0.000000   0.000000   0.000000   15
105        0.000       0.000      0.000    231.000      0.000      0.000      0.000
106   !     a           b          c        alpha       beta      gamma     #Cell Info
107      5.283172    9.135516   6.485942  90.000000  74.289703  90.000000
108      61.00000    71.00000   81.00000   0.00000   91.00000    0.00000
109   ! Pref1     Pref2      Asy1      Asy2      Asy3      Asy4      S_L       D_L
110    1.02833   0.00000   0.00000   0.00000   0.00000   0.00000   0.00000   0.00000
111     191.00      0.00      0.00      0.00      0.00      0.00      0.00      0.00
112   !   Y00        Y20       Y22+      Y22-       Y40       Y42+
113     2.317514   0.909517  1.137735  -0.408122  -2.561216   1.162674
114      101.00     111.00     121.00     131.00     141.00     151.00
115   !   Y42-       Y44+       Y44-
116    -1.111294  -1.146094   0.994637
117      161.00     171.00     181.00
118   ! Limits for selected parameters :
119      1        0.0000       0.5000      0.0000   0  Occ_Ir1_ph1
120      2        0.0000       0.2500      0.0000   0  Occ_Li1_ph1
121      3        0.0000       0.2500      0.0000   0  Occ_Ir2_ph1
122      4        0.0000       0.2500      0.0000   0  Occ_Li2_ph1
123   !  Set of  4 linear restraints:
124   !  Identifier, number of coeff., value, sigma / List of coeff & Parameters
125   Site1     2        0.500000          0.000500          -> Current calculated value:        0.499386
126     1.0000  1    1.0000  2
127   Site2     2        0.250000          0.000500          -> Current calculated value:        0.249365
128     1.0000  3    1.0000  4
129   Ir        2        0.500000          0.000500          -> Current calculated value:        0.498184
130     1.0000  1    1.0000  3
131   Li        2        0.250000          0.000500          -> Current calculated value:        0.250567
132     1.0000  2    1.0000  4
133   !  2Th1/TOF1    2Th2/TOF2   Pattern to plot
134       10.000       119.969        1
135
```

Figure 2.8: An example of refined parameters in a PCR file viewed in Notepad++.

for a successful structural refinement via Rietveld method for a new compound.

- The first parameters to refine are the lattice parameters, line 106 in Fig. 2.8. The first peak position can be directly controlled by modifying c, and the next couple of peaks (specifically in honeycomb-layered structure) are controlled by a and b. In this step, it is better to change the values for the lattice parameters manually and then, once the peak positions and the model are in good agreement, then refine the lattice parameters one by one (code is in the line 108).

32

- The next two parameters to refine are the scale factor (line 100) and X (line 103) to modify the relative intensities and the peak shape in the model. The combination of refinement of these two parameters would significantly improve the peak shape and intensities.

- To include the Lorentzian function in the peak shape correction, it is better to refine spherical harmonic parameters (line 112 and 117) instead of Y (line 103). To have the correct spherical harmonic parameters, the number for Size Model (line 103) needs to be selected correctly (FullProf Manual page 117 [78]). It is important to carefully check the condition for the specific Laue class for the selected Size Model. For some Laue classes, some of the spherical harmonic coefficients are not refinable. You can find examples for Size Model 17, 19, 21 in the FullProf Manual [78].

- After spherical harmonic coefficients, the preferred orientation coefficient (line 109) can be refined. This coefficient is either slightly larger or smaller than 1 depending on the preferred orientation of the sample.

- The next parameters to refine are the refinable Wyckoff positions for the atoms in the unit cell (line 82 to 98). Sometimes, a small change in the atomic positions can have a huge impact on the results of the refinement. However, it is important to mention that x-ray diffraction is not sensitive to light elements like oxygen and to obtain accurate information about their atomic positions, neutron diffraction experiments are required. Otherwise, for oxygen positions other materials with similar structures can be used as a reference.

- At this step, the refinement is in a very good shape and refining the background points can be very helpful. To refine the height intensities of background points it is better to divide them into two parts and refine them

separately. The background point refinement affects the isothermal factor values significantly; therefore, the refinement of overall B-factor should be the last item.

- At this step, if there is a possibility of refining the occupation number for atoms in the unit cell all the refined parameters should be off. It is easier if this step is done via the GUI. Then turn on the occupanies for refinable atoms and put constraints on the occupation number and fix the range of the parameter. In the Editor for PCR, Box/Restraints option put a fixed range of values for each occupation number (line 118 to 135). Then repeat all the steps in the same order again.

- After Refining background points for the second round, the next parameter is to include the changes due to displacement in the x-ray pattern. This parameter is SyCos and it should be less than 1, the smaller the better.

- The final parameter to refine is the overall B-factor. The positive value of the overall B-factor means the isothermal factors for the atoms are smaller than what they should be and a negative value means the isothermal factor values are overestimated.

After completing all the steps for refining the x-ray diffraction data of your sample, in addition to checking the overall agreement between the collected data and the calculated model (residual plot), the R-factors, χ^2, and goodness of the fit need to be checked as well. The R-factors in the Rietveld refinement are R_{wp} (weighted profile R-factor), R_{exp} (the best value that can be obtained for R_{wp} from analysis, expected R-factor), R_P (profile factor), R_B (Bragg factor), and R_F (crystallographic R-factor). From R_{wp} and R_{exp}, the goodness of fit and χ^2 can be calculated ($\frac{R_{wp}}{R_{exp}}$) and ($\frac{R_{wp}}{R_{exp}}$)^2, respectively [76, 79]. As mentioned before, the R_{exp} is the best value that R_{wp} can get; thus the χ^2 cannot be less than one [79]. There
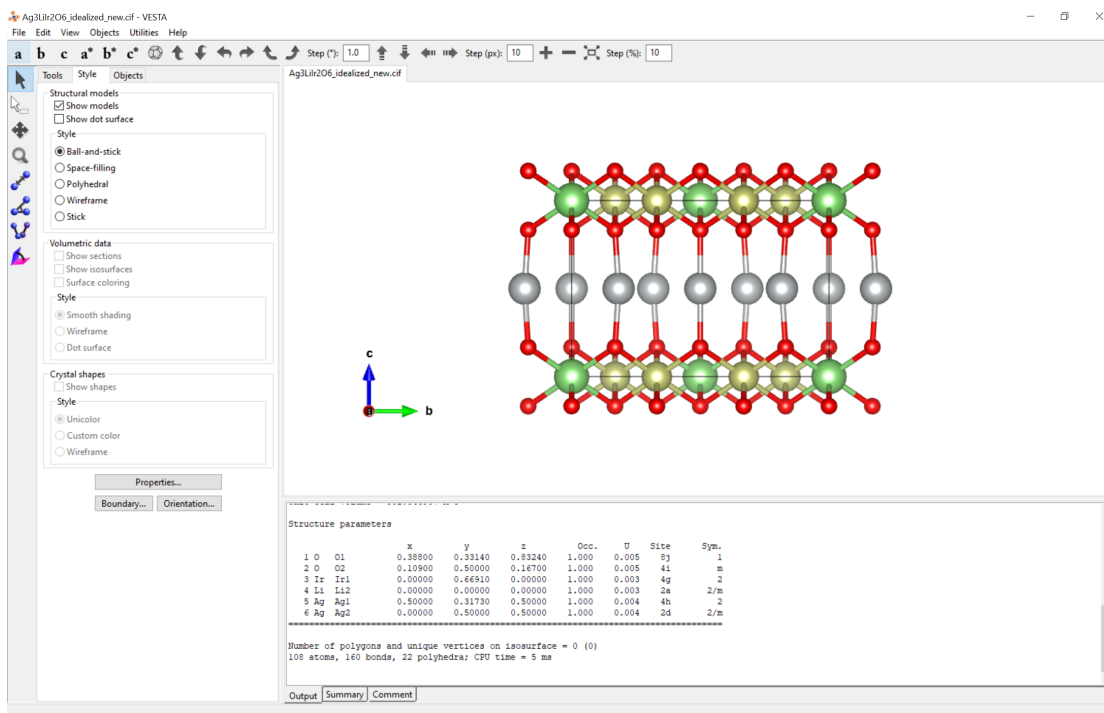
Figure 2.9: A visualized crystallographic information file (CIF) in vesta.

is no clear upper limits for these R factors because they are influenced by several factors such as having a well-defined structural model, correction of background in the diffraction data, and the peak shapes and positions [79]. However, it is important to keep track of them and also the values for them should not be very large. There are also other parameters that can help to check the quality of the Rietveld refinement such as Durbin-Watson statistic parameters (see FullProf Manual) [76, 78, 80]. These statistics are based on the correlation between the peaks in the residual plot and provide information about the signs of the successive peaks in the residual plot.

2.2.2 Crystallographic Information File

One of the most practical products of the Rietveld refinement is the crystallographic information file (CIF). This file can be used to visualize the crystal structure of the studied material, the main experimental piece of information

35

for theoretical calculations, and provides helpful structural details such as bond lengths and bond angles. The VESTA software is used to create a graphical presentation of a CIF in Fig. 2.9 [81]. There are several options in VESTA that help modify the presentation of the CIF.

- Edit → Edit Data: this option provides the possibility of correction/modification of unit cell parameters and structural parameters.

- Edit → Bonds: this option helps to define new bonds or remove some of the unwanted ones.

- Objects → Properties or Boundary: it can help to change the details in the presentation of crystal structure such as the number of layers, color of atoms, etc.

- From Utilities, it is possible to reproduce the powder diffraction pattern from the calculated model. This option can be helpful if the x-ray diffraction data of synthesized material does not exist in the database.

2.3   Magnetization

Studying the magnetic properties of new materials is one of the essential steps in their characterization. The magnetic response of a material can be studied as a function of temperature under different applied magnetic fields (M vs. T) or as a function of magnetic field at different temperatures (M vs. H). Each of these measurements provides important details about the general magnetic properties of studied material. A Quantum Design Magnetic Property Measurement System (MPMS3) is used for all magnetization measurements presented in this thesis. Based on the form of the sample, a proper sample holder is chosen for the measurement. For powder specimens, the sample can be packed into a plastic

capsule, mounted on a brass holder, or placed into a straw. For single crystal samples, the sample can be mounted on a quartz holder and fixed with varnish or with sapphire in a straw. Once the sample is in a proper holder, you place the sample holder inside the MPMS3 chamber. After centering, the sample is located at the center of superconducting pickup coils. Then the sample moves inside the coils in the presence of an applied magnetic field. The samples' movement creates current based on Faraday's law and through a superconducting quantum interference device (SQUID) is converted into a voltage. The obtained voltage as a function of sample position is fitted to an expected response function and provides us with the magnetization of the measured sample [82].

Magnetization as a function of temperature- From magnetization measurements under small applied fields, the magnetic susceptibility is calculated (the value for the applied field should be in a range where the magnetization has a linear behavior as a function of field). Magnetic susceptibility is $\chi = M/H$, where M is magnetization and H is a very small applied magnetic field (this relationship is not correct for large applied field). Magnetization can be measured from 1.8 K to 400 K via the MPMS3 instrument. For very high or low temperature ranges, the oven option or ^{3}He option can be used, respectively. Observation of any anomalies such as a peak, a sharp or broad downturn, or any saturation refers to a specific type of magnetic ordering in a material. The magnetic susceptibility can also display evidence of structural disorder; a very large upturn tail in a layered material can be a sign of stacking fault disorder. Different types of magnetic ordering are presented with different critical temperature symbols, AFM order (T_N), FM order (T_C), and spin-glass (T_g).

From the high-temperature data, important parameters such as effective magnetic moment (μ_{eff}) and CW temperature can be obtained. The paramagnetic region (temperatures very higher than ordering temperature) is fit to the CW

equation.

$$\chi - \chi_0 = C/(T - \Theta_{CW}) \tag{2.5}$$

where χ_0, C, and Θ_{CW} are fitting parameters. The χ_0 gives information about the background in the measurement, C is used to calculate the μ_{eff} ($= \sqrt{8C}$), the absolute value of Θ_{CW} is the expected ordering temperature, and its sign refers to different types of magnetic order. $+$ and $-$ values for Θ_{CW} refer to FM and AFM, respectively. The effective magnetic moment can give us information about the spin configuration or spin-orbital state in a material. The Θ_{CW} is proportional to the strength of the interactions in a material. Magnetization as a function of temperature is measured under two different conditions: zero-field-cooled (ZFC) and field-cooled (FC). Any deviation of measured ZFC and FC data from each other can be a sign for spin-glass freezing behavior in a material which can be due to stacking fault disorders. A spin-glass behavior can be studied by measuring the AC magnetic susceptibility as a function of temperature under different applied frequencies.

Magnetization as a function of field- Magnetization as a function of magnetic field shows a linear behavior for materials with AFM order and a hysteresis for samples with FM order at base temperature. At base temperature, if the magnetization saturates at high enough applied magnetic fields, the saturation magnetization is the μ_{eff} in the material. Magnetization as a function of field also can show anomalies that are evidence for phase transitions.

2.4   Heat Capacity

The heat capacity measurement is a crucial measurement to obtain details about the lattice vibrations (phonon contribution), electronic, and magnetic properties of a material. The heat capacity measurements in this thesis are performed
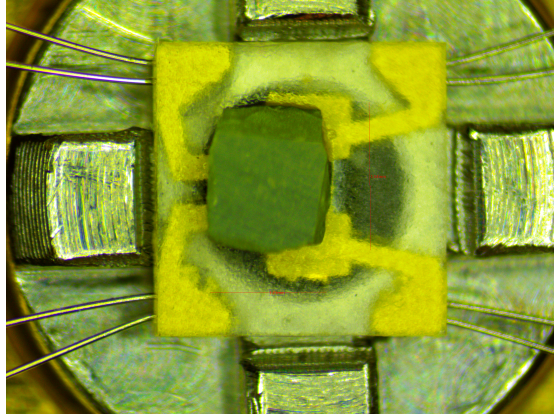
Figure 2.10: A rectangular shape pressed pellet sample is mounted on the sample platform on a heat capacity puck.

via a Physical Property Measurement System (PPMS) instrument. A small sample with a mass of 4 to 6 mg is placed on a calibrated heat capacity puck for measurements, Fig. 2.10. This puck has a sample platform made of sapphire which is connected to the puck via eight thin wires. These wires connect the sample and its platform to a thermal bath. To avoid the effect of noise on the measurement, this measurement has to be done at high vacuum. The first step for the measurement is to measure an addenda. The addenda measurement consists of running the heat capacity puck with a small amount of N-grease. Then the same measurement is repeated with a sample on the platform, with the N-grease helping to provide better thermal conductivity. The sample heat capacity as a function of temperature is measured by subtracting the addenda measurement from the measurement with the sample. The heat capacity measurement is at constant pressure. This quantity is measured via monitoring the changes in the temperature via applying heat pulses followed by a cooling process. The changes in the temperature of the sample/platform as a function of time is fitted to a function which then extracts the heat capacity [83].

The measured heat capacity of a sample contains information about different properties of the material. Sometimes it is necessary to isolate the magnetic

contribution to understand the ground-state of the studied material. There are three different approaches to subtract the phonon contribution from the total heat capacity. First: synthesizing a non-magnetic counterpart with the same crystal symmetry and the closest possible values of the lattice parameters. One of the main challenges for this method is that it is not always possible to prepare a non-magnetic analogue for our sample. Second: to estimate the phonon contribution in the very low temperature region by the Debye T^3 law which is only valid in the very low temperature limit. Third: the heat capacity of a non-magnetic sample can be calculated by first-principles which only requires having the CIF for the sample [63]. The phonon contribution to the heat capacity data can be subtracted by any of these methods to provide the magnetic heat capacity (C_m). The magnetic entropy can also be calculated from C_m, the area under a C/T vs. T curve.

$$S_m = \int\limits_{T_1}^{T_2} (C_m/T)dT \tag{2.6}$$

Both C_m and S_m are helpful to understand the ground-state of magnetic or magnetically disordered systems, specifically for the case of QSL candidates. Based on the theoretical simulations and calculations for a pure Kitaev Hamiltonian as well as for a generalized Kitaev and Heisenberg model, the general behavior of magnetic heat capacity, magnetic entropy and their characteristics are predicted [84, 85]. Thus, the heat capacity measurements allow us to compare the experimental results directly to theoretical analysis.

2.5 Resistivity

The resistivity measurement provides information about the electronic properties of a material. The same PPMS instrument provides resistivity measurements as well. The materials that I mainly studied during my Ph.D. research are Mott
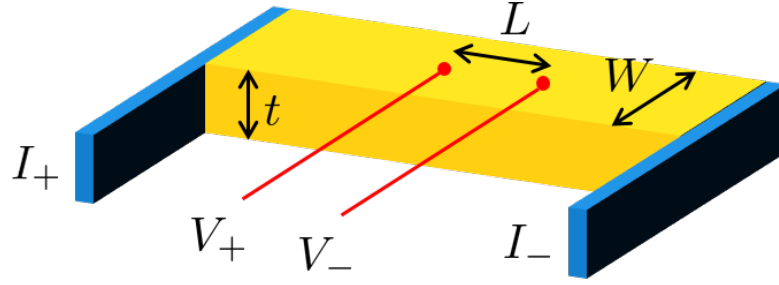
Figure 2.11: A schematic view of resistivity contacts on a sample.

insulators, and the resistivity as a function of temperature shows a quick upturn with decreasing temperature, a signature of saturation. For the measurement, four wires are used to make contacts with a sample on a resistivity puck. The current contacts are located on the edges of the sample and are affixed with silver epoxy to create a homogeneous electric field (E) in the sample, Fig. 2.11. Then, the voltage contacts are placed at the center of the sample far from the edges to make sure the voltage is measured in a homogeneous electric field. It is important that the voltage contacts have a small footprint on the sample to be able to accurately specify the distance between the contacts, length L, and to have them parallel and in the same direction as E (V = EL). The width (W) and thickness (T) of the sample are used to calculate the cross-sectional area (A). The resistivity measurement as a function of temperature is as follows:

- A fixed amount of current is applied to a sample. Based on the sample electronic properties an appropriate current is selected. For example, the current range for metals is between 100 to 1000 μA while this range is lower for insulators or oxides, 1 to 10 μA.

- The fixed current creates a homogeneous electric field (far from the edges) in the sample, then the instrument measures the changes in the voltage in the sample while the sample is cooling down and calculates the resistance (R) as a function of temperature.

41
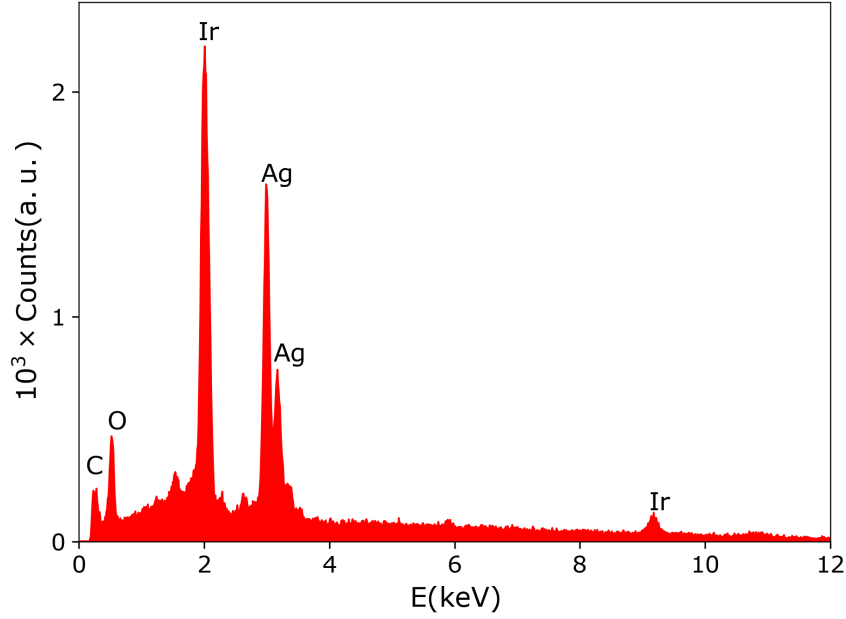
Figure 2.12: EDX spectrum of a pressed pellet sample of $Ag_3LiIr_2O_6$. The EDX measurement is not able to detect lithium atoms and also is not very accurate about the proportion of oxygen atoms.

- The resistivity can be calculated from the measured resistance with an additional geometry factor:

$$R = \rho L/A \tag{2.7}$$

- Before placing the resistivity puck in the instrument, the puck is placed on an user bridge device and the resistance of every two contacts are measured ($R_{contact1} + R_{sample} + R_{contact2}$) with an ohm meter to make sure the contacts are working properly.

2.6 Energy Dispersive X-ray Spectroscopy

Energy dispersive x-ray (EDX) spectroscopy is a characterization tool for determining the elemental composition of a material. This method, in addition to x-ray diffraction, provides information about the chemical formula or chemical composition of the studied material. EDX is also very helpful to probe any source

of impurities and evaluate a series of doped materials. Unfortunately, this method is not very useful for examining light elements such as Li or O atoms and it is very difficult to obtain reliable results for insulators. During EDX measurements, high-energy electron beams hit the sample and remove the core electrons (K, L, and M shells). Removing the electrons from the inner shells creates holes that higher level electrons can occupy after emitting specific x-ray energies. The emitted x-rays are detected and examined to provide information about the existing elements in the compound and their relative proportions. Figure 2.12 shows a measured spectrum of a pressed pellet sample of $Ag_3LiIr_2O_6$. The spectrum is as a function of energy. Each peak in the spectrum belongs to a specific element and is unique to that element. The peaks in the EDX spectrum are labeled based on the EDX periodic table information.

2.7 Raman Spectroscopy

Raman spectroscopy is an optical technique which is used to characterize materials. Incident light, typically from a laser, is inelastically scattered by interactions with lattice vibrations, resulting in scattered light that is no longer at the same wavelength as the incident light. The scattered light is collected as a function of wavelength or wavenumber to form a Raman spectrum, which is characteristic of each material. Peaks in the spectrum appear at the energies of the Raman active lattice vibrations for the material. From the CIF, one can predict the number and symmetries of such Raman active modes for a given material. If there are two different phases for a material that have different numbers of Raman modes, simply counting the number of peaks in the spectrum can reveal which phase (or phases) are present in a given sample. Raman scattering is very sensitive to the quality of the material surface. For single crystals, it is important that a high-quality surface is chosen to perform measurements.

43
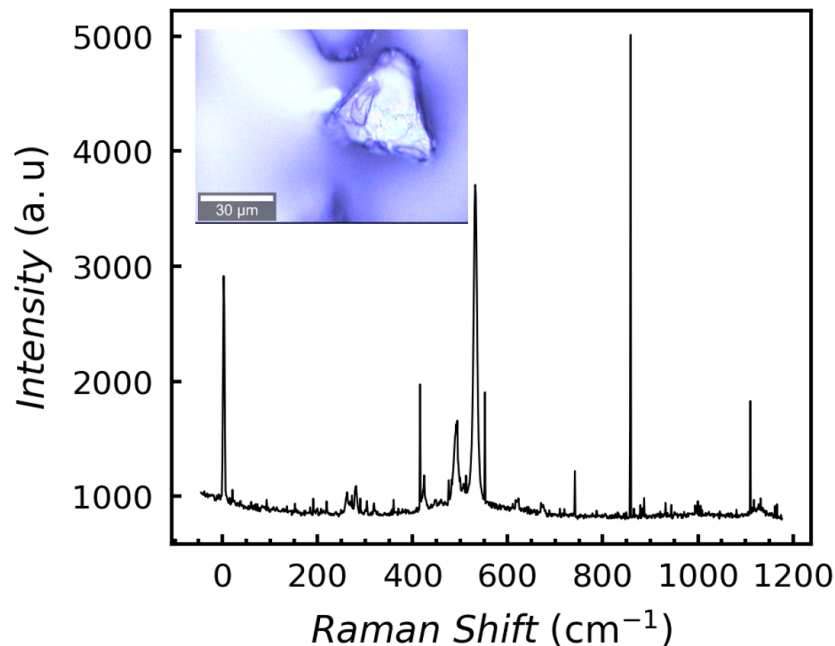
Figure 2.13: The Raman spectrum from a single crystal sample as a function of wavenumber. The inset shows the surface of the crystal. The sharp, single-data-point peaks are "cosmic rays", while the broader peaks correspond to actual excitations from the material.

Professor Kenneth Burch kindly allowed me to use the WITec alpha300R system in their glovebox for the measurement of single crystal samples. This system uses an unpolarized 532 nm laser (2.3 eV) and has objectives ranging from 5X to 100X for imaging and measuring the sample. When focused with the 100X objective, the spot size of the laser is $\sim 1~\mu$m. The Raman scattered light is collected in the backscattering geometry by the same objective used to focus the incident radiation, and the scattered light is then focused into a fiber optic cable that feeds into the spectrometer located outside of the globebox. Because of the small spot size, a relatively low power is used to avoid damaging the material, leading to integration times of $\sim$20 minutes. Several spectra are recorded for each sample and then averaged to remove any artifacts resulting from e.g. cosmic rays, Fig. 2.13.

CHAPTER III

Kitaev Spin-Liquid Candidate: Ag$_3$LiIr$_2$O$_6$

3.1 Introduction

An exciting frontier in condensed matter physics is to design materials where the spin degrees of freedom avoid magnetic ordering and form an entangled quantum ground-state known as a QSL [1–4]. Among different proposals to realize such a state, the Kitaev model is especially appealing due to having a QSL ground-state and for the possibility of engineering its features in real materials [20, 21, 23]. This theoretical model is defined on a honeycomb lattice with bond-dependent Ising interactions and has an exactly solvable Hamiltonian with a spin-1/2 degree of freedom. The 4d and 5d transition-metals, due to having a strong SOC effect, attracted a lot of attention as the candidate elements to build the honeycomb networks in real materials [21]. These magnetic elements can provide the magnetic anisotropy which is a prerequisite for a QSL. Experimental efforts to design honeycomb structure materials based on the Kitaev model led to the introduction of the first generation of honeycomb-layered compounds such as α-Li$_2$IrO$_3$, Na$_2$IrO$_3$, Li$_2$RhO$_3$, and α-RuCl$_3$ [35–40, 46, 51, 58, 86–88]. All these materials - despite promising thermodynamic properties, their proximity to the Kitaev QSL limit, and strong magnetic frustration - have a ground-state that is magnetically ordered and they thus fail to completely satisfy all the required criteria for this

model. Thus, a complete model Hamiltonian for the first generation Kitaev candidate must include non-Kitaev interactions:

$$\mathcal{H} = \sum_{\langle i,j \rangle \in \alpha\beta(\gamma)} \left[-K_\gamma S_i^\gamma S_j^\gamma + J\mathbf{S}_i \cdot \mathbf{S}_j + \Gamma \left(S_i^\alpha S_j^\beta + S_i^\beta S_j^\alpha \right) \right] \qquad (3.1)$$

where the Kitaev term (K) favors a QSL, the Heisenberg term (J) favors AFM order, and the off-diagonal exchange term (Γ) controls the details of the magnetic order [21, 89].

One of the successful methods to modify the magnetic interactions in favor of Kitaev interactions is the topo-chemical synthesis method. In this method, it is possible to structurally alter the inter-layer coordination while the honeycomb layers remain intact. In this chapter, I review my experimental methods and results for the synthesis and characterization of a new Kitaev candidate, $Ag_3LiIr_2O_6$. I used α-Li_2IrO_3 as a parent compound and modified its crystal structure in favor of Kitaev interactions. In order to enhance the Kitaev interactions, I replaced the inter-layer atoms in the parent compound via a topo-chemical synthesis method and synthesized $Ag_3LiIr_2O_6$. This novel Kitaev QSL material shows a lower transition temperature while retaining all of the promising features of its parent compound. The results of this chapter are published in Ref. [44, 59, 64].

3.2   Background

One of the most promising Kitaev candidate materials that has been heavily studied over the past two decades is α-Li_2IrO_3 [35, 36, 51]. This honeycomb-layered compound contains edge-sharing IrO_6 octahedra in the form of honeycomb networks with a Li atom at the center of each hexagon and thus constitutes a honeycomb structure as required for a Kitaev material. The honeycomb layers in this Mott insulator are connected via octahedrally coordinated LiO_6, with the inter-

layer Li atoms connected to three O atoms on the top and three O atoms on the bottom. Strong chemical bond coordination between the honeycomb layers and inter-layer atoms reduces the inter-layer spacing between the honeycomb layers. The magnetic element, Ir^{4+}, provides effective magnetic moments for a pseudospin $J_{eff} = 1/2$ state in the presence of octahedral CEF and strong SOC. This feature is also experimentally confirmed by a CW analysis of the paramagnetic region of the measured magnetic susceptibility. The results of both magnetization and heat capacity measurements on α-Li_2IrO_3 indicate a long-range AFM order at $T_N = 15$ K [35, 36]. High-temperature magnetic susceptibility measurements up to 1000 K give a CW temperature $\Theta_{CW} = -105$ K [36]. Although α-Li_2IrO_3 is magnetically ordered at low temperatures, the magnetic frustration between different exchange interactions in the material leads to a reduction of the actual ordering temperature (T_N) compared to the expected ordering temperature (Θ_{CW}). The magnetic frustration parameter ($f = \frac{|\Theta_{CW}|}{T_N}$), which is the ratio of the CW temperature and T_N, can provide an estimate of the strength of the magnetic frustration in a material [35]. A significant difference between the CW temperature and T_N, as shown by $f = 7$, is indicative of magnetic frustration in α-Li_2IrO_3. Despite the fact that the ground-state of α-Li_2IrO_3 shows a long-range magnetic order, the structural properties, its spin-orbital state, and the presence of strong magnetic frustration in the compound make it a desirable Kitaev candidate.

In addition to the structural and thermodynamic analyses that suggest the proximity of α-Li_2IrO_3 to a QSL limit, the magnetic heat capacity (C_m) and magnetic entropy (S_m) in this compound are also qualitatively consistent with quantum Monte Carlo (QMC) simulations for a pure Kitaev model [84] and theoretical calculations on a generalized Kitaev-Heisenberg model [85]. The Kitaev model is exactly solvable via fractionalization of $S = 1/2$ particles located on the vertices of each hexagon into itinerant and localized Majorana fermions. The

QMC simulations investigated the effect of spin fractionalization on the heat capacity and entropy in the presence of only Kitaev interactions in a honeycomb structure. This study predicted a two-peak behavior for the heat capacity, where each peak refers to a crossover and thermal excitation of itinerant or localized Majorana fermions. The high-temperature (T_H) crossover refers to the enhancement of nearest-neighbor or short-range spin correlations in the system, and it is described by itinerant fermions. The low-temperature (T_L) peak is indicative of thermal fluctuations of localized Majorana fermions and is a signature of incipient alignment of hexagon plaquette operators or fluxes in the system. The calculated entropy based on the heat capacity simulations shows a two-step behavior and release at about $1/2 \ln(2)$ value for each crossover [84]. The theoretical calculations for a generalized Kitaev-Heisenberg system suggest that the two-peak behavior survives in heat capacity in the magnetically ordered materials which are close to Kitaev QSL phase; however, the plateau-like behavior could be replaced by a shoulder-like behavior for this limit [85]. The magnetic heat capacity data for α-Li$_2$IrO$_3$ displays a two-peak behavior as is predicted for magnetically ordered materials close to the Kitaev QSL limit. A shoulder-like behavior between the two crossovers is observed in this compound, consistent with the theoretical calculations for a Kitaev-Heisenberg model [36]. The experimental observations in support of the proximity of α-Li$_2$IrO$_3$ to the Kitaev QSL limit proves this Kitaev candidate material can be a promising honeycomb system to tune its magnetic interactions and push it even closer to the ideal QSL limit by lowering its ordering temperature.

3.3 Methods

3.3.1 Material Synthesis

The preparation of high-quality $Ag_3LiIr_2O_6$ samples has two main steps. The first step is synthesizing a high-quality parent compound, α-Li_2IrO_3, via a solid-state reaction at high-temperature (T $\geq$ 800 °C) [34]. A mixture of Li_2CO_3 and IrO_2 with molar ratio of 1.2:1 and total mass of 350 mg are pressed into a loose pellet. The pellet is then placed into an alumina crucible in a furnace set at 150 °C to avoid evaporation of Li_2CO_3. The furnace is heated to 900 °C at a rate of 5 °C/min and stays at 900 °C for 16 hours, before cooling down to 600 °C. The sample is then quenched in an antechamber filled by Ar gas. The x-ray diffraction (XRD) pattern of a typical sample at this stage is presented in Fig. 3.1 (black pattern). The first step should be short to avoid any un-reacted IrO_2 impurities (a peak at 28° is indicative of this kind of impurity). After the first round of heating, the superstructure peaks between 20° and 30° (the honeycomb ordering peaks) are still not well-separated, which means the honeycomb structure is weak and the material has a high level of stacking faults. In order to increase the honeycomb-ordering quality and remove stacking faults in α-Li_2IrO_3, it is necessary to perform successive stages of grinding and heating. These reheating steps are performed in the range of 950 °C and 1015 °C for 16−24 hours. After several rounds of annealing, which varies based on the humidity level in the lab, a high-quality sample of α-Li_2IrO_3 is created, Fig. 3.1 (green pattern). Typically, improving the quality of the parent compound will directly improve the quality of the product material and decrease the level of stacking faults and the possibility of having rows of unwanted atoms in the honeycomb layers of the product compound.

The second step is a topo-chemical exchange reaction. During this process, the main goal is to keep the structure of the honeycomb layers unchanged and
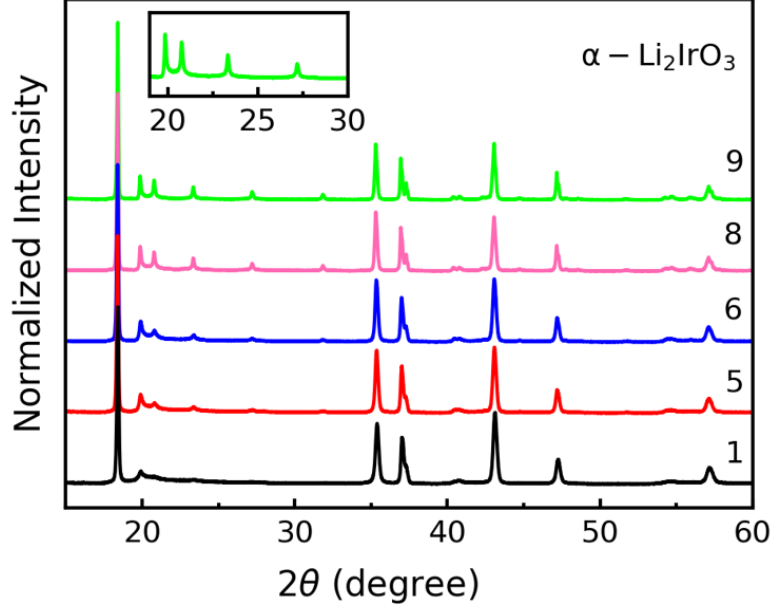
Figure 3.1: After each heat cycle, the powder x-ray pattern of α-Li$_2$IrO$_3$ shows more pronounced peaks, especially between 20° and 30° degrees where the honeycomb Bragg peaks appear. The number of times each sample has been reheated is shown on the right above its respective pattern.

to only alter the inter-layer atoms and their coordination. The topo-tactic cation exchange reaction must be conducted at low temperatures (T $\leq$ 400 °C), since higher temperatures will decompose the metastable product [55, 63, 90]. The poly-crystalline samples of Ag$_3$LiIr$_2$O$_6$ were synthesized with mixtures of high-quality α-Li$_2$IrO$_3$ samples and AgNO$_3$. A total mass of 350 mg of starting materials are mixed according to Eq. (3.2) with 50% excess silver nitrate.

$$2\,\text{Li}_2\text{IrO}_3 + 3\,\text{AgNO}_3 \longrightarrow \text{Ag}_3\text{LiIr}_2\text{O}_6 + 3\,\text{LiNO}_3 \tag{3.2}$$

The mixture was pressed into a hard pellet and placed into a small alumina crucible inside a quartz tube. The quartz tube was sealed under Ar gas pressure to avoid decomposition of the AgNO$_3$. The pressed pellet was heated to 350 °C at a rate of 1 °C/min. It remained at 350 °C for seven days and was then cooled down to room temperature at the same rate [44, 59, 70]. In order to remove the excess AgNO$_3$,

the sample was placed into a beaker filled with deionized water for 20 minutes, then washed with deionized water three times, and dried at room temperature under vacuum for an hour. The black powder sample is fairly air sensitive and can only be exposed to air for a couple of hours. Exactly the same procedure was repeated to synthesize the non-magnetic compound $Ag_3LiSn_2O_6$ with parent compound Li_2SnO_3.

3.3.2 Crystal Structure Analysis: Rietveld Refinement

One of the essential material characterization tools to identify the quality of prepared materials is XRD measurements. This is particularly the case for a layered material with complex structural properties like α-Li_2IrO_3, for which the synthesis conditions in each annealing step are modified based on the measured x-ray pattern. After perfecting the quality of the synthesized material, α-Li_2IrO_3 or $Ag_3LiIr_2O_6$, a high resolution x-ray pattern scan is collected from a well-ground powder sample to perform a Rietveld refinement analysis. The signatures of the honeycomb structure in both compounds can be found via the Bragg peaks in the range of 19° to 26°. Using the topo-chemical exchange reaction helps to maintain the honeycomb structure while modifying the inter-layer structure. Among all the possible space groups, only space group No. 12 ($C2/m$) and space group No. 15 ($C2/c$) can be indexed for all the Bragg peaks, including the honeycomb peaks in the region 19−30° for α-Li_2IrO_3 and the asymmetric peak in the region 19−22° for $Ag_3LiIr_2O_6$, Fig. 3.2. The advantage of the $C2/m$ model is that it offers a simpler model with a smaller unit cell compared to the $C2/c$ model, which ultimately makes calculations easier [63]. Therefore, we report the correct space group for $Ag_3LiIr_2O_6$ to be $C2/m$, similar to its parent compound [34] as well as other honeycomb-layer oxides with similar structures [91, 92]. Table 3.1 summarizes the unit cell parameters and the quality factors for the Rietveld refinement. The
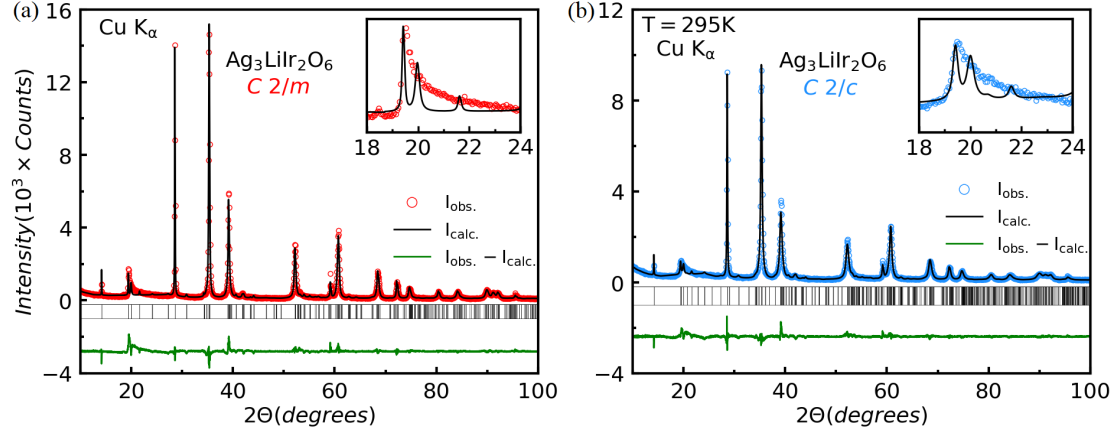
Figure 3.2: Rietveld refinements of the PXRD pattern for $Ag_3LiIr_2O_6$ using $C2/m$ (a) and $C2/c$ (b) models. The broad asymmetric peak in the inset is due to the honeycomb ordering. Stacking disorder is responsible for the asymmetric broadening of the honeycomb peaks.

Table 3.1: Unit cell and Rietveld refinement quality factors are reported for $Ag_3LiIr_2O_6$ at room temperature.

Unit cell parameters		Refinement parameters	
Space Group	$C2/m$	Parameters	24
a (Å)	5.28317(8)	R_{Bragg} (%)	8.51
b (Å)	9.13552(19)	R_F (%)	4.36
c (Å)	6.48594(11)	R_{exp} (%)	5.30
β (°)	74.28970(231)	R_p (%)	9.21
V (Å^3)	301.347	R_{wp} (%)	14.0
Z	2	χ^2	7.0
ρ (g cm^{-3})	8.946	T (K)	295

PXRD data were taken at room temperature on a powder specimen using a Bruker D8 ECO instrument equipped with a copper x-ray source (Cu Kα), a nickel filter to absorb the Kβ radiation, and two 2.5° Soller slits after the source and before the LYNXEYE XE 1D energy-dispersive detector. The FullProf suite and VESTA software were used for the Rietveld refinements and crystal visualizations [76, 81]. Table 3.2 summarizes the atomic coordinates, Wyckoff-site occupancies, and the Debye-Waller factors in the Rietveld refinement of $Ag_3LiIr_2O_6$. An artificial mixing between Ir and Li atoms is introduced in sites $4g$ and $2a$ to account for the stacking faults, similar to the reported refinement of α-Li_2IrO_3 [34].

Table 3.2: Atomic coordinates, site occupancies, and the isotropic Debye-Waller factors ($B_{iso} = 8\pi^2 U_{iso}$) for the Rietveld refinement of $Ag_3LiIr_2O_6$.

atom	site	x	y	z	occ.	B_{iso} (Å^2)
Ag1	$4h$	1/2	0.31732(30)	1/2	1.000	0.35
Ag2	$2d$	0	1/2	1/2	1.000	0.35
Ir1	$4g$	0	0.66914(23)	0	0.802	0.25
Li1	$4g$	0	0.66914(23)	0	0.196	0.25
Ir2	$2a$	0	0	0	0.388	0.27
Li2	$2a$	0	0	0	0.612	0.27
O1	$8j$	0.38800	0.3314	0.8324	1.000	0.4
O2	$4i$	0.1090	1/2	0.1670	1.000	0.4

3.3.3 Characterization Measurements

DC magnetization measurements were performed on $\sim$30 mg powder samples of α-Li_2IrO_3 and $Ag_3LiIr_2O_6$ packed in a VSM Powder Sample Holder and mounted in a MPMS3 Brass Half-tube Sample Holder in a Quantum Design MPMS3.

Heat capacity measurements were performed on a rectangularly shaped piece of pressed pellet with total mass of $4-5$ mg with the relaxation time method in a Quantum Design PPMS Dynacool. To obtain the magnetic heat capacity (C_m), the total heat capacity of $Ag_3LiIr_2O_6$ and $Ag_3LiSn_2O_6$ were measured separately and then subtracted after considering the molar mass correction.

The muon spin relaxation (μSR) experiments were carried out at the Paul Scherrer Institute (PSI) using a ^{3}He refrigerator with the Dolly Multi Purpose Surface-Muon Instrument and a gas flow cryostat with the General Purpose Surface-Muon (General Purpose Surface-Muon (GPS)) Instrument. The MUSRFIT program [93] was used for data analysis. The polycrystalline samples were pressed into pellets 13 mm in diameter and 1 mm thick. The pellet was wrapped in 25-μm thick silver foil and mounted with varnish on copper holders[1].

The ED and HAADF-STEM were performed using an aberration-corrected

---

[1]The μSR experiments and its analyses were performed by Dr. E. Kenney, Dr. C. Wang, and Prof. M. Graf.

JEM ARM200F microscope[2].

3.4 Results and Discussion

3.4.1 Crystal Structure

Figure 3.3 shows the crystal structures of the parent compound, α-Li_2IrO_3, and the exchange system, $Ag_3LiIr_2O_6$. Both materials show a similar honeycomb structure with Ir^{4+} honeycomb networks. The honeycomb layers in the parent compound are connected via octahedrally coordinated inter-layer Li atoms with an inter-layer spacing of 4.83 $\mathring{A}$. After the cation exchange reaction, the inter-layer Li atoms are replaced by linearly coordinated Ag atoms in $Ag_3LiIr_2O_6$. In the Ag-exchange material, each Ag atom is connected to one O atom on top and one O atom on the bottom; therefore, the inter-layer connection in $Ag_3LiIr_2O_6$ is weaker and leads to a 30% increase (d = 6.24 $\mathring{A}$) in the inter-layer spacing compared to the parent compound. A weaker inter-layer connection between the honeycomb layers in $Ag_3LiIr_2O_6$ enhances the stacking faults, as well as the trigonal distortion in the octahedral environment of the Ir atoms. The structural modification of α-Li_2IrO_3 affects the magnetic properties of $Ag_3LiIr_2O_6$ and lowers the ordering temperature.

3.4.1.1 Trigonal Distortion

Ir atoms are octahedrally coordinated with six O atoms (IrO_6) in both α-Li_2IrO_3 and $Ag_3LiIr_2O_6$. In the ideal case, the O-Ir-O bond angles are 90° in an octahedron. However, deviations of the bond angles from the ideal values are expected to be observed in a real material, which is referred to as trigonal

---

[2]Dr. O. Lebedev performed the TEM measurements and analyzed the results.
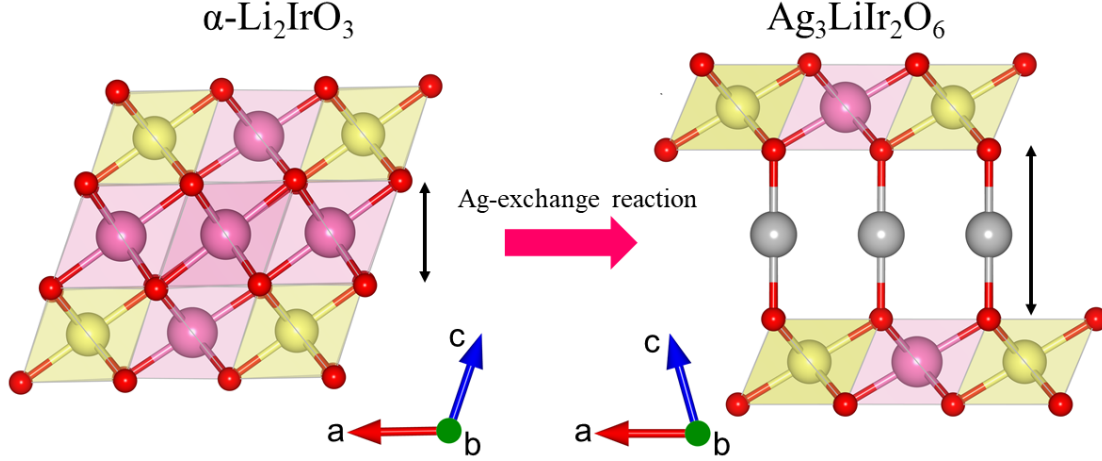
Figure 3.3: The octahedral coordination of Li atoms between the layers of α-Li$_2$IrO$_3$ (left) and linear (dumbbell) coordination of Ag atoms between the layers of Ag$_3$LiIr$_2$O$_6$ (right) which leads to an increase of the inter-layer separation. The yellow, pink, red, and grey spheres are Ir, Li, O, and Ag atoms, respectively.

distortion. Trigonal distortion can be quantified by the bond angle variance [49],

$$\sigma = \sqrt{\frac{\Sigma_i(\phi_i - \phi_0)^2}{(m-1)}} \tag{3.3}$$

where m and ϕ_0 are the number and ideal value of O-Ir-O bond angles in an octahedron without distortion, respectively. The ϕ_i values are calculated from the CIF of both iridate compounds, Fig. 3.4. The bond angle variance σ is 3.46(1)° for α-Li$_2$IrO$_3$ and 6.39(1)° for Ag$_3$LiIr$_2$O$_6$. Trigonal distortion is two times larger in the Ag-exchange compound. One can expect an enhancement in the influence of off-diagonal exchange coupling and a significant difference between the magnetic behavior of parent and exchange compounds due to a stronger trigonal distortion in Ag$_3$LiIr$_2$O$_6$. However, iridates have very strong SOC; thus, the effect of trigonal distortion on the magnetic properties of the iridate materials are negligible.
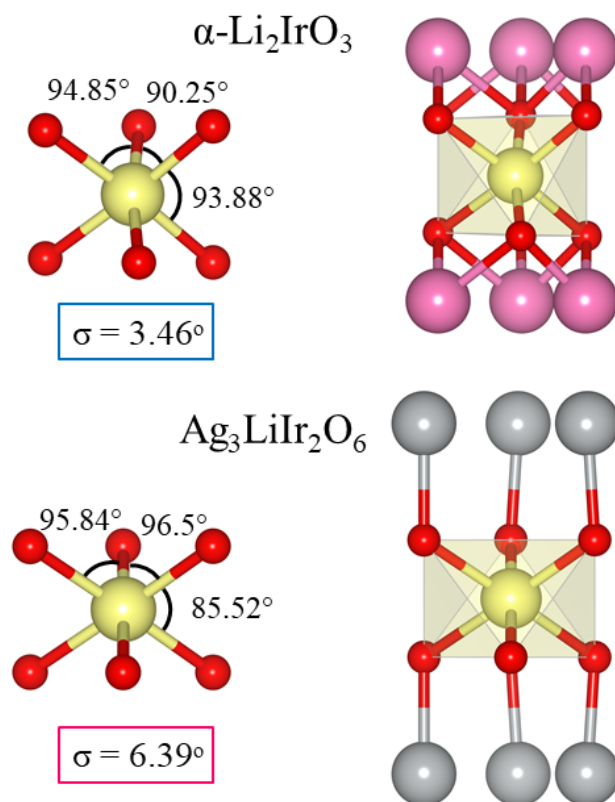
Figure 3.4: The bond angle values and inter-layer connections between Ir atoms and inter-layer Li and Ag atoms in α-Li$_2$IrO$_3$ and Ag$_3$LiIr$_2$O$_6$ are presented, respectively. Changing the inter-layer chemistry from octahedrally coordinated Li atoms (stronger connection) in α-Li$_2$IrO$_3$ with a weaker linear bond connection in Ag$_3$LiIr$_2$O$_6$ moves the O atoms towards the honeycomb layers and increases the trigonal distortion in the Ag-exchange compound.

3.4.2 Magnetism

The DC magnetic susceptibility as a function of temperature is measured at 0.2 T, as shown in Fig. 3.5(a). The first evidence of magnetic ordering in a high-quality $Ag_3LiIr_2O_6$ sample is a downturn at $T_N = 14$ K. To more clearly illustrate the low-temperature region, we magnified the magnetic susceptibility data for T $\leq T_N$ in Fig. 3.5(b). A similar behavior was observed in an earlier work by Todorova *et al.* [70]. The peak is broad and shows splitting between the ZFC and FC conditions (Fig 3.6) and suggests a trace of spin-glass like freezing. This splitting between ZFC and FC curves is only 2% of the total magnetization data; thus, it originates from a minority of frozen spins due to stacking faults in this layered compound. The DC magnetic susceptibility (ZFC and FC) is measured at higher applied fields (Fig. 3.6) which leads to a decrease in the splitting, but the gap is not fully closed which confirms a static freezing at the ordering temperature, T_N [94, 95].

A second anomaly in Fig. 3.5(b) is indicative of a long-range magnetic order, $T_{LRO} = 8$ K, below which the susceptibility visibly turns down. We thus identify T_N as the onset temperature for short-range magnetic ordering that becomes long-range below T_{LRO}. After considerable effort to remove disorder and improve the quality of $Ag_3LiIr_2O_6$, we were able to resolve the AFM peak in the high-quality sample.

To understand the magnetic interactions in $Ag_3LiIr_2O_6$, we performed a CW analysis on the inverse susceptibility $(1/\chi)$ for T ≥ 150 K in Fig. 3.5(a). The yellow line represents the CW fit to the $[1/(\chi - \chi_0) = (T - \Theta_{CW})/C]$ equation, where χ_0, Θ_{CW}, and C are fit parameters. The CW analysis of the paramagnetic region yields a CW temperature $\Theta_{CW} = -132(1)$ K and magnetic moment $\mu_{eff} = 1.87(2)\mu_B$. The negative sign of Θ_{CW} indicates AFM interactions, and its large magnitude compared to T_N implies magnetic frustration ($f = 9.5$). The CW
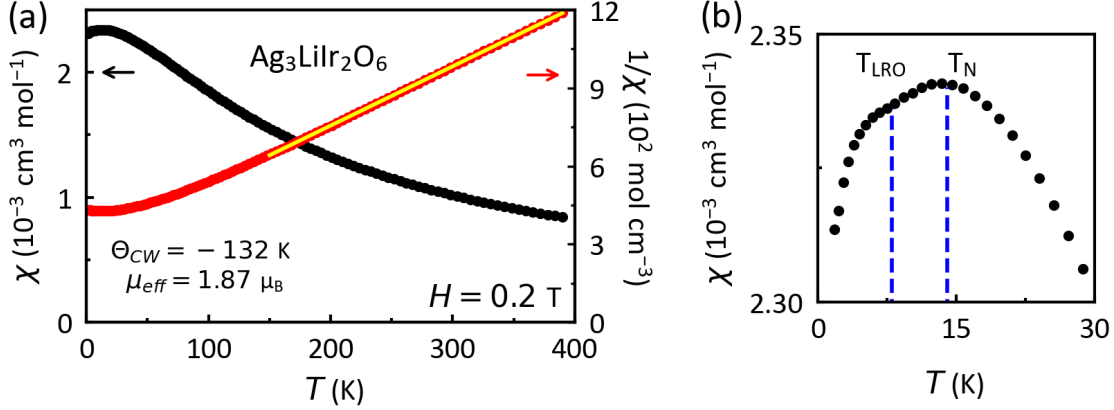
Figure 3.5: (a) DC magnetic susceptibility per mole of Ir (black data) and inverse susceptibility (red data) plotted as a function of temperature in the high-quality sample. The yellow line is a CW fit at T > 150 K. The solid and open circles in the inset represent the ZFC and FC curves at H = 5 T. (b) Magnified view of the ZFC susceptibility showing a broad peak at $T_N = 14$ K and a sharper downturn at $T_{LRO} = 8$ K.

temperature and magnetic moment for the parent compound are $\Theta_{CW} = -105(2)$ K and $\mu_{eff} = 1.83(5)\mu_B$, respectively [35, 36]. We extract an effective magnetic moment ($\mu_{eff} = 1.87\mu_B$) for $Ag_3LiIr_2O_6$, comparable to the reported values in α-Li_2IrO_3, and close to the expected moment for a $J_{eff} = 1/2$ state ($1.74\mu_B$). A similar CW temperature in both compounds also suggests a comparable strength of the Heisenberg exchange interaction [59].

In Fig. 3.7, the magnetic field dependence of the magnetization in $Ag_3LiIr_2O_6$ is presented at 2 K for fields up to 7 T. The magnetization reaches $0.03\mu_B$ and does not saturate even up to 7 T. In order to achieve saturation of the magnetization, higher magnetic fields are required. The magnetization data has a linear behavior, confirming the AFM interactions in this Kitaev magnet.

3.4.3 Heat Capacity

As noted in Section 3.2, QMC simulations suggest that a Kitaev magnet releases the spin entropy in two successive crossovers resulting in high-temperature (T_H) and low-temperature (T_L) peaks in the magnetic heat capacity [84, 85].
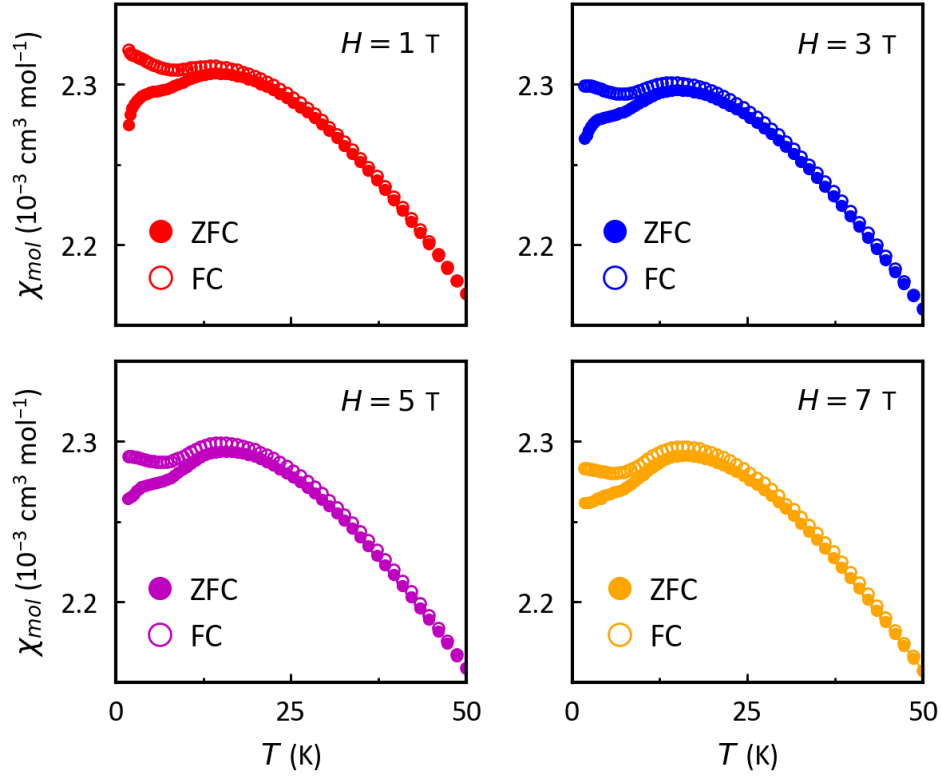
Figure 3.6: The splitting between ZFC (solid circles) and FC (open circles) susceptibility curves at 1, 3, 5, and 7 T. The splitting decreases by increasing the applied field.
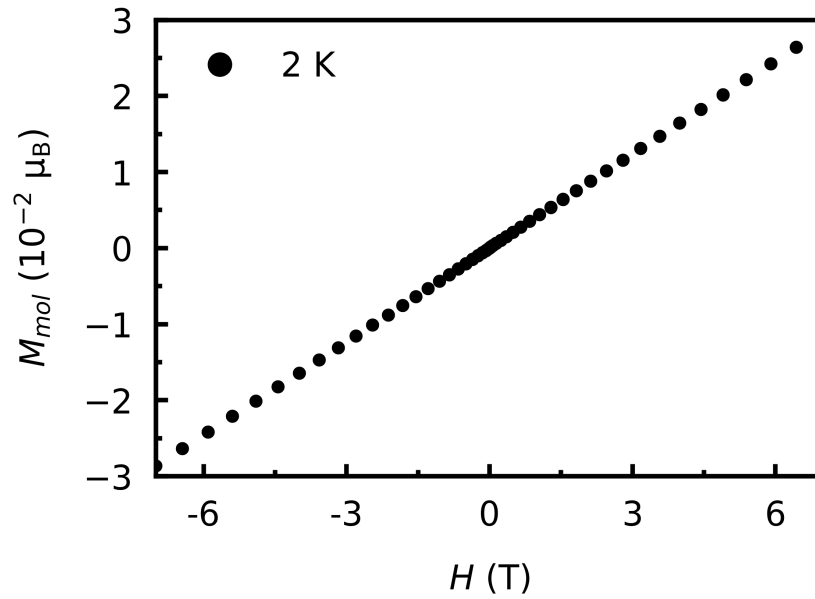
Figure 3.7: Magnetization as a function of magnetic field is shown at temperature 2 K up to 7 T.
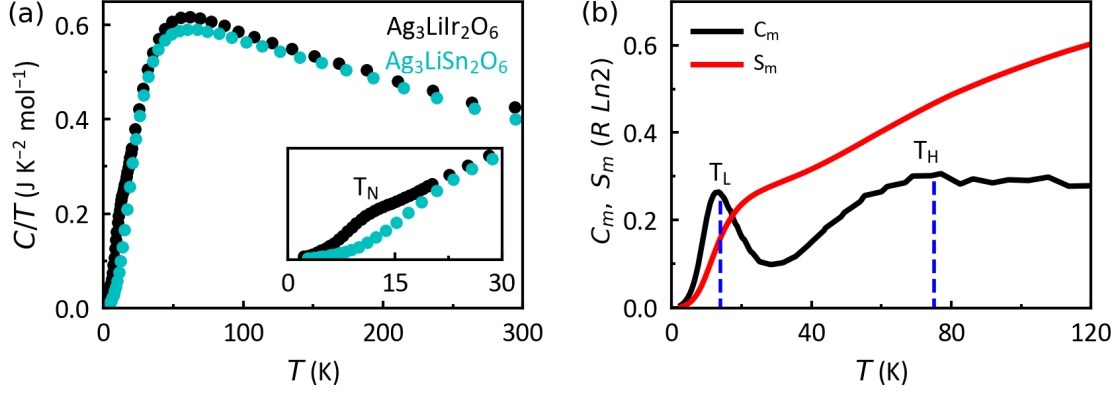
Figure 3.8: (a) Heat capacity divided by temperature (C/T) per mole of Ir or Sn plotted as a function of temperature in $Ag_3LiIr_2O_6$ (black data) and its non-magnetic lattice model, $Ag_3LiSn_2O_6$ (turquoise data). (b) Magnetic heat capacity C_m and entropy S_m in units of $R\ln(2)$ as a function of temperature below 120 K, where $T_L = T_N = 14$ K and $T_H = 75$ K.

The experimental results for α-Li_2IrO_3 are qualitatively in agreement with this theoretical prediction [36] and show a two-peak behavior in C_m. We measured the heat capacity (C) of a high-quality sample of $Ag_3LiIr_2O_6$ to confirm the bulk AFM order in $Ag_3LiIr_2O_6$ and to study the behavior of the magnetic heat capacity in the Ag-compound. Figure 3.8(a) shows a broad peak in C/T at $T_N = 14$ K, consistent with the peak at 14 K in $\chi(T)$. In the same panel we also present the heat capacity of an isostructural compound, $Ag_3LiSn_2O_6$, which serves as a non-magnetic lattice model for $Ag_3LiIr_2O_6$ to isolate the magnetic contribution of the heat capacity.

The two data sets closely track each other as a function of temperature except near 75 K (T_H) and 14 K (T_L), where an additional magnetic contribution enhances the heat capacity of $Ag_3LiIr_2O_6$. The magnetic heat capacity (C_m) can be isolated by subtracting the $Ag_3LiSn_2O_6$ data (a model for the phonon background) from $Ag_3LiIr_2O_6$, Fig. 3.8(b) (black curve). The obtained C_m is used to calculate the magnetic entropy via $S_m = \int (C_m/T)dT$. Figure 3.8(b) shows C_m and S_m in units of $R\ln(2)$ as a function of temperature where two broad peaks are resolved at $T_H = 75$ K and $T_L = 14$ K in C_m, and a two-step structure is

seen in S_m. The behavior of C_m and S_m is qualitatively consistent with QMC simulations and very similar to the results reported for the parent compound [36]. According to the theoretical prediction [84, 85], the entropy release at each step must be $1/2R\ln(2)$, but we observe $\sim 60\%$ of this value. A similar observation was reported for the parent compound and the quantitative disagreement was attributed to the phonon background subtraction. It is possible that $Ag_3LiSn_2O_6$ is not a perfect lattice model for $Ag_3LiIr_2O_6$ due to small differences in the lattice parameters and the masses of Ir and Sn.

Such a two-peak behavior has been interpreted as evidence of a fractionalization of spins into Majorana fermions at T_H followed by a long-range entanglement at T_L in $Ag_3LiIr_2O_6$, α-Li_2IrO_3, Na_2IrO_3, and α-$RuCl_3$ [36, 59, 96], based on the QMC simulations of the Kitaev Hamiltonian with only the pure Kitaev interaction. We caution against this interpretation and point out that the peak at $T_L = T_N$ in $Ag_3LiIr_2O_6$ is due to static magnetism instead of quantum entanglement, while the onset of static magnetism starting at 14 K is confirmed in magnetization data. Similarly, the low-temperature peaks in the heat capacity of α-Li_2IrO_3, Na_2IrO_3, and α-$RuCl_3$ are due to AFM ordering [36, 96]. The above discussion does not discredit the iridate materials as candidates for a Kitaev QSL - the peak at T_H may indeed signal the onset of a fractionalization process. But, the Majorana liquid would develop an instability toward a gapped AFM state instead of melting into an entangled spin liquid ground state. Ideally, the ratio of T_L/T_H should be less than 0.03 for a Kitaev spin-liquid [84], whereas $T_L/T_H = 0.18$ in $Ag_3LiIr_2O_6$. Therefore, the T_L might occur at very low temperatures below our measurement capabilities and the presently identified T_L refers to AFM ordering in the compound.

The heat capacity of $Ag_3LiIr_2O_6$ is also measured under different applied fields to study the stability of the AFM transition, Fig. 3.9(a). The AFM peak in the Ag-compound is very robust and does not change when increasing the magnetic field.
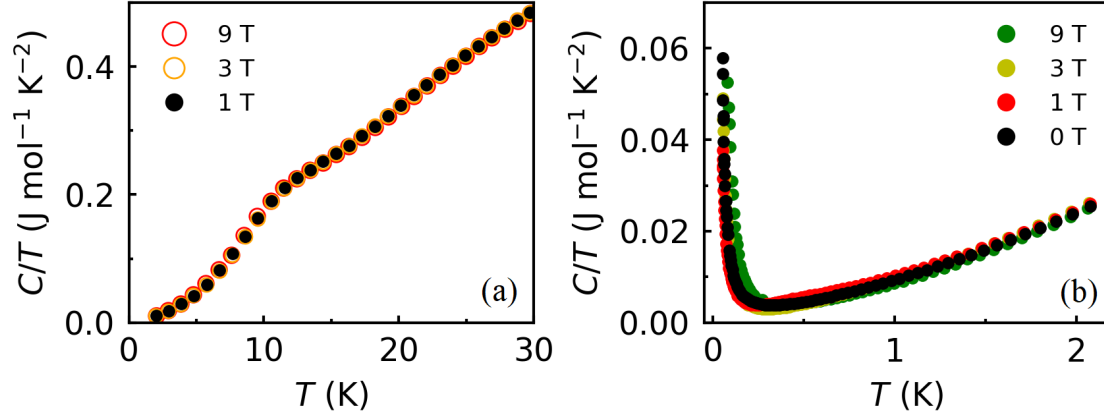
Figure 3.9: (a) The heat capacity in $Ag_3LiIr_2O_6$ is measured at 1, 3, and 9 T. (b) The heat capacity as a function of temperature from 2 K down to 52 mK at 0, 1, 3, and 9 T.

In α-RuCl$_3$, the AFM transition peak was removed by applying a 7 T magnetic field parallel to the honeycomb layers [97]. A similar effect may be observed in $Ag_3LiIr_2O_6$ once single crystals are available.

The heat capacity is measured down to 52 mK, Fig. 3.9(b). The heat capacity (C/T) shows a linear behavior ($\sim T$) at low temperature, similar to what is observed for α-Li$_2$IrO$_3$, and suggests an unusual magnetic excitation in these compounds [36]. A similar upturn is also observed in the parent compound due a nuclear Schottky anomaly which is also present in the Ag-compound [36].[3]

3.4.4 Muon Spin Relaxation

In positive muon spin relaxation (μ^+SR), spin-polarized positive muons are injected into a sample and in less than 1 ps come to rest at a preferred crystallographic interstitial site (or sites). The muon spin polarization then evolves with time in the local magnetic field, yielding information about the magnitude and orientation of the local field relative to the initial spin direction. After tens of millions of decay events, a time histogram can be used to extract the asymmetry,

---

[3]The heat capacity experiments at low temperature were performed by Sangyun Lee and Dr. Roman Movshovich.

which is proportional to the time dependence of the projection of the muon spin along the detector direction [98]. The asymmetry contains information about the local field's temporal and spatial variation. We plot the asymmetry as a function of time in a high-quality sample in Fig. 3.10 at nine representative temperatures from 0.28 to 20 K at zero field. For temperatures greater than or equal to 20 K, the Ir^{4+} moments are fluctuating too rapidly, and they have no effect on the muon. Therefore, the depolarization is dominated by randomly oriented quasi-static nuclear moments. The temperature dependent asymmetry is well described by a Gaussian Kubo-Toyabe function

$$A_{\mathrm{KT}}(t) = A_0 \left[\frac{1}{3} + \frac{2}{3} \left(1 - \sigma^2 t^2 \right) \exp\left(-\frac{1}{2}\sigma^2 t^2 \right) \right] \tag{3.4}$$

where $A_0 = 0.174$ is the initial asymmetry for GPS in spin-rotated mode, and the parameter $\sigma = 0.150$ MHz is proportional to the second moment of the field distribution experienced by the muon ensemble. The magenta line on Fig. 3.10 is a fit to Eq. 3.4 at 20 K. We found a constant value for σ between 200 and 20 K, indicating that the muon is not diffusing in this temperature range and there is no sign of magnetic order in the material. The data below 20 K can be explained in three regions of interest.

Region 1. For 20 K$> T > T_N$, depolarization is dominated by the nuclear moments. The electronic moments are slowing down and begin contributing to muon depolarization.

Region 2. For the range $T_N > T > T_{\mathrm{LRO}}$, depolarization is dominated by the electronic moments. Short-range correlations are manifested in the onset of a fast relaxation component in addition to a slow exponential depolarization due to fluctuations. To characterize the crossover in this temperature range, we use a
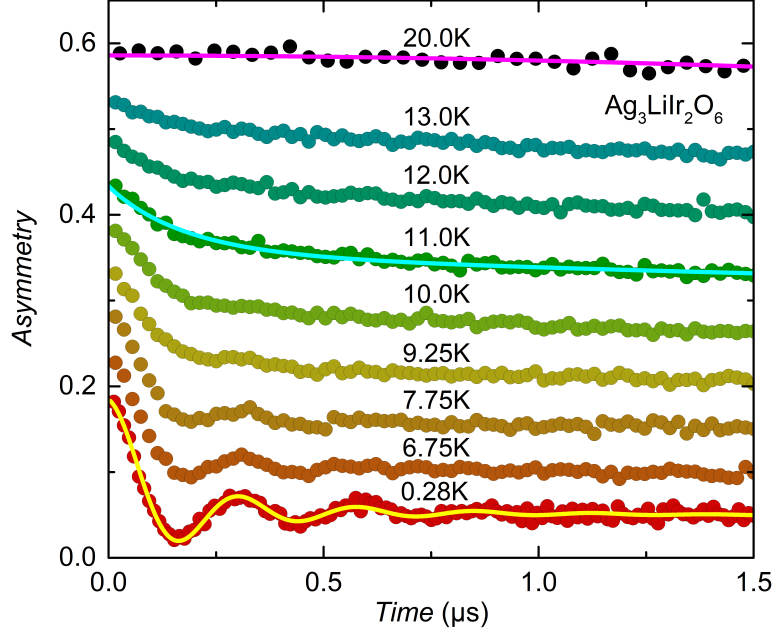
Figure 3.10: Asymmetry plotted as a function of time at short timescales. The curves have been offset by equal increments from the base-temperature curve (0.28 K) for clarity. The magenta, cyan, and yellow solid lines are fits to Eq. 3.4, Eq. 3.5, and Eq. 3.6, respectively.

phenomenological depolarization function

$$A(t) = A_0 \left[\alpha_F \exp\left(-\left(\lambda_F t\right)^\beta\right) + (1 - \alpha_F) \exp\left(-\lambda_{St}\right) \right] \tag{3.5}$$

where $A_0 = 0.185$ is the initial asymmetry in the Dolly spectrometer in spin-rotated mode. The first term in the brackets is related to the fast decay with rate λ_F best described by a stretched exponential with exponent β, and attributed to spin freezing. The second term is a slow exponential decay at rate λ_S attributed to a fluctuating contribution. The fit parameters λ_F, β, and λ_S in the high-quality sample vary from 10.1(6) μs^{-1}, 0.85(6), and 0.211(2) μs^{-1} at 13 K, respectively, to 11.0(1) μs^{-1}, 1.75(5), and 0.285(8) μs^{-1} at 8 K. The cyan line on Fig. 3.10 is a representative fit to Eq. 3.5 at 11 K. From such fits, we extract the fraction of fast decay α_F, which we take as a metric for the onset of static magnetism. The temperature dependence of α_F is plotted in Fig. 3.11, and it vanishes near
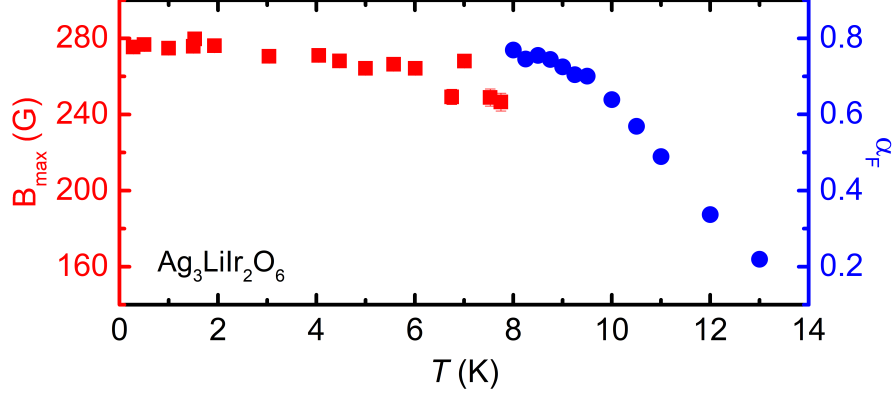
Figure 3.11: The blue circles represent α_F values from fits to Eq. 3.5, and the red squares represent B_{max} values from fits to Eq. 3.6 in the high-quality sample. Static magnetism starts at $T_N = 14$ K and μSR oscillations start at $T_{LRO} = 8$ K.

$T_N = 14$ K.

Region 3. At $T < T_{\mathrm{LRO}}$, clear oscillations appear in the depolarization curves for the high-quality $Ag_3LiIr_2O_6$ sample (Fig. 3.10), indicating a long-range magnetic order. The depolarization curves are well described by the function

$$A_{\mathrm{LRO}}(t) \ = A_0[\alpha_{\mathrm{LRO}} \exp(-\Lambda t) J_0(\gamma_\mu B_{\mathrm{max}} t + \phi) + (1 - \alpha_{\mathrm{LRO}}) \exp(-\lambda t)] \ (3.6)$$

Again, the initial asymmetry is $A_0 = 0.185$ in the Dolly spectrometer. Here J_0 is the zeroth-order Bessel function and the muon gyromagnetic ratio is $\gamma_\mu = 2\pi(135.5 \text{ MHz/T})$. The yellow line in Fig. 3.10 is a fit to the Bessel function at 0.28 K. A Bessel oscillatory behavior is typically associated with incommensurate magnetic ordering [98], where the muon experiences ordered fields ranging from 0 to B_{max}. We extract the B_{max} value from such a fit at each temperature below T_{LRO}, and plot it in Fig. 3.11 as red squares.

At the base temperature $T = 0.28$ K, the fit to Eq. 3.6 yields $\alpha_{\mathrm{LRO}} = 0.741(2)$, $B_{\mathrm{max}} = 269(1)$ G, $\phi = -0.9(6)°$, $\Lambda = 2.8(1)$ ¯s^{-1}, and $\lambda = 0.052(4)$ ¯s^{-1}. The value for α_{LRO} is close to the 2/3 value expected from a polycrystalline sample exhibiting long-range magnetic order. The damping rate λ is associated with those muons
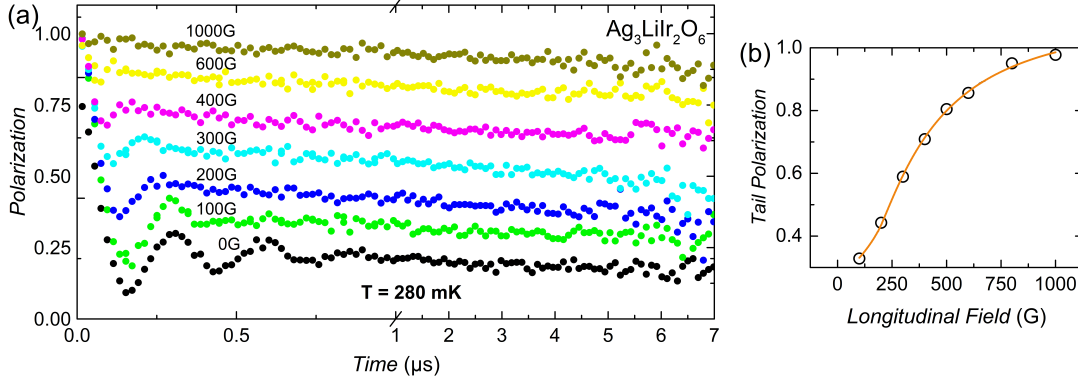
Figure 3.12: (a) Polarization scans in $Ag_3LiIr_2O_6$ at 0.28 K under different longitudinal fields (LF) from 0 to 1000 G. The time axis is expanded for $t < 1$ μs to reveal the oscillations. (b) By analyzing the recovery of the initial asymmetry with increasing field, we estimate $B_{int} = 263$ G in high-quality sample of $Ag_3LiIr_2O_6$. Solid lines are guides to the eye.

whose initial polarization lies along the local magnetic field and are depolarized by transverse magnetic fluctuations. The rate Λ contains contributions from both static magnetic disorder and magnetic fluctuations. Since $\Lambda \gg \lambda$, disorder is the dominant contribution.

The value for B_{max} is also confirmed from a LF experiment. As a consistency check, here we estimate the internal field B_{int} by analyzing the LF scans at 0.28 K as shown in Fig. 3.12(a). The initial polarization is fully recovered by 1000 G, so the internal field B_{int} must be much smaller than this value. A detailed analysis [99] shows that the midpoint of the polarization recovery occurs at a field value close to $B/B_{int} = 4/3$. Figure 3.12(b) shows that the midpoint of recovery in $Ag_3LiIr_2O_6$ is at 350 G, yielding an internal field $B_{int} = 263$ G, in good agreement with the $B_{max} = 269$ G obtained from our Bessel function fit to Eq. 3.6.[4]
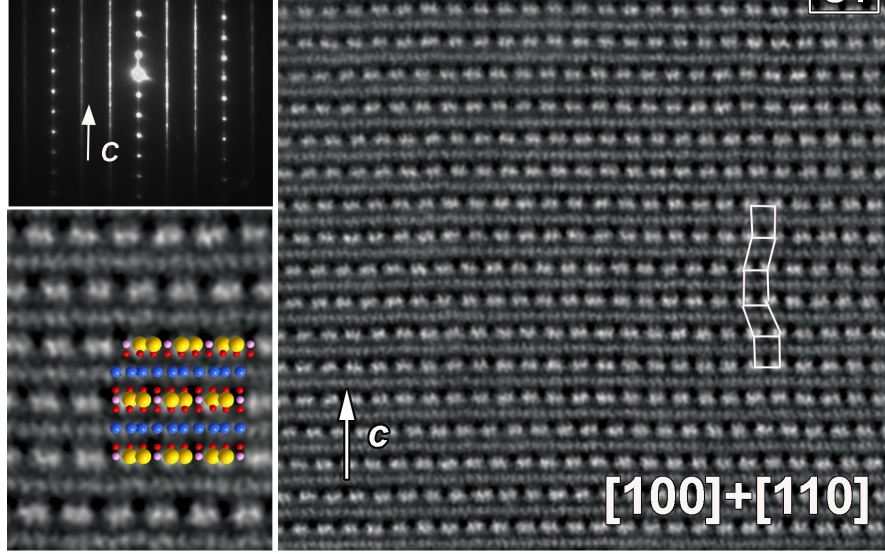
Figure 3.13: Electron diffraction (top inset) and HAADF-STEM image from the high-quality sample. A structural model is overlaid on the magnified image in the bottom inset with blue, yellow, pink, and red spheres for the Ag, Ir, Li, and O atoms, respectively.

3.4.5 Transmission Electron Microscopy

We characterize the structural properties of the $Ag_3LiIr_2O_6$ using high-resolution HAADF-STEM images in Fig. 3.13. The characteristic feature of each honeycomb layer in Fig. 3.13 is a repeating pattern of a pair of Ir atoms (large bright spots) separated by a Li atom (not visible). This pattern is clearly demonstrated for $Ag_3LiIr_2O_6$. In the inset of Fig. 3.13, a crystallographic model is overlaid on the magnified image to identify the Ag, Ir, Li, and O atoms as blue, yellow, pink, and red spheres, respectively (only the Ag and Ir atoms are clearly visible and light elements such as Li and O cannot be detected). The HAADF-STEM image from the high-quality sample in Fig. 3.13 shows pristine honeycomb layers free from silver inclusions. We present the electron diffraction (ED) patterns in the top inset of Fig. 3.13. The streaking in ED patterns is due to the stacking faults in the form of an angular twist between the adjacent layers as shown in other

---

[4]The μSR experiments and its analyses were performed by Dr. E. Kenney, Dr. C. Wang, Dr. A. Berlie, and Prof. M. Graf.
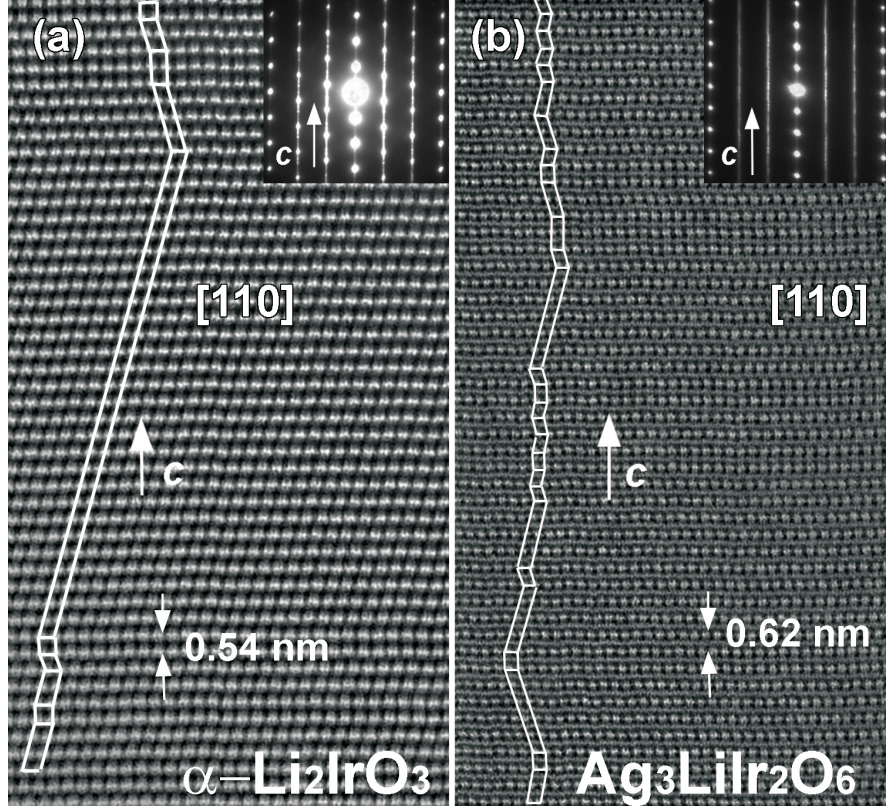
Figure 3.14: HAADF-STEM images from (a) α-Li$_2$IrO$_3$ and (b) Ag$_3$LiIr$_2$O$_6$. A high-quality sample is used for each material. The images show an abundance of stacking faults in Ag$_3$LiIr$_2$O$_6$ unlike α-Li$_2$IrO$_3$, due to the weaker inter-layer coupling in the former. The ED patterns are presented as insets and reveal less streaking in α-Li$_2$IrO$_3$ due to fewer stacking faults compared to Ag$_3$LiIr$_2$O$_6$.

honeycomb materials [63].

Here we point out that Ag$_3$LiIr$_2$O$_6$ suffers from the stacking faults, similar to other layered honeycomb materials such as Cu$_3$LiSn$_2$O$_6$ [63]. Figure 3.14 compares HAADF-STEM images between a high-quality sample of α-Li$_2$IrO$_3$ and a high-quality sample of Ag$_3$LiIr$_2$O$_6$. There is no intersite disorder in either image, but Ag$_3$LiIr$_2$O$_6$ exhibits many more stacking faults than its parent compound α-Li$_2$IrO$_3$. It has been demonstrated in a prior study of Cu$_3$LiSn$_2$O$_6$ that the stacking faults result from a twisting between the adjacent honeycomb layers, due to the weak O-Cu-O dumbbell bonds between the layers [63]. A similar mechanism is at work in Ag$_3$LiIr$_2$O$_6$, where the weak O-Ag-O dumbbell bonds lead to

the twisting between the layers and produce the zig-zag stacking pattern observed in Fig. 3.14(b). Despite the considerable amount of stacking faults in $Ag_3LiIr_2O_6$ (Fig. 3.14(b)), it still shows clear signatures of long-range order. In fact, the incommensurate order is similar between α-Li_2IrO_3 and $Ag_3LiIr_2O_6$ based on our μSR data and the published results in Ref. [50]. It is likely that in the absence of such stacking faults, the initial spin freezing at T_N could turn into a long-range order, i.e. $T_N =T_{LRO}$.

3.4.6 Density of States

The density of states (DOS) calculations for $Ag_3LiIr_2O_6$ are presented in Fig. 3.15, where a finite weight of Ag 4d orbitals are observed at the Fermi level E_F. We present three levels of the DFT calculations following the prior work on α-Li_2IrO_3 [100]. First, a plain LDA is presented in Fig. 3.15(a) to show the t_{2g} states just below E_F and e_g states above E_F. Notice that the majority of Ag electrons (blue line) are between 2 and 4 eV below E_F; however, a small but finite contribution from Ag d orbitals is observed near E_F. Second, by adding the SOC (LDA+SOC) in Fig. 3.15(b), the t_{2g} levels are split into lower $J_{eff} = 3/2$ and an upper $J_{eff} = 1/2$ states. Third, by adding an exchange potential (LDA+SOC+U) in Fig. 3.15(c), a gap is opened within the $J_{eff} = 1/2$ states to separate the upper and lower Hubbard bands. These results are identical to α-Li_2IrO_3 and consistent with the localized effective spin-1/2 Kitaev model [100]. The new finding is the finite weight of Ag 4d orbitals at E_F which remains unchanged between the LDA and LDA+SOC+U calculations, and suggests a d-p orbital mixing between the Ag and O atoms. Whereas the Li 2s electrons in α-Li_2IrO_3 are transferred to O 2p orbitals in an ionic bond, the Ag 4d electrons in $Ag_3LiIr_2O_6$ are more extended and bonded to the O 2p orbitals with a more covalent character. As a result of such d-p mixing, the SOC is effectively increased on the Ir-O-Ir exchange path
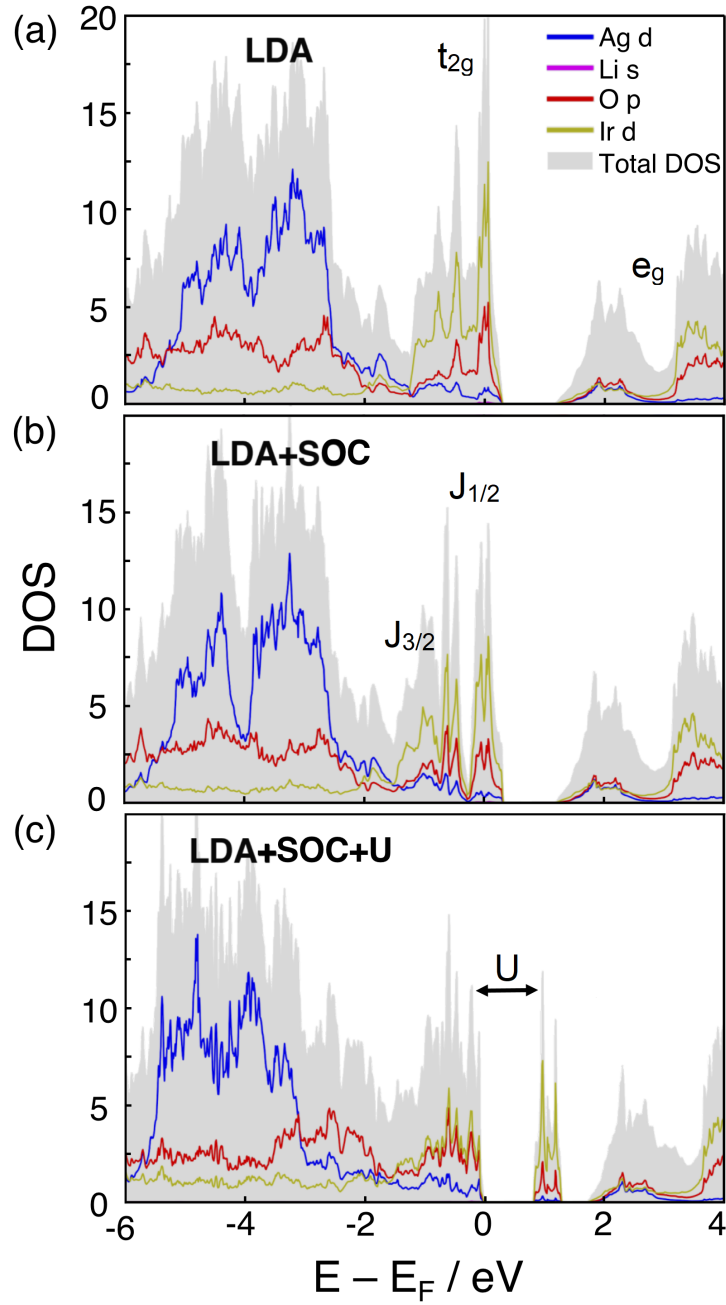
Figure 3.15: Density of states calculated at three levels of DFT with (a) local density approximation (LDA), (b) LDA+SOC, and (c) LDA+SOC+U where U is the exchange potential.

within the honeycomb layers of $Ag_3LiIr_2O_6$ which enhances the Kitaev coupling.[5]

3.5 Conclusion

In this work, I synthesized a novel Kitaev spin-liquid candidate via a topo-chemical method. The inter-layer bonds and atoms are modified in the parent compound α-Li_2IrO_3 to prepare the honeycomb-layered oxide, $Ag_3LiIr_2O_6$. The honeycomb structure remains the same in the Ag compound, while the inter-layer chemistry are completely modified. The octahedrally coordinated Li atoms are replaced by linearly coordinated Ag atoms; therefore, it leads to a weaker connection in $Ag_3LiIr_2O_6$. The weaker connection causes more stacking fault in the Ag-compound compared to the parent compound which is confirmed by the asymmetric peak in the region $19-22°$ and the HAADF-STEM images. The magnetic susceptibility in $Ag_3LiIr_2O_6$ shows a downturn at $T_N = 14$ K which is the onset of short-range magnetic ordering and a second sharper downturn, a signature of long-range magnetic ordering at $T_{LRO} = 8$ K. The heat capacity data also shows a broad peak at 14 K consistent with $\chi(T)$. The magnetic heat capacity shows a similar behavior as the parent compound, a two-peak structure. The low-temperature heat-capacity data (down to 52 mK) shows the same behavior as what is observed in α-Li_2IrO_3 and suggests a similar magnetic excitation in both compounds. In μSR, a fast decay of muon depolarization below T_N shows the onset of short-range order, and the appearance of oscillations below T_{LRO} confirms the long-range order in agreement with magnetic susceptibility data. The oscillation patterns in μSR data at low temperatures fit to a Bessel function, consistent with incommensurate ordering. An incommensurate spiral order has been confirmed in α-Li_2IrO_3 from both μSR and neutron scattering [50]. All these experimental results suggest $Ag_3LiIr_2O_6$ maintains all thermodynamic properties of α-Li_2IrO_3 in favor of

---

[5]The DOS calculations were done by Dr. W. Lafargue-Dit-Hauret and Dr. X. Rocquefelte.

Kitaev interactions with a lower long-range magnetic ordering temperature.[6]

CHAPTER IV

Effect of Structural Properties on Ir-Based Kitaev Magnets

4.1 Introduction

A long standing challenge in condensed matter physics has been to access a quantum spin liquid (QSL) ground state characterized by long-range entanglement and fractionalized anyonic excitations [1, 3, 4, 24, 101]. The Kitaev model, one of the most promising theoretical models of a QSL is heavily studied in quantum materials with main characteristic features such as a spin-1/2 configuration, bond-directional Ising interactions on a 2D honeycomb lattice with the potential to host a QSL phase as well as Majorana excitations [20]. The prime candidates for the Kitaev model are α-Li$_2$IrO$_3$, Na$_2$IrO$_3$, and α-RuCl$_3$, but all three compounds order magnetically at low temperatures and unfortunately fail to satisfy one of the main criterion for an ideal Kitaev material which is to remain magnetically disordered [21, 23, 35, 37, 38, 52, 84, 86].

Recently, a new class of intercalated Kitaev magnets have been synthesized via a topo-chemical exchange of the inter-layer Li/Na atoms in α-Li$_2$IrO$_3$ and Na$_2$IrO$_3$ with H, Cu, or Ag atoms, producing H$_3$LiIr$_2$O$_6$, Cu$_3$LiIr$_2$O$_6$, Cu$_2$IrO$_3$, and Ag$_3$LiIr$_2$O$_6$ [55, 59, 61, 70, 74, 90, 102, 103]. The motivation behind the

synthesis of intercalated Kitaev magnets is to structurally modify the original candidate material in favor of Kitaev interactions. It is claimed that this new family of Kitaev magnets, specifically $H_3LiIr_2O_6$ and $Ag_3LiIr_2O_6$, are closer to the QSL phase based on the absence of magnetic ordering in thermodynamic measurements, a scaling behavior in the heat capacity, and a two-step release of the magnetic entropy [1, 59, 74, 104]. Both bond disorder and modified inter-layer coordination are hypothesized as possible mechanisms for the proximity to the QSL ground state [1, 55, 59, 105]. It is worth mentioning that the modification of the prime candidate via a topo-chemical reaction will add more structural disorder such as stacking faults. Furthermore, if the quality of the honeycomb ordering in the parent compound used as a precursor is not well-defined, the structural modification can introduce rows of unwanted atoms in the honeycomb layers and break the honeycomb ordering pattern. Currently, there have been no careful experimental works to examine these hypotheses and elucidate the role of structural disorder in the intercalated Kitaev magnets. It is important to study the effect of structural disorder on the thermodynamic properties of intercalated Kitaev magnets and to avoid the misinterpretation of experimental results.

In this chapter, we present a careful study on the effect of structural disorder on one of the intercalated Kitaev magnets, $Ag_3LiIr_2O_6$. We show that the signatures of magnetic ordering may be hidden in a disordered sample, but they emerge unmistakably in a clean sample. Based on our experimental results, the onset of magnetic ordering in the clean limit is unaffected by the inter-layer coordination, and the nature of disorder in $Ag_3LiIr_2O_6$ is inconsistent with a randomized bond picture [1]. Our experimental discussion is organized in five sections. First, a comparison between the x-ray diffraction patterns of disordered and clean samples of α-Li_2IrO_3 and $Ag_3LiIr_2O_6$. Second, a comparison between the low temperature data of magnetic susceptibility of clean (S1) and disordered (S2) samples of

$Ag_3LiIr_2O_6$. In a clean sample (S1), we reveal a peak in the magnetic susceptibility at the Néel temperature $T_N = 14$ K followed by a sharper downturn at $T_{LRO}=8$ K, the onset of a long-range magnetic order, as discussed in chapter III. Such a peak is absent in a disordered sample (S2). Third, we also reveal a peak in the heat capacity of S1 at T_N, which turns into a mild change of slope in S2. Fourth, using muon spin relaxation (μSR) measurements, we show that the μSR oscillations are not visible in the disordered sample (S2) which can mistakenly be interpreted as evidence for a QSL phase, while as discussed in chapter III, T_N marks the onset of an incommensurate magnetic order with short-range correlations that becomes long-range below T_{LRO} in the clean sample S1. Fifth, we use transmission electron microscopy (TEM) to reveal extended regions of silver inclusion within the honeycomb layers of S2 that are absent in S1. After a complete comparison between the thermodynamic properties of clean and disordered samples of $Ag_3LiIr_2O_6$, in the second part of this chapter I will provide a comparison between the structural and thermodynamic properties of a clean sample of $Ag_3LiIr_2O_6$ and $H_3LiIr_2O_6$. The results of this chapter are published in Ref. [44, 64].

4.2 Methods

4.2.1 Material Synthesis

$Ag_3LiIr_2O_6$ was synthesized via a topo-tactic cation-exchange reaction as reported in Ref. [59, 70]. To prepare the samples in two different limits, it was important to prepare the parent compound, α-Li_2IrO_3 in two different honeycomb ordering qualities. A higher quality of the honeycomb ordering in α-Li_2IrO_3 increases the duration of the topo-chemical reaction and it requires keeping the mixture of α-Li_2IrO_3 and $AgNO_3$ under mild synthesis conditions for longer. The weaker honeycomb ordering in α-Li_2IrO_3 is one of the main reasons for breaking

the honeycomb networks and replacing them with rows of unwanted Ag atoms. We minimized the stacking faults in the precursor α-Li$_2$IrO$_3$ by performing a sequential solid-state synthesis at 900, 1000, and 1015 °C for 24, 32, and 48 h, respectively [34]. We increased the duration of the topo-tactic reaction to several days (up to 7 days) to ensure a complete exchange of the high-quality α-Li$_2$IrO$_3$ precursor. The sample S1 was prepared via a chemical substitution of very high-quality α-Li$_2$IrO$_3$ and sample S2 was made with a lower honeycomb ordering quality α-Li$_2$IrO$_3$ sample [59].

4.2.2 Characterization

Powder X-ray diffraction - The PXRD was performed using a Bruker D8 ECO instrument equipped with a Cu-K$_\alpha$ source and a 1D LINXEYE-XE detector. The quality of both the parent compound and the Ag-exchange material are confirmed via a careful evaluation of high-resolution x-ray diffraction data. After each step of reheating and annealing the precursor, α-Li$_2$IrO$_3$, the measured x-ray diffraction pattern was examined to decide upon the next synthesis condition.

Magnetism and Heat capacity - Magnetization and heat capacity were measured using a Quantum Design MPMS3 and Dynacool PPMS, respectively. Polycrystalline specimens of both disordered and clean limits of α-Li$_2$IrO$_3$ and Ag$_3$LiIr$_2$O$_6$ were used for measurements. For the magnetization measurements, about 30 mg of a polycrystalline sample were packed in a plastic capsule and mounted on a brass holder. For the heat capacity measurements, a powder sample was pressed into a pellet and cut into a rectangular shape with a mass of about 4.5 mg.

Transmission Electron Microscopy - The electron diffraction (ED) and high angle annular dark field scanning TEM (HAADF-STEM) were performed using an aberration corrected JEM ARM200F microscope.[1]

---

[1]The TEM measurements were done by Dr. O. Lebedev.

Muon Spin Relaxation - The μSR experiments were carried out at the Paul Scherrer Institute (PSI) using a ^{3}He refrigerator with the Dolly Multi Purpose Surface-Muon Instrument (sample S1), and a gas flow cryostat with the General Purpose Surface-Muon (GPS) Instrument (both samples). The Musrfit program [93] was used for data analysis. Sample S1 was pressed into a pellet 13 mm in diameter and 1 mm thick, and sample S2 was 13 mm in diameter and 1.2 mm thick. The pellets were wrapped in a 25 μm thin silver foil and mounted with varnish on copper holders. The same holder was used to mount S1 in both spectrometers. Initial measurements were made on sample S2 using a dilution refrigerator and gas flow cryostat on the EMU spectrometer at the ISIS Muon Source at the Rutherford Appleton Laboratory.[2]

4.3   Structural Quality

The important difference between the two $Ag_3LiIr_2O_6$ samples, S1 and S2, is in the α-Li_2IrO_3 precursor used in their synthesis. Figure 4.1(a) compares the x-ray patterns between two α-Li_2IrO_3 precursors, shown in black and red, used for the synthesis of samples S1 (clean) and S2 (disordered), respectively. The region between 19° to 24° gives information about the quality of honeycomb ordering in α-Li_2IrO_3 (Fig. 4.1a, left inset). The black x-ray pattern with sharp and well-separated peaks indicates better honeycomb ordering and fewer stacking faults than the red x-ray pattern. A similar level of disorder carries over to the $Ag_3LiIr_2O_6$ produced from these precursors. However, when the honeycomb ordering is not strong, the honeycomb networks can break during the chemical substitution of the parent compound and lead to rows of unwanted atoms. We also reveal the effect of disorder on the magnetic behavior of α-Li_2IrO_3 by plot-

---

[2]The μSR experiments and analysis have been done by Prof. M. Graf, Dr. E. Kenney, Dr. C. Wang, Dr. A. Berlie.
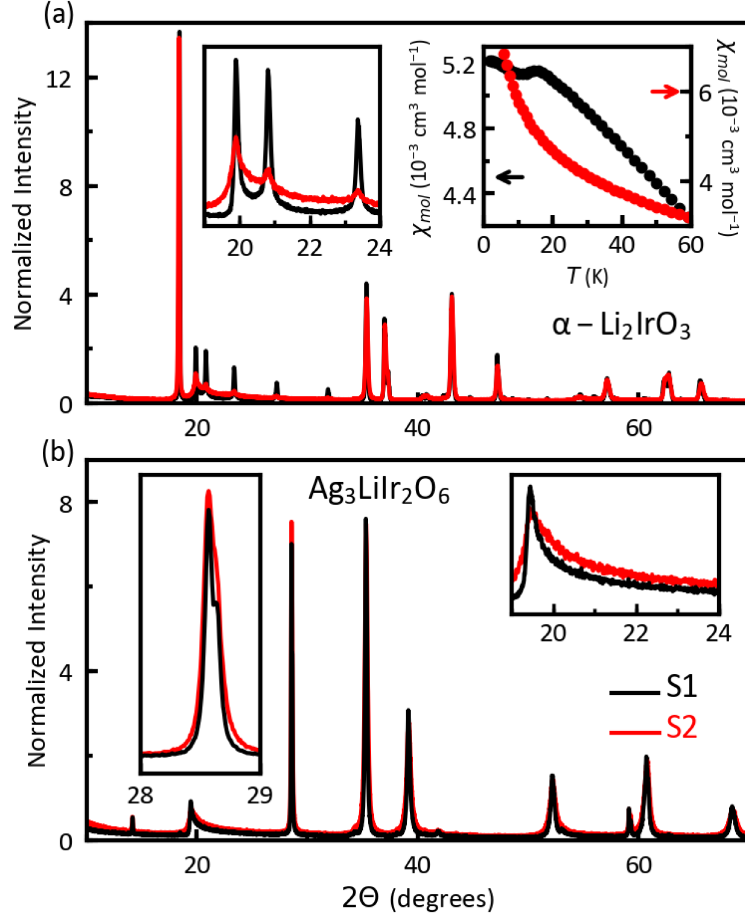
Figure 4.1: (a) X-ray patterns of two α-Li$_2$IrO$_3$ precursors used in the synthesis of clean (black) and disordered (red) Ag$_3$LiIr$_2$O$_6$. The region of honeycomb peaks is magnified in the left inset. Temperature dependence of the DC magnetic susceptibility in the two α-Li$_2$IrO$_3$ precursors is presented in the right inset. (b) X-ray patterns of two Ag$_3$LiIr$_2$O$_6$, S1 (black) and S2 (red). The peak at 28.5° in the two Ag$_3$LiIr$_2$O$_6$ samples is compared in the left inset. The region of honeycomb peaks is magnified in the right inset.

ting the DC susceptibility of both α-Li$_2$IrO$_3$ samples as a function of temperature below 60 K in the right inset of Fig. 4.1(a). The red curve does not show any signs of magnetic ordering and shows a long tail in the low temperature region, a sign of a higher level of stacking faults, while the black curve shows a peak at the AFM transition at 15 K, consistent with previous reports on α-Li$_2$IrO$_3$ [34–36, 52]. Based on the DC magnetic susceptibility of clean and disordered samples of α-Li$_2$IrO$_3$, it is clear that having a high level of stacking fault disorder in the parent compound conceals the signs of long-range AFM order; thus it is crucial to confirm the quality of the precursor via different thermodynamic measurements in addition to x-ray diffraction before the topo-tactic reaction.

Figure 4.1(b) shows the difference between the x-ray patterns of Ag$_3$LiIr$_2$O$_6$ samples S1 (black) and S2 (red). The main differences between the two samples are the intensity of the peak at 28.5° (left inset) and the sharpness in the asymmetric honeycomb peaks (right inset). S1 has sharper asymmetric honeycomb peaks and a shorter peak at 28.5°, which is similar to a prior report [70]. Whereas we have used AgNO$_3$ for the silver-exchange reaction, the authors of Ref. [70] used a mixture of AgNO$_3$/KNO$_3$ for the reaction. In S2, the honeycomb peaks are broader, and the intensity of the two peaks at 28.5° and 35.3° are nearly the same. Note the honeycomb ordering peaks in both S1 and S2 samples appear as an asymmetric broadening peak that confirms a higher level of stacking fault disorders in the Ag-exchange system compared even to the disordered samples of α-Li$_2$IrO$_3$.

4.4 Structural Disorder

Here we characterize the structural disorder in the Ag-exchange materials using high-resolution HAADF-STEM images from both samples S1 and S2 in Fig. 4.2. The images reveal extended regions of Ag inclusion within the honeycomb layers in S2, unlike S1 which is devoid of such inclusions. The characteristic feature of each

honeycomb layer in Fig. 4.2(a,b) is a repeating pattern of a pair of Ir atoms (large bright spots) separated by a Li atom (not visible). This pattern is interrupted in sample S2 by rows of unwanted Ag atoms (smaller bright spots) as indicated by the arrows of Ag atoms in Fig. 4.2(a). Note that Ag inclusions take the form of extended defects (rows of Ag atoms) instead of local defects (singular inter-site disorder). The distinction between local and extended defects are especially important in theoretical modeling of disordered Kitaev magnets [106, 107].

In the inset of Fig. 4.2(a), a crystallographic model is overlaid on the magnified image to identify the Ag, Ir, Li, and O atoms as blue, yellow, pink, and red spheres, respectively (only the Ag and Ir atoms are clearly visible). The arrows indicate where the unwanted Ag atoms (blue) are inserted within the Ir layer (yellow). In contrast, the HAADF-STEM image from the clean sample S1 in Fig. 4.2(b) shows pristine honeycomb layers free from Ag inclusions.

We present the ED patterns for S1 and S2 in the top insets of Fig. 4.2(a,b). The streaking in ED patterns is due to the stacking faults in the form of angular twist between the adjacent layers as shown in other honeycomb materials [63]. Upon careful inspection, the ED pattern of sample S1 reveals less streaking than S2. This is consistent with the synthesis of sample S1 from a precursor α-Li$_2$IrO$_3$ with fewer stacking faults as explained in 4.3 (Fig. 4.1).

4.5 Magnetization and Heat Capacity

A complete review on the thermodynamic properties of the clean sample of Ag$_3$LiIr$_2$O$_6$ (S1) is presented in chapter III. Here we focus on the main differences in magnetization and heat capacity data of clean (S1) and disordered samples (S2). Figure 4.3(a) shows a comparison in the C/T curves between samples S1 (clean) and S2 (disordered). Whereas S2 shows a slight change of slope at $T_N = 14$ K, S1 reveals a peak. Notice that without having the clean sample S1, the heat capacity
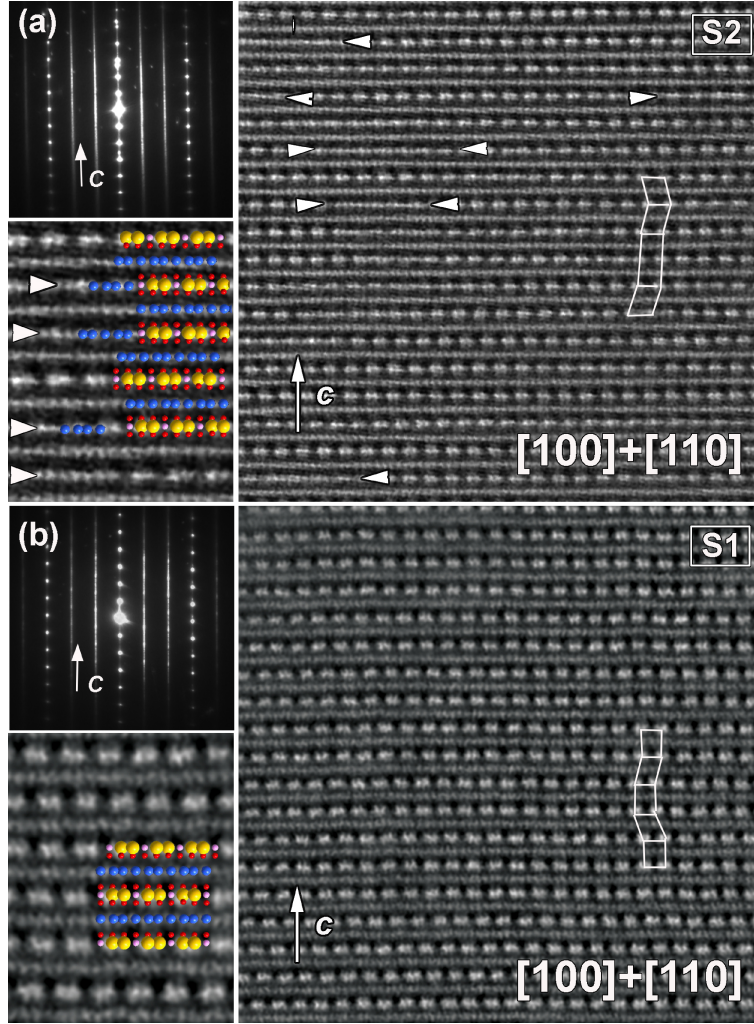
Figure 4.2: (a) Electron diffraction (top inset) and HAADF-STEM image from the disordered sample S2. A structural model is overlaid on the magnified image in the bottom inset with blue, yellow, pink, and red spheres for the Ag, Ir, Li, and O atoms, respectively. The arrows indicate where Ag atoms replace Ir atoms within the honeycomb layers. (b) Similar images from the clean sample S1 where Ag inclusion is absent.
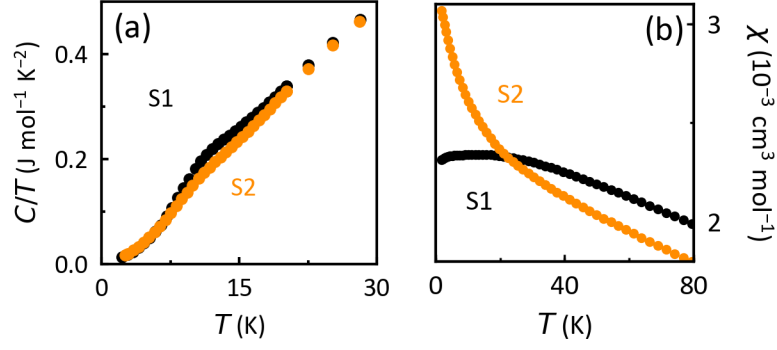
Figure 4.3: (a) Comparison between C/T as a function of temperature below 30 K in the clean sample S1 (black) and disordered sample S2 (orange). The orange curve is shifted by -0.014 K for clarity. (b) $\chi(T)$ curves are compared between the clean sample S1 (black points) and disordered sample S2 below 80 K.

of S2 could have been misinterpreted as the absence of magnetic ordering. This shows the importance of improving sample quality, since without having access to S1, we could not have associated the peak at T_L with the entropy release from a long-range AFM order instead of entanglement. However, a two-peak structure in the heat capacity data of a magnetically ordered Kitaev material is evidence of its proximity to the Kitaev limit as is theoretically predicted by a study on a generalized Kitaev-Heisenberg model [85], and our discussion does not discredit the iridates and α-RuCl$_3$ as Kitaev candidates [36, 96].

We next compare the magnetic susceptibility of the clean sample (S1) and disordered sample (S2) in Fig. 4.3(b). A susceptibility peak is present in the former, but absent in the latter. The absence of such a peak in a sample with the same quality as S2 has been misinterpreted as evidence of proximity to a Kitaev spin liquid [59]. After improving the sample quality of Ag$_3$LiIr$_2$O$_6$, we were able to observed the AFM peak in the high-quality sample S1. Based on our results, it would be insightful to revisit recent claims of a QSL phase in another Kitaev material H$_3$LiIr$_2$O$_6$, which suffers from a higher level of disorder than Ag$_3$LiIr$_2$O$_6$ [72, 74]. A large low-temperature tail in $\chi(T)$ has been observed in H$_3$LiIr$_2$O$_6$ similar to the behavior of sample S2 in Fig. 4.3(b). The question is

whether a peak is hidden under that low-temperature tail. In a similar vein, recent claims of a disordered QSL phase in Cu_2IrO_3 based on the absence of a peak in $\chi(T)$ may be questionable [105]. In fact, a small peak at 2 K has been reported in higher-quality samples of that material and diagnosed as a signature of partial static magnetism [108].

To understand the magnetic interactions in $Ag_3LiIr_2O_6$, we compared the results of a Curie-Weiss (CW) analysis of the inverse susceptibility ($1/\chi$) for both clean (S1) and disordered (S2) samples [44, 59]. The CW fit for the S1 sample yields a CW temperature $\Theta_{CW}=-132(1)$ K and a magnetic moment $\mu_{eff}=1.87(2)\,\mu_B$. The same analysis on the same temperature range was done for the S2 sample and yielded $\Theta_{CW}=-142$ K and $\mu_{eff}=1.79(2)\,\mu_B$. The negative sign of Θ_{CW} indicates AFM interactions, and its large magnitude compared to T_N implies magnetic frustration [109]. The values of μ_{eff} and Θ_{CW} are comparable between S1 and S2 [44, 59] and suggests a similar interaction strength in both samples.

4.6 Muon Spin Relaxation

In chapter III, the results of μSR measurements on the clean sample S1 is presented. The results for temperatures below 20 K are studied in detail for three different regions: 20 K$> T > T_N$ (depolarization is dominated by the nuclear moments), $T_N > T > T_{LRO}$ (depolarization is dominated by the electronic moments), and $T < T_{LRO}$ (clear oscillations indicative of a long-range magnetic order). Here, we only focus on the comparison between the μSR data of clean (S1) and disordered (S2) samples.

We compare the polarization (normalized asymmetry) at 10 K between samples S1 and S2 in Fig. 4.4(a). At this temperature ($T_N > T > T_{LRO}$) neither S1 nor S2 shows oscillations; however, the fast decay below 1 μs is visibly faster in S1. Note that the long-time tail of polarization converges to the same value in both
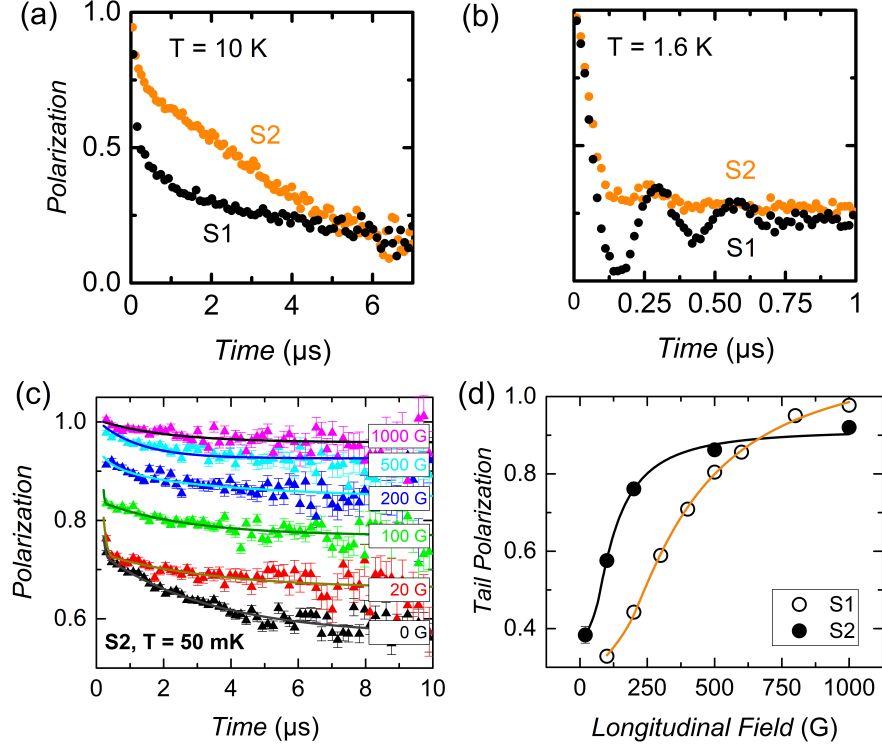
Figure 4.4: (a) Muon polarization ($P = A/A_0$ where A_0 is the initial asymmetry) as a function of time in S1 and S2 at 10 K ($T_N > T > T_{LRO}$). (b) Polarization curves below 1 μs in S1 and S2 at 1.6 K ($T < T_{LRO}$). The oscillations are barely discernible in the disordered sample S2, although the initial depolarization is comparable between S1 and S2. (c) Polarization scans in the disordered sample S2 at 0.05 K under LF from 0 to 1000 G. The data in panel (c) were collected at ISIS facility. (d) By analyzing the recovery of the initial asymmetry with increasing field, we estimate $B_{int} = 263$ G in S1 and 113 G in S2. Solid lines are guides to the eye.

samples, indicating weak dynamics. We conclude that the same magnetic ordering starts below T_N in both samples, but the short-range correlations are stronger in S1 as evidenced by the larger fast decay with a rate of λ_F (equation 3.5) than in S2.

Figure 4.4(b) compares the polarization curves as a function of time for both S1 and S2 samples at 1.6 K. The oscillations in sample S1 are clearly observed which are indicative of high-quality sample; however, sample S2 barely shows any sign of oscillations and without access to the results of sample S1 a careful μSR analysis was not possible. Two additional observations in Fig. 4.4(b) are worth noting. First, at extremely short timescales (less than 0.1 μs) the fast depolarization is identical in both samples. Second, the long-time depolarization tail ($t > 0.8$ μs) converges between the two samples. From these observations, we conclude that a similar incommensurate order exists in the ground state of both samples, but with a longer correlation length in sample S1 than in S2, due to less structural disorder.

The oscillations are barely visible in S2 at zero-field (ZF) μSR data, thus a fit to Eq. 3.6 would not work. To calculate the internal field for the S2 sample, we turned to the longitudinal field (LF) μSR data. Figure 4.4(c) shows the LF scans collected from the disordered sample S2 at 0.05 K. Figure 4.4(d) shows that the midpoint of recovery in S1 is at 350 G, yielding an internal field $B_{\text{int}} = 263$ G, in good agreement with the $B_{\text{max}} = 269$ G obtained from our Bessel function fit to Eq. 3.6, as discussed earlier. The midpoint of recovery in S2 occurs at 150 G in Fig. 4.4(d), yielding an internal field $B_{\text{int}} = 113$ G which is smaller than in sample S1. A smaller internal field may result from a range of muon stopping sites in the disordered sample. Since μSR is a local probe, we do not expect a major change in the local field near Ir^{4+} sites below T_N, but it is likely that muons probe a range of stopping sites with slightly different chemical environment due to various

levels of Ag inclusion across the sample. This explains the slow depolarization of muons inside S2 at 10 K in Fig. 4.4(a), and the different polarization recovery between S2 and S1 in Fig. 4.4(d). As noted earlier, it is not possible to fit the ZF data in sample S2 to a Bessel function (Eq. 3.6) because the oscillations are not discernible in the disordered sample. Thus, the LF analysis is the only way of estimating the local internal field in S2.

4.7 Comparison Between X-ray Diffraction of Exchanged Ir-Based Materials
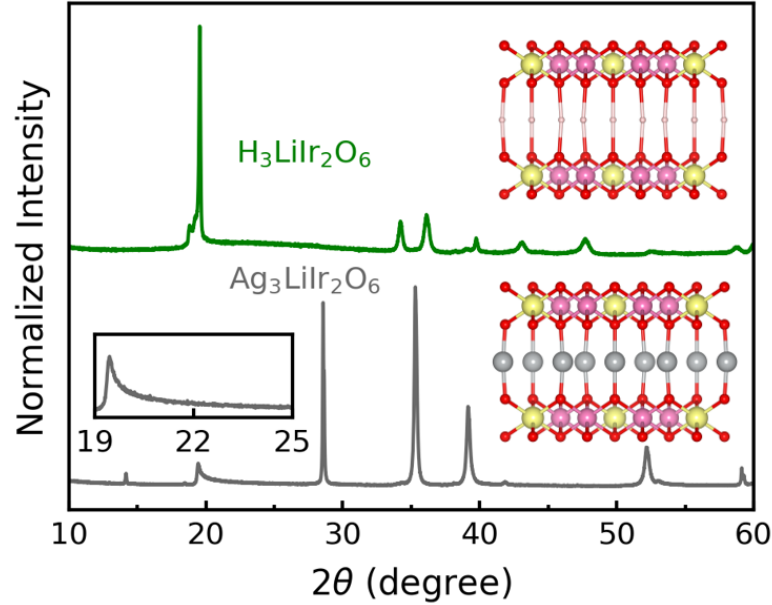
Figure 4.5: The x-ray patterns of two intercalated Kitaev systems, $H_3LiIr_2O_6$ (green) and $Ag_3LiIr_2O_6$ (gray data). The inset shows the asymmetric broadening of the honeycomb Bragg peaks in $Ag_3LiIr_2O_6$ due to stacking faults. In $H_3LiIr_2O_6$, the honeycomb peaks are hardly discernible due to high structural disorder.

The x-ray pattern of a high-quality α-Li_2IrO_3 sample is presented in Fig. 3.1. The sharp and well-separated Bragg peaks, specifically in the region between 20° to 30°, are signatures of a high-quality sample as was discussed earlier. The x-ray diffraction patterns of $Ag_3LiIr_2O_6$ (green) and $H_3LiIr_2O_6$ (gray) are presented in

Fig. 4.5. Both $Ag_3LiIr_2O_6$ and $H_3LiIr_2O_6$ are synthesized via a structural modification of the inter-layer atoms and the associated chemical bonds in the parent compound, α-Li_2IrO_3. The Li atoms are octahedrally coordinated with three O atoms from the top and three from the bottom honeycomb layers in α-Li_2IrO_3. These strong connections are replaced by linear and weaker connections in both $Ag_3LiIr_2O_6$ and $H_3LiIr_2O_6$, therefore the exchanged materials have more stacking faults than their parent compounds [44, 110]. The higher amount of stacking faults in the intercalated Kitaev magnets is due to the inter-layer chemistry. The weak linear bonds are responsible for more stacking faults in the exchanged materials. $Ag_3LiIr_2O_6$ and $H_3LiIr_2O_6$ suffers more from different structural disorders such as stacking faults, unwanted atoms, or even changes in the oxidation states of magnetic element compared to α-Li_2IrO_3 [44, 61, 63, 71, 110].

The inset of Figure 4.5 shows the honeycomb ordering peaks for $Ag_3LiIr_2O_6$. The honeycomb ordering peaks in $Ag_3LiIr_2O_6$ are all merged together and appear as an asymmetric, broadened peak. The asymmetric broadening of honeycomb peaks is known as the Warren line shape, which is a signature of stacking disorder [111] and a sign for considerable stacking faults. In $H_3LiIr_2O_6$, the small size of H atoms and their high mobility make the chemical bonds even weaker than in $Ag_3LiIr_2O_6$. As such, $H_3LiIr_2O_6$ has the highest degree of stacking faults among the intercalated Kitaev magnets [72, 74, 110]. This is why the honeycomb peaks of $H_3LiIr_2O_6$ are not resolved by x-rays (Fig. 4.5). Also, a study on the single crystal properties of $H_3LiIr_2O_6$ shows the possibility of change in the oxidation state of Ir atoms from 4+ to 3+ for which Ir is non-magnetic [71]. Unlike the solid state reactions, topo-tactic exchange cannot be repeated to improve the sample quality. Thus, getting rid of the stacking faults in these materials remains an open challenge.

4.8 Tuning Magnetic Interactions via Topo-Chemical Methods
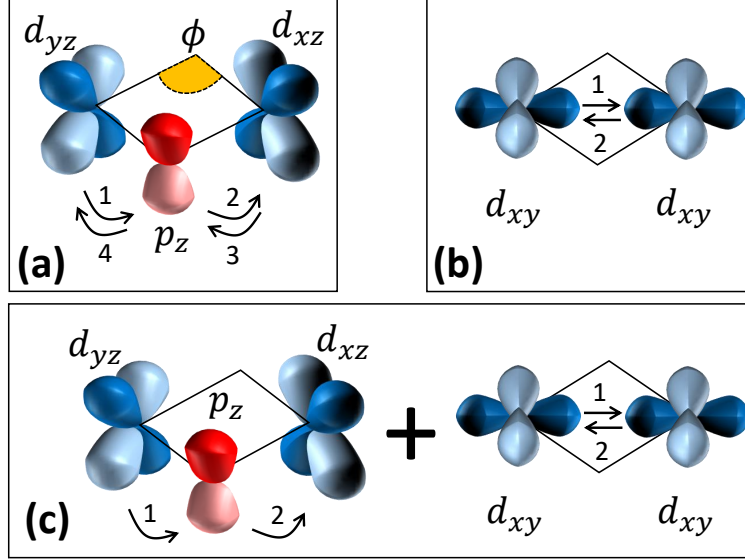
Figure 4.6: Exchange paths for (a) K, (b) J, and (c) Γ terms in Eq. 3.1. The d and p orbitals are painted in blue and red, respectively. The numbers show the hopping sequence in the perturbation.

As discussed in chapter III, the monoclinic unit cell and the honeycomb ordering in the 2D layers remain unchanged before and after exchange reactions. However, the change of inter-layer coordination from octahedral to dumbbell modifies the M-O-M (M = transition metal) bond angles within the honeycomb layers. Super-exchange magnetic interactions are sensitive to a change of bond angles and thus topo-chemical reactions can be used to tune the magnetic interactions. There are at least three terms in the magnetic Hamiltonian of the Kitaev materials, equation 3.1. The Kitaev term (K) favors QSL, the Heisenberg term (J) favors AFM ordering, and the off-diagonal exchange term (Γ) controls details of the ordered structure. All three terms can be modified via topo-chemical reactions.

Figure 4.6 shows the individual exchange paths for each term in Eq. 3.1. The Kitaev term is an indirect exchange interaction with hopping matrix elements t_{dpd}

between the d_{xz}, p_z, and d_{yz} orbitals (Fig. 4.6(a)) [112, 113]. In addition to the indirect exchange (K), Fig. 4.6(b) shows a direct exchange path for the Heisenberg interaction (J) with hopping matrix element t_{dd} between d_{xy} orbitals, leading to $J \sim t_{dd}^2/U$ in Eq. 3.1 [114]. Finally, a combination of direct and indirect paths in Fig. 4.6(c) leads to the symmetric off-diagonal exchange, $\Gamma \sim t_{dpd}t_{dd}J_H/U^2$, where J_H is the Hund's coupling between the e_g and t_{2g} orbitals [62, 115]. The hopping matrix elements (t_{dd} and t_{dpd}) are tuned by the M-O-M bond angle and the M-M distance which can be tuned by the exchange reaction. For example, (i) the change of O positions within the honeycomb layers due to the change of inter-layer coordination modifies the M-O-M bond angle (ϕ in Fig. 4.6(a)) and thereby tunes t_{dpd}; (ii) according to theoretical calculations [21], the Heisenberg interaction is canceled between the opposite paths if the bond angle ϕ is close to $90°$ (Fig. 4.6(a)); (iii) the hybridization between the Ag d-orbitals between the layers and O p-orbitals within the layers tunes the ratio of t_{dpd}/t_{dd}.

4.9 Magnetic Characterization of Intercalated Kitaev Materials

To demonstrate the effect of topo-chemical modifications on the magnetic interactions (Eq. 3.1 and Fig. 4.6), we compare the heat capacity and magnetic susceptibility of the first- and second-generation Kitaev magnets. Figure 4.7(a) compares the magnetic susceptibility curves in α-Li_2IrO_3, $Ag_3LiIr_2O_6$, and $H_3LiIr_2O_6$ as a function of temperature below 30 K. The suppression of magnetic ordering due to topo-chemical changes in the intercalated Kitaev magnets is observed in the magnetic susceptibility data. The magnetic susceptibility of α-Li_2IrO_3 (black curve) shows a clear anomaly at $T_N = 15$ K indicating the antiferromagnetic (AFM) order. The green curve representing $Ag_3LiIr_2O_6$ shows two downturns at 14 K and
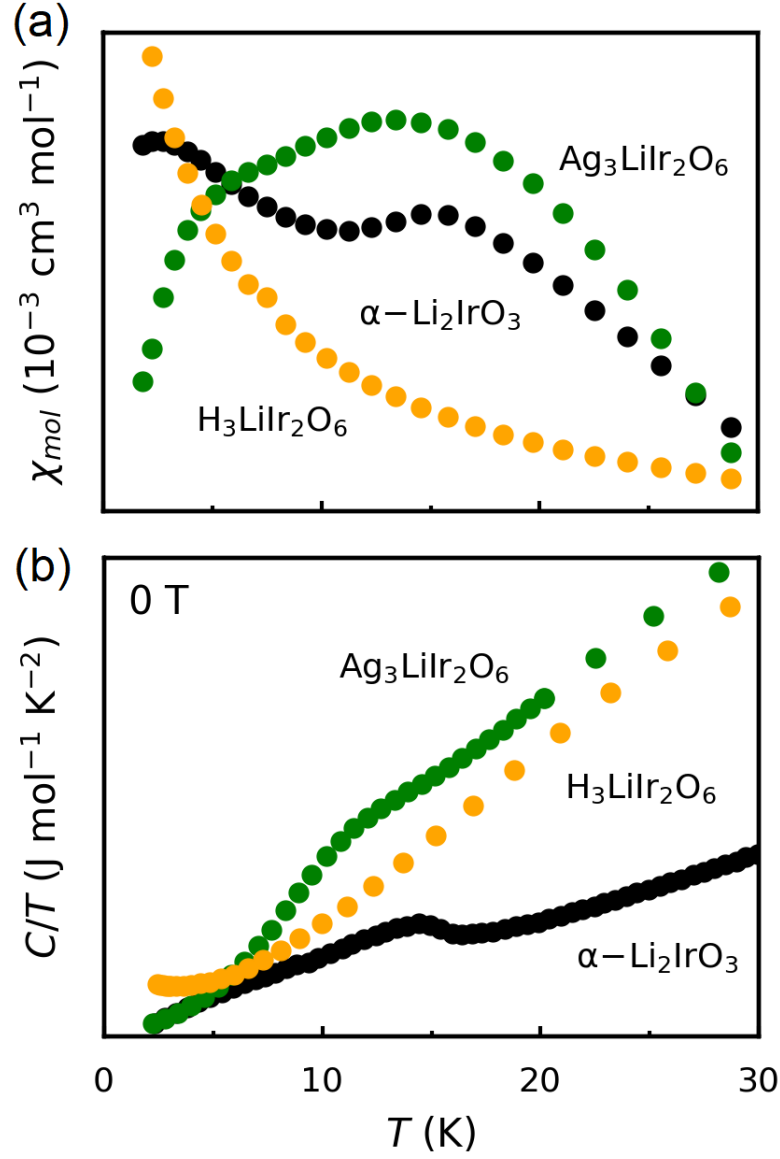
Figure 4.7: (a) Magnetic susceptibility (χ) plotted as a function of temperature below 30 K for the prime Kitaev magnet α-Li$_2$IrO$_3$ and its intercalated derivatives Ag$_3$LiIr$_2$O$_6$ and H$_3$LiIr$_2$O$_6$. (b) Heat capacity (C/T) plotted as a function of temperature below 30 K for the Kitaev magnet α-Li$_2$IrO$_3$ and its intercalated derivatives Ag$_3$LiIr$_2$O$_6$ and H$_3$LiIr$_2$O$_6$. The data for α-Li$_2$IrO$_3$ and Ag$_3$LiIr$_2$O$_6$ are reproduced from Refs. [35, 44].

8 K, corresponding to the onsets of short-range and long-range magnetic orders, respectively [44]. The orange curve representing $H_3LiIr_2O_6$ does not show any evidence of magnetic ordering consistent with previous reports on this material [72, 74].

Figure 4.7(b) compares the heat capacity curves in α-Li_2IrO_3, $Ag_3LiIr_2O_6$, and $H_3LiIr_2O_6$ as a function of temperature below 30 K. The peak in the heat capacity of α-Li_2IrO_3 confirms long-range magnetic ordering at $T_N = 15$ K, consistent with the χ data. The order has been characterized as incommensurate spiral by recent neutron scattering and muon spin relaxation (μSR) experiments [50, 51]. As seen in Fig. 4.7(b), this peak is shifted to lower temperatures in $Ag_3LiIr_2O_6$ and seemingly disappears in $H_3LiIr_2O_6$. The suppression of T_N in intercalated compounds $Ag_3LiIr_2O_6$ and $H_3LiIr_2O_6$ is a positive sign of approaching the QSL phase, where long-range order is replaced by long-range quantum entanglement [1, 23]. Our μSR experiment [44] has shown a similar incommensurate spiral order in $Ag_3LiIr_2O_6$; however, the long-range order develops at 8 K in $Ag_3LiIr_2O_6$, well below $T_N = 15$ K in α-Li_2IrO_3. Thus, the topochemical modification of bond angles seem to strengthen K and weaken J in Eq. 3.1. A recent nuclear magnetic resonance (NMR) experiment has shown absence of long-range order in $H_3LiIr_2O_6$, which is another promising result towards the discovery of a QSL phase [74].

4.10   Conclusion

By improving the sample quality, we have revealed signatures of a long-range incommensurate order in $Ag_3LiIr_2O_6$. A broad peak in the magnetic susceptibility and heat capacity at 14 K marks the onset of short-range magnetic ordering and a sharper downturn at 8 K indicates the onset of long-range magnetic ordering. Such a peak is absent in the disordered sample, which hinders the recognition of a long-range order in $Ag_3LiIr_2O_6$. In μSR, a similar pattern is observed, oscilla-

tions at base temperature are barely visible in the disordered sample while they are clearly observed in the clean limit. The oscillation patterns at low temperatures can be fitted to a Bessel function in the clean sample while such analysis is not possible for the disordered sample. Our HAADF-STEM images confirm a moderate level of extended defects (Ag inclusion) in the disordered $Ag_3LiIr_2O_6$ sample made from a lower quality α-Li_2IrO_3. In the disordered sample, the Ag atoms enter the honeycomb layer and disrupt the long-range magnetic order. This effect must be distinguished from the lack of magnetic ordering due to long-range entanglement in a QSL. Such a structural disorder can spuriously hide the long-range order and be misinterpreted as evidence of a QSL phase. As noted earlier, $H_3LiIr_2O_6$ is even more disordered compared to $Ag_3LiIr_2O_6$ due to the high mobility of the H atoms, which causes bond randomness and site vacancies within the honeycomb layers [72] and a lack of control over the number of intercalated H atoms between the honeycomb layers which can change the oxidation state of the Ir atoms. This discussion does not undervalue the importance of the role of topo-chemical reactions in the modification of magnetic interactions in a Kitaev magnet to enhance the Kitaev interactions in the prime Kitaev candidate. Here we aim at providing an experimental comparison between the thermodynamic behavior of the intercalated Kitaev magnets in different structural qualities to avoid any misinterpretation of experimental observation.[3]

CHAPTER V

First Demonstration of Tuning Between Kitaev and Ising Limits in a Honeycomb Lattice

5.1 Introduction

An exotic quantum state in condensed matter physics is the $J_{\text{eff}} = \frac{1}{2}$ state in honeycomb iridate materials that leads to the Kitaev exchange interaction [1, 20, 21, 23, 116, 117]. The $J_{\text{eff}} = \frac{1}{2}$ state is a product of strong spin-orbit coupling (SOC) effect in heavy Ir^{4+} ions that splits the t_{2g} manifold into a $J_{\text{eff}} = \frac{3}{2}$ quartet and a $J_{\text{eff}} = \frac{1}{2}$ doublet. With five electrons in the $5d^5$ configuration, the effect of crystal electric field (CEF) splits the five degenerate levels into the doubly degenerate e_g and triply degenerate t_{2g} orbital states and, further, the effect of strong SOC leads to the total effective angular momentum $J_{\text{eff}} = \frac{1}{2}$ and $J_{\text{eff}} = \frac{3}{2}$ states. Iridates have one electron (or equivalent to that one hole) in the spin-orbital $J_{\text{eff}} = \frac{1}{2}$ state that satisfies the prerequisites of the Kitaev interaction (spin-1/2 configuration) in a honeycomb lattice as shown by earlier studies [1, 21, 23, 116, 117].

In this chapter, we introduce a new spin-orbital state, $\mu = \frac{1}{2}$, which we have engineered by tuning the interplay between two energy scales: the SOC (λ_{SOC}) and the trigonal crystal field splitting (Δ_{T}). The $\mu = \frac{1}{2}$ state drives Ising instead

of Kitaev interactions. Although the Ising limit has been discussed in several theoretical studies [28, 49, 118, 119], a transition between the Kitaev and Ising limits has not been demonstrated until now. It has been theoretically predicted that the Kitaev limit in Na_2IrO_3 can be tuned to an Ising limit under uniaxial physical pressure [118], but the required pressure has not been achieved. The Ising limit is relevant to MPS_3 (M = Mn, Fe, Ni) compounds [119], however, a transition from the Ising to Kitaev limit has not been discussed in those materials, even at a theoretical level. This work presents the first experimental observation of a transition between the Kitaev and Ising limits in the same material family.

Our experiment was motivated by a survey of the average Curie-Weiss temperature (Θ_{CW}^{avg}) and the antiferromagnetic (AFM) or spin-glass transition temperatures (T_N/T_g) of the two-dimensional (2D) Ir, Rh, and Ru-based Kitaev materials (Fig. 5.1a and Table 5.1). These compounds can be categorized into two groups. The first-generation Kitaev magnets include α-Li_2IrO_3, Na_2IrO_3, Li_2RhO_3, and α-$RuCl_3$, synthesized by conventional solid-state methods. The first-generation candidates are prepared under high-temperature conditions via a direct synthesis method [34–38, 56, 57, 120–122]. The second-generation materials, such as $H_3LiIr_2O_6$, $Cu_3LiIr_2O_6$, $Cu_3NaIr_2O_6$, Cu_2IrO_3, and $Ag_3LiIr_2O_6$, have been recently synthesized by exchanging the inter-layer alkali (Li^+ and Na^+) in the first-generation compounds with H^+, Cu^+, and Ag^+ using topo-chemical reactions under mild conditions. The second-generation Kitaev candidates are metastable materials and they can only be synthesized via modification of the first-generation materials under low-temperature heating conditions [44, 55, 59–61, 64, 70, 74, 90, 108, 123–125]. Both the first and second-generation iridates appear in the same region of the phase diagram in Fig. 5.1a due to the overwhelming effect of SOC. The strong effect of SOC dominantly controls the magnetic and thermodynamic behavior in the iridate materials and prevents significant alterations in
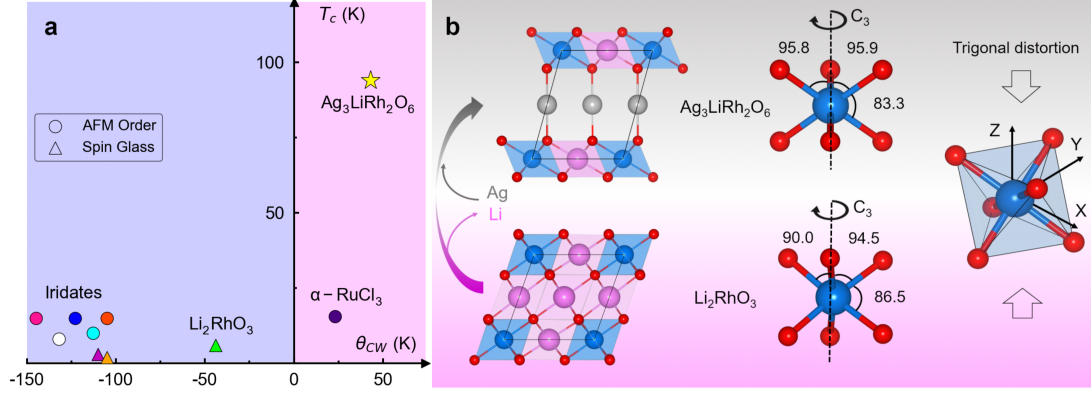
Figure 5.1: **Phase Diagram.** (a) Critical temperature (T_c) plotted against the Curie-Weiss temperature ($\Theta_{\mathrm{CW}}^{\mathrm{avg}}$) using the data in Table 5.1 for polycrystalline 2D Kitaev materials. Circles and triangles represent AFM and spin-glass transitions, respectively. The iridate materials are (from left to right) $Cu_3LiIr_2O_6$, $Ag_3LiIr_2O_6$, Na_2IrO_3, $Cu_3NaIr_2O_6$, Cu_2IrO_3, $H_3LiIr_2O_6$, and α-Li_2IrO_3. (b) Structural relationship between the first and second-generation Kitaev systems, Li_2RhO_3 and $Ag_3LiRh_2O_6$, with enhanced trigonal distortion in the latter, as evidenced by the change of bond angles after cation exchange.

both Curie-Weiss and transition temperatures via structural modification. The $4d$ systems, namely Li_2RhO_3 and α-$RuCl_3$, appear to be shifted horizontally but not vertically from the iridate block. The $4d$ transition-metals (Ru/Rh) are lighter elements compared to Ir; therefore, a decrease in the SOC effect leads to a change in the value of the CW temperature. Despite theoretical predictions of diverse magnetic phases for the Kitaev materials [62, 115], it seems all 2D Kitaev materials studied so far aggregate in the same region of the phase diagram with $T_{\mathrm{N}} \leq 15$ K and a $J_{\mathrm{eff}} = \frac{1}{2}$ state. This observation prompted us to experimentally investigate the possibility of tuning the local spin-orbital state and the magnetic ground state in the same material family.

We focused on rhodate ($4d$) systems where the SOC is weaker than in the iridate ($5d$) systems, and Δ_{T} has a better chance to compete with λ_{SOC}. Evidence of such competition can be found in earlier DFT studies of the honeycomb rhodates, where a high sensitivity of the magnetic ground state to structural parameters has been reported [56, 126]. To enhance Δ_{T}, we replaced the Li atoms between

Table 5.1: The effective moment μ_{eff}, average Curie-Weiss temperature Θ_{CW}^{avg}, and critical temperature T_c, listed from polycrystalline specimens of Kitaev magnets.

	Material	μ_{eff} (μ_B)	Θ_{CW}^{avg} (K)	T_c (K)	Ref.
First Gen.	Li_2RuO_3	2.2	-44	$T_g = 6$	[40, 41, 56, 57]
	$\alpha\text{-}Li_2IrO_3$	1.8	-105	$T_N = 15$	[34, 36]
	Na_2IrO_3	1.9	-123	$T_N = 15$	[35, 55]
	$\alpha\text{-}RuCl_3$	2.2	$+23$	$T_N = 15.6$	[120]
Second Gen.	Cu_2IrO_3	1.9	-110	$T_g = 3$	[55, 108]
	$Ag_3LiIr_2O_6$	1.9	-132	$T_N = 8$	[44]
	$Cu_3LiIr_2O_6$	2.1	-145	$T_N = 15$	[90]
	$Cu_3NaIr_2O_6$	2.0	-113	$T_N = 10$	[90]
	$H_3LiIr_2O_6$	1.6	-105	____	[74]
	$Ag_3LiRh_2O_6$	1.8	$+43$	$T_N = 94$	this work

the layers of Li_2RhO_3 with Ag atoms, and synthesized $Ag_3LiRh_2O_6$ topochemically (Fig. 5.1b). The change of inter-layer bonds leads to a trigonal compression along the local C_3 axis (Fig. 5.1b). Using crystallographic refinement (Fig. 5.2, Tables 5.2, and 5.3), we determined the bond angles within the local octahedral (O_h) environments of both compounds and quantified the trigonal distortion by calculating the bond angle variance [49] $\sigma = \sqrt{\sum_{i=1}^{12}(\theta_i - \theta_0)^2/(m-1)}$, where m is the number of the angles in an octahedron ($m = 12$) and $\theta_0 = 90°$ for an undistorted octahedron. In an ideal octahedron, $\sigma = 0$. In $Ag_3LiRh_2O_6$, we found $\sigma = 6.1(1)°$, nearly twice the $\sigma = 3.1(1)°$ in Li_2RhO_3. It has been noted in earlier theoretical works [28, 118] that a trigonal distortion can reconstruct the spin-orbital states and lead to new magnetic regimes; however, it has also been noted that such a regime may not be accessible in iridate materials due to the overwhelmingly strong SOC. As shown in Fig. 5.1a, we induced such a change of regime between Li_2RhO_3 and $Ag_3LiRh_2O_6$ using chemical pressure. The results of this chapter are published in Ref. [33].

Table 5.2: Unit cell dimensions and refinement parameters are listed for both Li_2RhO_3 and $Ag_3LiRh_2O_6$ from Rietveld refinements in the space group $C2/m$ (Fig. 5.2).

Material	Li_2RhO_3	$Ag_3LiRh_2O_6$
Mass (gr/mol)	164.787	632.364
a (Å)	5.11081(5)	5.23163(9)
b (Å)	8.83505(8)	9.05596(15)
c (Å)	5.09945(6)	6.46649(8)
β (°)	109.61155(88)	74.6384(18)
V (Å^3)	216.904	295.420
Z	4	2
D (gr/cm^3)	5.046	7.101
R_{p}	8.67	6.98
R_{exp}	5.93	6.00
χ^2	4.24	2.95

5.2 Methods

5.2.1 Material Synthesis

Similar to other second-generation Kitaev magnets, $Ag_3LiRh_2O_6$ is a metastable compound. It is synthesized through a topotactic cation-exchange reaction under mild conditions from the first-generation parent compound, Li_2RhO_3.

$$2Li_2RhO_3 + 3AgNO_3 \longrightarrow Ag_3LiRh_2O_6 + 3LiNO_3 \tag{5.1}$$

Li_2RhO_3 was synthesized following prior published works [70]. To perform the topotactic exchange reaction, Li_2RhO_3 and $AgNO_3$ powders were mixed very well, pressed into a pellet, and heated to 350 °C for 1 week. To avoid decomposition of $AgNO_3$ during the heating process, the material is sealed under Ar gas. After reaction, the excess $AgNO_3$ and produced $LiNO_3$ were removed via washing with deionized water.
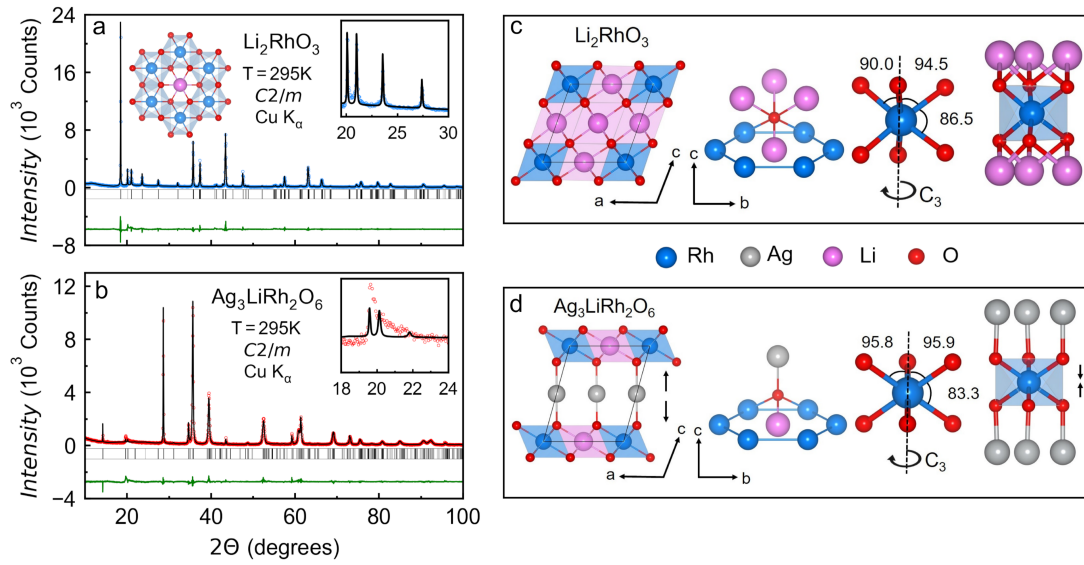
Figure 5.2: **X-ray data.** (**a**) Rietveld refinement (black line) on the powder x-ray pattern (blue data) of Li_2RhO_3. The expected reflections are indexed with black tics and the green line is the fit residual. The Bragg peaks in the inset are due to honeycomb ordering. (**b**) Rietveld analysis for $Ag_3LiRh_2O_6$ (red data). A larger amount of stacking faults in $Ag_3LiRh_2O_6$ leads to an asymmetric broadening of the honeycomb peaks (Warren line shape) commonly observed in delafossite structures ([63, 127]). (**c**) The inter-layer bonding, oxygen coordination, trigonal distortion, and RhO_6 octahedra in Li_2RhO_3. (**d**) The larger inter-layer spacing and larger trigonal distortion (compression along the local C_3 axis) in $Ag_3LiRh_2O_6$.

Table 5.3: Wyckoff sites, atomic coordinates, and site occupancies are listed for both Li_2RhO_3 and $Ag_3LiRh_2O_6$. The isotropic Debye-Waller factors (B_{iso}) are less than 1.0 Å^2 for all atoms. Since O and Li atoms are practically invisible to x-rays, the O and Li positions are modeled based on the honeycomb structures of α-Li_2IrO_3 and $Ag_3LiIr_2O_6$ ([57, 59]). An artificial mixing between the Rh and Li atoms is introduced in sites $4g$ and $2a$ to account for the stacking faults similar to the published refinement for Li_2RhO_3 ([57]).

Li_2RhO_3					
Atom	site	x	y	z	occupancy
O1	$8j$	0.245	0.321	0.759	1.000
O2	$4i$	0.255	0	0.773	1.000
Rh1	$4g$	0	0.33253(1)	0	0.870(1)
Li1	$4g$	0	0.33253(1)	0	0.130(1)
Rh2	$2a$	0	0	0	0.259(2)
Li2	$2a$	0	0	0	0.741(2)
Li3	$4h$	0	0.819(1)	1/2	1.000
Li4	$2d$	0	1/2	1/2	1.000
O-Rh-O angles	90.06(3)	94.53(3)	86.46(6)		
Rh-O lengths	1.9934(10)	2.0307(10)			
$Ag_3LiRh_2O_6$					
Atom	site	x	y	z	occupancy
O1	$8j$	0.3880	0.3314	0.8324	1.000
O2	$4i$	0.1090	1/2	0.1670	1.000
Li1	$4g$	0	0.66734(32)	0	0.234(1)
Rh1	$4g$	0	0.66734(32)	0	0.770(2)
Li2	$2a$	0	0	0	0.484(2)
Rh2	$2a$	0	0	0	0.524(2)
Ag1	$4h$	1/2	0.32325(28)	1/2	1.000
Ag2	$2d$	0	1/2	1/2	1.000
O-Rh-O angles	95.77(9)	95.88(9)	83.33(14)		
Rh-O lengths	2.021(3)	2.03266(6)	2.025(3)		

5.2.2 Crystal Structure

Powder x-ray diffraction (PXRD) was performed using a Bruker D8 ECO instrument in the Bragg-Brentano geometry, using a copper source (Cu-K$_\alpha$) and a LYNXEYE XE 1D energy dispersive detector. The FullProf suite was used for the Rietveld analysis [76] to create a CIF which was then visualized by VESTA [81]. Peak shapes were modeled with the Thompson-Cox-Hastings pseudo-Voigt profile convoluted with axial divergence asymmetry.

Topo-chemical reactions are excellent tools to induce local distortions in a crystal structure without changing its global symmetries. Any small modification in the structure of the first-generation compound leads to changes in the positions of other atoms in the material and slightly modifies their orientation in the unit cell. For example, the PXRD patterns of both Li_2RhO_3 and $Ag_3LiRh_2O_6$ in Fig. 5.2a,b fit to a layered structural model in the space group $C2/m$. The satellite Bragg peaks in the insets of Fig. 5.2a,b correspond to a honeycomb ordering of the Rh and Li atoms within each layer. The honeycomb ordering and stacking of the honeycomb layers are well-defined in Li_2RhO_3 as the Bragg peaks in the 20° to 30° range are observed to be sharp and well-separated, see the inset of Fig. 5.2a. Meanwhile, the honeycomb peaks in $Ag_3LiRh_2O_6$ are merged together and have an asymmetric broadening shape due to an increase in the level of stacking faults in the compound, see the inset of Fig. 5.2b. Despite having the same space group and honeycomb ordering, Li_2RhO_3 and $Ag_3LiRh_2O_6$ have different local symmetries that profoundly impact their magnetic behaviors. Specifically, Fig. 5.2c,d show different inter-layer bonding, with LiO_6 octahedra and AgO_2 dumbbells connecting the honeycomb layers in Li_2RhO_3 and $Ag_3LiRh_2O_6$, respectively. A weaker connection between the honeycomb layers in $Ag_3LiRh_2O_6$ pushes the O atoms towards honeycomb layers and distorts the octahedral environment around the magnetic atoms in the honeycomb layers. The local environment of cations

around each O is also changed from pseudo-octahedral in Li_2RhO_3 to pseudo-tetrahedral in $Ag_3LiRh_2O_6$. These changes enhance the trigonal distortion of the octahedral environment within the honeycomb layers of $Ag_3LiRh_2O_6$ compared to Li_2RhO_3. The O-Rh-O bond angles in Fig. 5.2c,d and the arrows in Fig. 5.2d indicate the trigonal compression along the local C_3 axis. A bond valence sum analysis (BVS= $\sum_i (\ell_0 - \ell_i)/b_0$) yields the oxidation state of +3.8 for Rh in $Ag_3LiRh_2O_6$, which is not far from the expected +4 value. The bond valence parameter ℓ_0 is available only for $b = 0.422$ according to the bvparm2020 database. There have been no recent efforts to correct ℓ_0 for $b = 0.37$ which is the current standard.

5.2.3 Magnetization, Heat Capacity, and Resistivity

Magnetization was measured using a Quantum Design MPMS3 with the powder sample packed into a plastic capsule mounted on a low-background brass holder. The measurements for both Li_2RhO_3 and $Ag_3LiRh_2O_6$ are performed under the same condition, DC measurements with continuous measurement mode.

Both the electrical resistivity (four-probe technique) and heat capacity (relaxation-time method) were measured on a pressed pellet using a Quantum Design PPMS Dynacool. Given that both Li_2RhO_3 and $Ag_3LiRh_2O_6$ have Rh^{4+} ions in the $4d^5$ configuration, with a single hole in the t_{2g} level, it is reasonable to assume a Mott insulating ground state. Figure 5.3 shows an insulating (activated) behavior in the resistivity of both compounds consistent with this picture. By fitting the data to an Arrhenius model, $\rho \propto \exp(\Delta/T)$, we extract the gap values of approximately 145 meV and 52 meV in Li_2RhO_3 and $Ag_3LiRh_2O_6$, respectively (Fig. 5.3a). However, as shown in Fig. 5.3b, these data are better described by a Mott variable range hopping (VRH) model, $\rho \propto \exp[(D/T)^{\frac{1}{4}}]$, which has been used for Na_2IrO_3 and Cu_2IrO_3 as well [37, 55, 128]. The Mott VRH can describe strongly disordered systems with localized charge-carrier states better.
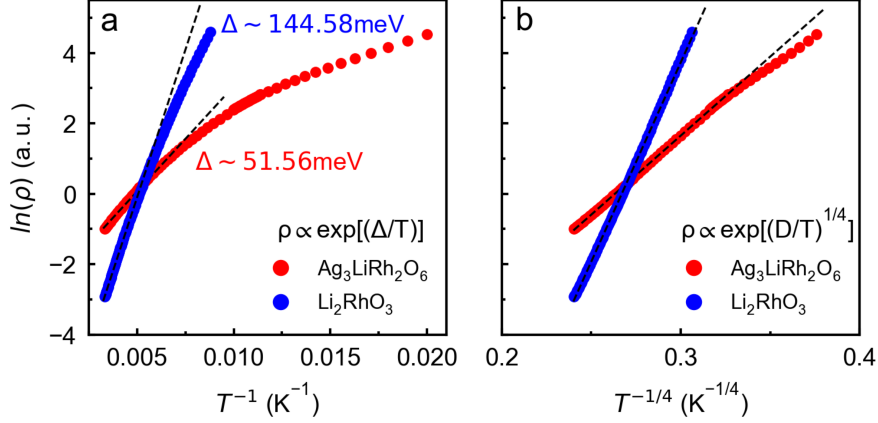
Figure 5.3: **Resistivity curves.** (**a**) Arrhenius fit of the resistivity data as a function of temperature in both Li_2RhO_3 and $Ag_3LiRh_2O_6$. (**b**) Mott variable range hopping fit of the resistivity data as a function of temperature.

5.2.4 Transmission Electron Microscopy

Electron diffraction (ED), high-angle annular dark-field scanning TEM (HAADF-STEM), and annular bright-field scanning TEM (ABF-STEM) were performed using an aberration double-corrected JEM ARM200F microscope operated at 200 kV and equipped with a CENTURIO EDX detector, Orius Gatan CCD camera and GIF Quantum spectrometer [63, 129][1].

Layered delafossite-type structures are prone to disorder, which can alter their magnetic properties [44, 64]. We used high-resolution STEM imaging to investigate the disorder at an atomic level. In Li_2RhO_3, the dominant form of disorder is a mild concentration of interstitial Rh atoms between the honeycomb layers (blue circles in Fig. 5.4a). Prior to this study, it had been assumed that disorder in Li_2RhO_3 is in the form of Li-Rh anti-site mixing within the honeycomb layers due to the similar ionic radii of Li^{1+} and Rh^{4+} ions [40, 41, 56, 126]. Although this idea is sensible based on the comparable size of Li and Rh atoms, our HAADF-STEM and ABF-STEM images in Fig. 5.4a rule out such anti-site disorder. In HAADF-STEM, the image contrast is proportional to the thickness

---

[1]The TEM measurements were performed by Dr. Oleg I. Lebedev at Laboratoire CRISMAT.
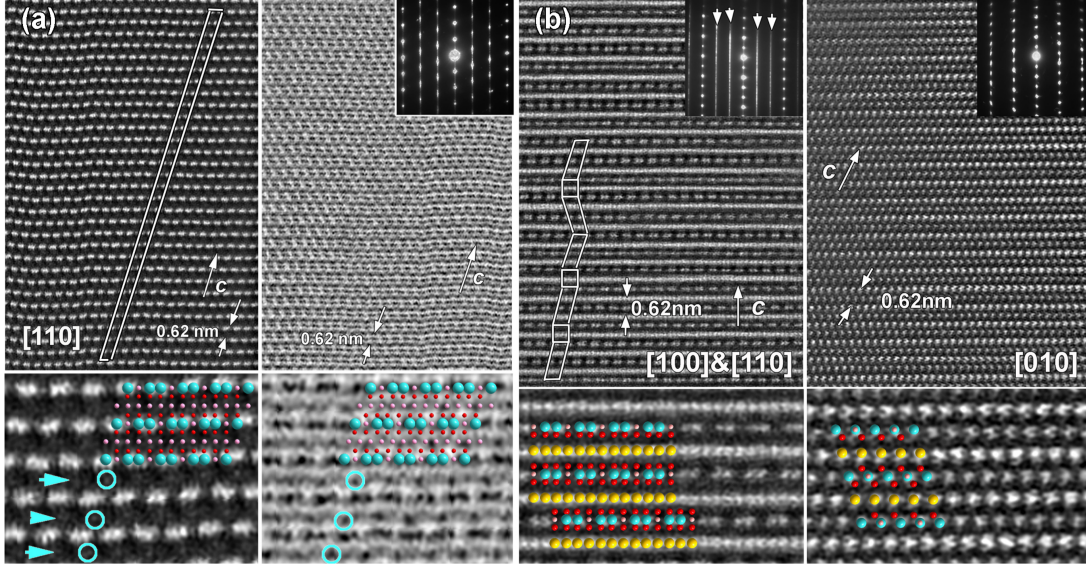
Figure 5.4: **Transmission electron microscopy.** (a) HAADF-STEM (left) and ABF-STEM (right) images of Li_2RhO_3, showing interstitial Rh atoms between the layers (blue circles). The nearly perfect stacking of honeycomb layers is most likely due to their pinning by interstitial Rh atoms. The honeycomb layers are characterized by a repeating pattern of pairs of Rh atoms (large spots) separated by a single Li atom (invisible due to small electron density) [63, 108]. (b) HAADF-STEM images of $Ag_3LiRh_2O_6$ viewing the crystals from [100] (left) and [010] (right) directions. The white zig-zag pattern highlights stacking faults due to a rotation of adjacent layers between the [100] and [110] directions. A crystallographic model (from PXRD) is overlaid on the TEM images of both Li_2RhO_3 and $Ag_3LiRh_2O_6$ with the Ag, Rh, Li, and O atoms appearing as yellow, cyan, pink, and red spheres.

of the crystal and the square of the atomic number (Z^2) [129], which makes Li ($Z = 3$) and Rh ($Z = 45$) atoms easily distinguishable as dark and bright spots, respectively. The presence of honeycomb ordering leads to a distinct pattern of pairs of Rh (bright spots) separated by a Li (dark spot) [63]. Nowhere in Fig. 5.4a do we see a breaking of this pattern. As such, Fig. 5.4a unambiguously confirms the absence of anti-site disorder within the honeycomb layers and identifies the interstitial Rh atoms between the honeycomb layers as the main form of disorder in Li_2RhO_3. Figure 5.4b is a HAADF-STEM image of the $Ag_3LiRh_2O_6$ lattice, where disorder is predominantly in the form of stacking faults. In a prior structural analysis of $Cu_3LiSn_2O_6$ and $Cu_3NaSn_2O_6$, which are isostructural to $Ag_3LiRh_2O_6$,

we have modeled the stacking faults as a twisting between adjacent layers [63]. Such twisting between the honeycomb layers and the resulting stacking faults are much less common in Li_2RhO_3 compared to $Ag_3LiRh_2O_6$ (Fig. 5.4a,b) due to two reasons: (i) the LiO_6 octahedra in Li_2RhO_3 offer stronger inter-layer bonding than the AgO_2 dumbbells in $Ag_3LiRh_2O_6$ (Fig. 5.2c,d), and (ii) the interstitial Rh atoms in Li_2RhO_3 prevent twisting between the layers by pinning them, leading to a nearly perfect monoclinic stacking as highlighted in Fig. 5.4a. The absence of a Warren line shape in the PXRD of Li_2RhO_3 (inset of Fig. 5.2a) is a manifestation of such perfect stacking.

5.2.5 Muon Spin Relaxation

The muon spin relaxation (μSR) measurements were performed in a continuous flow ^{4}He evaporation cryostat ($T > 1.5$ K) at the General Purpose Surface-Muon Instrument (GPS) [130] at the Paul Scherrer Institute (PSI), and the data was analyzed using the Musrfit program [93].[2]

A pressed disk of $Ag_3LiRh_2O_6$ with diameter 12 mm and thickness 1.2 mm was wrapped in 25 μm thick silver foil and suspended in the muon beam to minimize the contribution from muons implanted in the sample holder or in the cryostat walls, Fig 5.5. The μSR measurement is a local probe that can provide information about the magnetism in a material. The muon has a spin that can interact with the local magnetic field in a material. Above the transition temperature, the spins in a material have random direction and the internal magnetic field is zero; therefore, there is no change in a muon's spin orientation after their interactions with the material in a paramagnetic region. Below the transition temperature, the spins have a specific orientation based on the type of order and create an internal magnetic field which causes the muon's spin to rotate via interaction with the

---

[2]The μSR measurements were performed by Prof. M. Graf, Dr. C. Wang, Dr. H. Luetkens at the Paul Scherrer Institute.

internal field. The changes in the direction of the muon's spin can be presented in the form of asymmetry as a function of time, which below a long-range transition temperature will show clear oscillations.
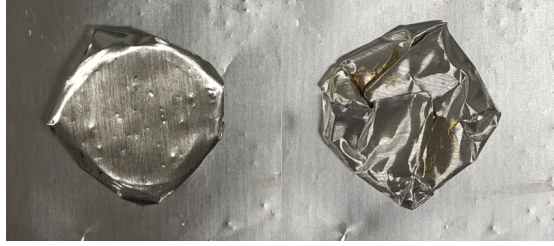
Figure 5.5: A pressed disk of $Ag_3LiRh_2O_6$ with diameter 12 mm and thickness 1.2 mm was wrapped in 25 μm silver foil. The left side image is where muons will enter the sample (this side will be glued to the copper sheet).

5.2.6 First Principles Calculations

The electronic structures were computed using the open-source code QUANTUM ESPRESSO [131, 132] with the experimental crystallographic information file (CIF) as the input. The calculation included SOC and zigzag magnetic ordering for both compounds, and the fully gapped states were achieved using a DFT+U method [133]. To stabilize the non-collinear magnetic calculation, we used the norm-conserving (NC) pseudopotentials from PseudoDojo [134]. For convergence reasons we implemented the Perdew-Zunger (PZ) functional in the calculation of $Ag_3LiRh_2O_6$, while leaving the default Perdew-Burke-Ernzerhof (PBE) functional for Li_2RhO_3. To compare with the previous report of the insulating states in Li_2RhO_3 [56], we fixed the Hund's coupling to $J = 0.7$ eV and tuned the Hubbard-U from 1 to 4 eV. Our results were consistent with the prior work. The real-space tight-binding functions (involving the Rh-$4d$ and O-$2p$ orbitals as well as Ag-$4d$ orbitals for $Ag_3LiRh_2O_6$) were derived from the band structure using maximally-localized Wannier states implemented by the Wannier90 software [135]. From here, tight-binding models for a single RhO_6 cluster were constructed

based on the obtained real-space hopping parameters. The eigenstates of such a RhO_6 cluster were used to compute $\langle \mathbf{L} \cdot \mathbf{S} \rangle$ and the traces in Fig. 5.8.[3]

5.2.7 X-ray Absorption Spectroscopy

The x-ray absorption near edge structure (XANES) data at the Rh and Ag $L_{2,3}$ edges were collected at tender energy beamline 8-BM of the National Synchrotron Light Source II, and at beamline 4-ID-D of the Advanced Photon Source, respectively. The Rh $L_{2,3}$ data were collected in total electron yield (TEY) mode using powder samples in a helium gas environment. The Ag $L_{2,3}$ data were collected in partial fluorescence yield (PFY) mode with powder samples in vacuum. Silicon and nickel mirrors together with detuning of the second Si(111) monochromator crystal were used to reject high-energy harmonics. The PFY data were corrected for self-absorption [136].[4]

5.3 Results

5.3.1 Magnetic Properties

A small peak at $T_\mathrm{g} = 6.0(5)$ K in Li_2RhO_3 with a splitting between the zero-field-cooled (ZFC) and field-cooled (FC) susceptibility data ($\chi(T)$ in Fig. 5.6a) confirms the spin-glass transition as reported in earlier works [40, 41, 56]. In stark contrast, $Ag_3LiRh_2O_6$ exhibits a robust AFM order with a pronounced peak in $\chi(T)$ and without ZFC/FC splitting at the transition peak(Fig. 5.6b). The transition temperature in $Ag_3LiRh_2O_6$ can decrease because of an increase in the level of stacking faults and structural disorders such as rows of unwanted atoms in the honeycomb layers. A high-quality sample of the parent compound can help to

---

[3]The first principles calculations were performed by X. Hu and Prof. Y. Ran at Boston College.
[4]The x-ray absorption spectroscopy was performed by Dr. D. Haskel, Dr. Y. Du, and Dr. G. Fabbris.
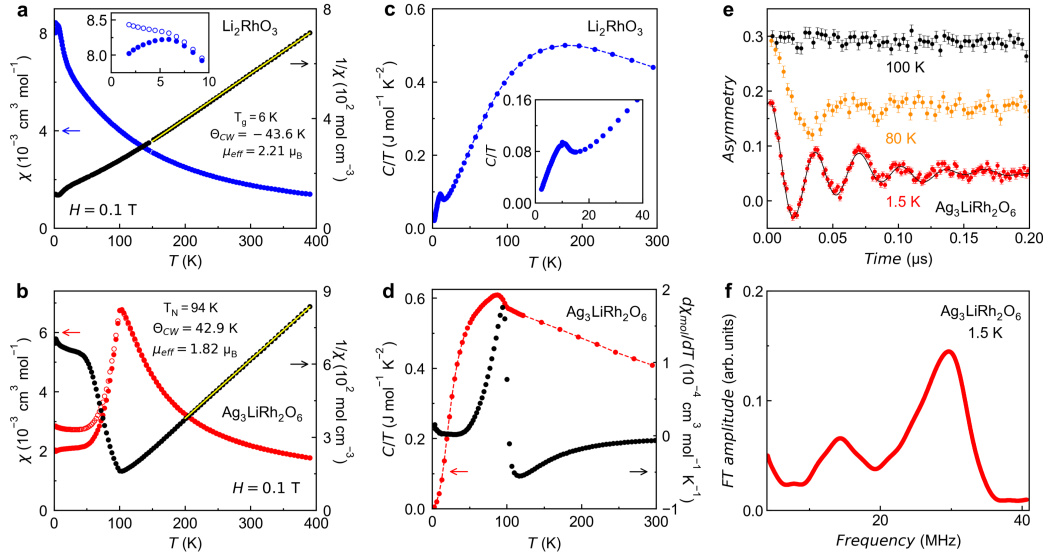
Figure 5.6: **Magnetic characterization.** Magnetic susceptibility plotted as a function of temperature and Curie-Weiss analysis presented in (**a**) Li_2RhO_3 (blue) and (**b**) $Ag_3LiRh_2O_6$(red). The ZFC and FC data are shown as full and empty symbols, respectively. Heat capacity as a function of temperature in (**c**) Li_2RhO_3 and (**d**) $Ag_3LiRh_2O_6$. The black circles in (**d**) show the derivative of magnetic susceptibility with respect to temperature. (**e**) μSR asymmetry plotted as a function of time in $Ag_3LiRh_2O_6$. For clarity, the curves at 100 and 80 K are offset with respect to the 1.5 K spectrum. The solid line is a fit to a Bessel function. (**f**) Fourier transform of the μSR spectrum at 1.5 K showing two frequency components.

107

prepare a high-quality of the Ag-exchange system. The small difference between the ZFC and FC curves at low temperatures is due to a small amount of stacking faults, which are carefully analyzed in Fig. 5.4. A Curie-Weiss analysis in Fig. 5.6b yields an effective moment of 1.82 μ_B and a $\Theta_{\text{CW}}^{\text{avg}} = 42.9$ K, consistent with a prior report [70]. A positive $\Theta_{\text{CW}}^{\text{avg}}$ refers to dominant FM interactions in the material and despite an AFM order suggests that $\chi(T)$ must be highly anisotropic, which is the case in materials with A-type or C-type AFM order. For example, $Na_3Ni_2BiO_6$ has a C-type AFM order (AFM intralayer and FM inter-layer) with $T_N = 10.4$ K and $\Theta_{\text{CW}}^{\text{avg}} = 13.3$ K [137].

Both the spin-glass transition in Li_2RhO_3 and the AFM transition in $Ag_3LiRh_2O_6$ are marked by peaks in the heat capacity in Fig. 5.6c,d. The heat capacity peak of $Ag_3LiRh_2O_6$ is visible despite the large phonon background at high temperatures, confirming a robust AFM order. The lattice-vibration contribution to the total amount of heat capacity is significantly larger in the high-temperature region; however, the AFM peak in $Ag_3LiRh_2O_6$ is clearly observed with no need to subtract a non-magnetic lattice analogue. We report $T_N = 94(3)$ K using the peak in $d\chi/dT$, which is close to the peak in the heat capacity (Fig. 5.6d). The transition temperature in AFM systems is reported from the derivative of magnetic susceptibility ($d\chi/dT$). T_N in $Ag_3LiRh_2O_6$ is nearly an order of magnitude larger than the transition temperature of any other 2D Kitaev material to date.

To obtain information about the local field within the magnetically ordered state of $Ag_3LiRh_2O_6$ we turned to μSR experiments. In Fig. 5.6e, the time-dependent μSR asymmetry curves in zero applied magnetic field show the appearance of spontaneous oscillations below 100 K, confirming the long-range magnetic order. The asymmetry spectrum at 1.5 K fits to a modified zeroth-order Bessel function [130], with the form of the fitting function indicating non-collinear incommensurate magnetic ordering. As shown in Fig. 5.6f, the Fourier transform of

the 1.5 K spectrum shows two peaks at 12 and 31 MHz, which we have modeled using a two-component expression. Each component has a distribution of local fields between a B_{min} and B_{max} indicating incommensurate ordering (Table 5.4). The center of distribution $(B_{min} + B_{max})/2$ is shifted from zero, indicating a non-collinear order [130].

The dominant frequency of 31 MHz in Fig. 5.6f corresponds to a maximum internal field of 0.231 T at the muon stopping site (using $\omega = \gamma_\mu B$ with the muon gyromagnetic ratio $\gamma_\mu = 851.6 \, \mathrm{Mrad \, s^{-1} T^{-1}}$), which is an order of magnitude larger than the internal field of 0.015 T extracted from μSR in Li_2RhO_3 [41]. μSR is a local probe, the dramatic change of the internal field in Li_2RhO_3 and $Ag_3LiRh_2O_6$ is due to a major change in the local field near Rh^{+4} sites in each compound. A mild trigonal distortion leads to an order-of-magnitude increase in both T_N and internal field, and implies a novel underlying interaction in the ground state. It is remarkable that a minor trigonal distortion induced by the topo-chemical reaction has led to such a dramatic change between the magnetic states of Li_2RhO_3 and $Ag_3LiRh_2O_6$.

5.3.1.1   Fitting the μSR Spectrum to a Bessel function

Figure 5.6f shows the Fourier transform (FT) of the μSR asymmetry spectrum at 1.5 K. The maximum and minimum peak frequencies in the FT spectrum are observed at 31 MHz and 12 MHz, corresponding to 2314 G and 883 G, respectively. The low temperature data suggest that we have two low-symmetry muon stopping sites and incommensurate magnetic ordering as described by the following depolarization function [130] (shown by the solid black curve in Fig. 5.6e):

$$G(t) = (1 - F) \sum_{i=1}^{2} f_i J_0(\gamma_\mu \Delta B_i t) \cos(\gamma_\mu B_{avg,i} t + \phi_i) \exp(-\lambda_{Ti} t) + F \exp(-\lambda_L t)$$

(5.2)

Table 5.4: Parameters for the fit of the data at T = 1.5 K to Equation 5.2.

	B_{max} (G)	B_{min} (G)	λ_T μs^{-1}	ϕ (deg)
Component 1	2316(10)	899(18)	5.1(11)	$-18(5)$
Component 2	2293(32)	1996(68)	15.3(30)	$-24(7)$

The field distributions are characterized by a field range $B_{min,i} \leq B \leq B_{max,i}$, with

$$\Delta B_i = \frac{B_{max,i} - B_{min,i}}{2}, \qquad B_{avg,i} = \frac{B_{max,i} + B_{min,i}}{2}, \qquad f_1 + f_2 = 1, \qquad 0 \leq F \leq 1 \tag{5.3}$$

and J_0 being the zeroth-order Bessel function of the first kind. At $T = 1.5$ K, $F = 0.275(2)$, $\lambda_L = 0.040(2)$ μs^{-1}, $f_1 = f_2 = 1/2$, and the component-specific parameters are listed in Table 5.4.

5.3.2 Theoretical Wave Functions

The drastic change of magnetic behavior between Li_2RhO_3 and $Ag_3LiRh_2O_6$ originates from a fundamental change of the spin-orbital quantum state (Fig. 5.7). In a perfect octahedral RhO_6 environment, the Rh d-orbitals split into t_{2g} and e_g manifolds. The t_{2g} manifold will further split into $J_{eff} = \frac{1}{2}$ and $J_{eff} = \frac{3}{2}$ due to the SOC interaction λ_{SOC}. The presence of a trigonal crystal field Δ_T can split t_{2g} manifold first and then SOC removes all the degeneracy of t_{2g} levels.

Both Li_2RhO_3 and $Ag_3LiRh_2O_6$ have Rh^{4+} in the $4d^5$ configuration, corresponding to one hole in the t_g manifold. Assuming that both compounds are in the Mott insulating regime (check the Methods), their low-energy physics should be described by a Kramers doublet per Rh^{4+} ion, i.e. they are effective spin-$\frac{1}{2}$ systems. However, the nature of the Kramers doublet may be significantly different depending on the interplay between λ_{SOC} and Δ_T. We illustrate this by considering two limits: the $J_{eff} = 1/2$ limit for $\lambda_{SOC} \gg \Delta_T$ relevant to Li_2RhO_3 (Fig. 5.7a)

and the Ising limit for $\Delta_\mathrm{T} \gg \lambda_\mathrm{SOC}$ relevant to $\mathrm{Ag_3LiRh_2O_6}$ (Fig. 5.7b). The wave functions of the low-energy Kramers doublet can be found in both limits using perturbation theory. The Kramers doublet in the $J_\mathrm{eff} = 1/2$ limit ($\lambda_\mathrm{SOC} \gg \Delta_\mathrm{T}$) comprises the following two states (Fig. 5.7a):

$$|j_{z,\uparrow}\rangle = \sqrt{\frac{2}{3}}|\mu_z, \uparrow\rangle + i\sqrt{\frac{1}{3}}|d_{z^2}, s_{z\downarrow}\rangle, \quad |j_{z,\downarrow}\rangle = \sqrt{\frac{2}{3}}|\mu_z, \downarrow\rangle + i\sqrt{\frac{1}{3}}|d_{z^2}, s_{z\uparrow}\rangle, \quad (5.4)$$

where $\{|\mu_{z,\uparrow}\rangle, |\mu_{z,\downarrow}\rangle\}$ are defined in Eq. 5.5 below. The $J_\mathrm{eff} = 1/2$ limit has been discussed extensively in the literature, and sizable Kitaev interactions have been proposed for materials in this limit such as the honeycomb iridates [1, 21, 23, 116], α-$\mathrm{RuCl_3}$ [121], and $\mathrm{Li_2RhO_3}$ [40, 41, 126]. The only difference between Eq. 5.4 and prior works [21] is that we choose the z-axis to be normal to the triangular face of the octahedron (Fig. 5.1b) instead of pointing at the apical oxygens.

In the Ising-limit ($\Delta_\mathrm{T} \gg \lambda_\mathrm{SOC}$), the trigonal distortion leads to new Kramers doublet states (Fig. 5.7b).

$$|\mu_{z,\uparrow}\rangle = -i\sqrt{\frac{1}{3}}|d_{x^2-y^2}, s_{z\uparrow}\rangle + i\sqrt{\frac{1}{6}}|d_{zx}, s_{z\uparrow}\rangle + \sqrt{\frac{1}{3}}|d_{xy}, s_{z\uparrow}\rangle + \sqrt{\frac{1}{6}}|d_{yz}, s_{z\uparrow}\rangle,$$

$$|\mu_{z,\downarrow}\rangle = i\sqrt{\frac{1}{3}}|d_{x^2-y^2}, s_{z\downarrow}\rangle - i\sqrt{\frac{1}{6}}|d_{zx}, s_{z\downarrow}\rangle + \sqrt{\frac{1}{3}}|d_{xy}, s_{z\downarrow}\rangle + \sqrt{\frac{1}{6}}|d_{yz}, s_{z\downarrow}\rangle. \quad (5.5)$$

Note that the states $\{|j_{z,\uparrow}\rangle, |j_{z,\downarrow}\rangle\}$ are *not* orthogonal to states $\{|\mu_{z,\uparrow}\rangle, |\mu_{z,\downarrow}\rangle\}$, despite being in opposite limits.

The trigonal splitting energy scale Δ_T is known to split the six-fold degenerate t_g levels (including spin degrees of freedom) into a two-fold $a_{1\mathrm{g}}$ manifold and a four-fold e'_g manifold (Fig. 5.7b) [119]. Choosing $\hat{x}$ and $\hat{y}$ directions pointing towards oxygen atoms as shown in Fig. 5.1b, the orbital wave functions are found to be
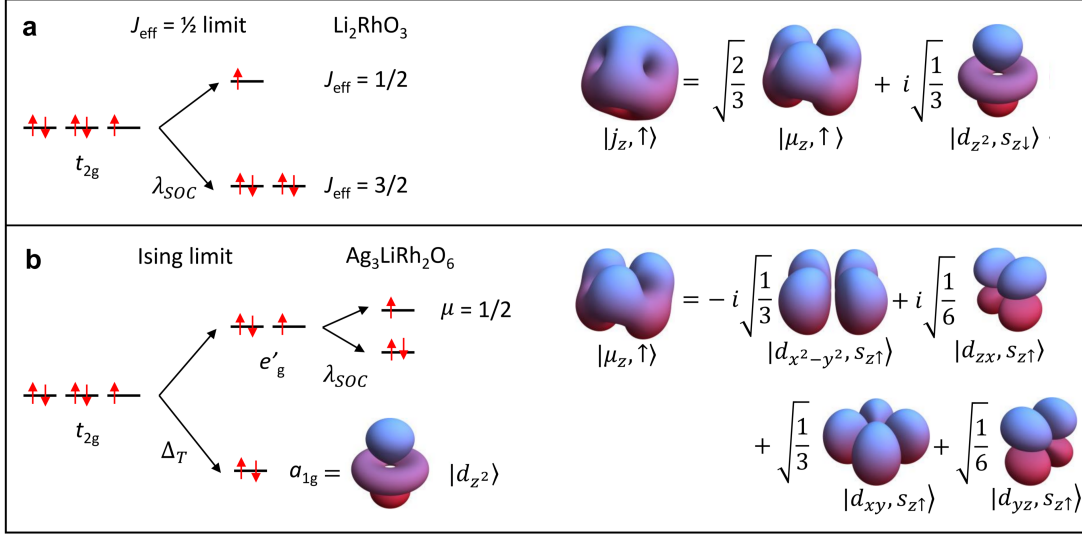
Figure 5.7: **Wave functions.** (a) The $J_{\text{eff}} = 1/2$ limit, realized in Li_2RhO_3, where $\lambda_{\text{SOC}} \gg \Delta_T$. The probability density is visualized for the isospin-up wave function. (b) The Ising limit, realized in $\text{Ag}_3\text{LiRh}_2\text{O}_6$, where $\Delta_T \gg \lambda_{\text{SOC}}$. The probability density is visualized for the spin-up wave function. Notice the cubic and trigonal symmetries of the J_z and μ_z orbitals, respectively.

$|d_{z^2}\rangle$ for a_{1g} (Fig. 5.7b), and $\{|\tau_{z,\uparrow}\rangle, |\tau_{z,\downarrow}\rangle\}$ for e'_g:

$$|\tau_{z,\uparrow}\rangle \equiv \sqrt{\frac{2}{3}}|d_{x^2-y^2}\rangle - \sqrt{\frac{1}{3}}|d_{zx}\rangle, \quad |\tau_{z,\downarrow}\rangle \equiv \sqrt{\frac{2}{3}}|d_{xy}\rangle + \sqrt{\frac{1}{3}}|d_{yz}\rangle, \tag{5.6}$$

In the materials under consideration, the trigonal distortion is a compression along the $\hat{z}$-axis (Fig. 5.1b) that lowers the energy of the a_{1g} level (Fig. 5.7b). Thus, for the $4d^5$ configuration, one should focus on the four-fold e'_g manifold. Unlike in the e_g manifold, the spin-orbit coupling is not completely quenched in the e'_g manifold. We show that the d-orbital angular momentum operator $\vec{L}$, after projection into the e'_g manifold, becomes:

$$L_x \to 0, \quad L_y \to 0, \quad L_z \to \tau_y, \tag{5.7}$$

where $\tau_{x,y,z}$ are the pseudospin Pauli matrices. We therefore have, in the e'_g man-

ifold

$$\lambda_{\text{SOC}} \, \vec{L} \cdot \vec{s} \to \lambda_{\text{SOC}} \, L_z s_z = \lambda_{\text{SOC}} \, \tau_y s_z \tag{5.8}$$

Namely, λ_{SOC} further splits the e'_{g} manifold into two Kramers doublets: τ_y anti-aligned with s_z, or τ_y aligned with s_z. The former doublet has a lower energy, so the latter doublet is half-filled in the $4d^5$ configuration. Finally, the low-energy effective spin-$\frac{1}{2}$ states in the Ising-limit are

$$|\mu_{z,\uparrow}\rangle = |\tau_y = +1, s_{z,\uparrow}\rangle, \quad |\mu_{z,\downarrow}\rangle = |\tau_y = -1, s_{z,\downarrow}\rangle \tag{5.9}$$

which are nothing but the states written in Eq. 5.5 and illustrated in Fig. 5.7b.

The exchange couplings for the effective μ-spins are expected to have the Ising anisotropy (easy-axis along the $\hat{z}$-direction). To understand its origin, one may consider exchange interactions like $J\vec{S}_i \cdot \vec{S}_j$ between two Rh sites i, j in the absence of the spin-orbit interaction. After λ_{SOC} is turned on, the $J\vec{S}_i \cdot \vec{S}_j$ needs to be projected onto the Kramers doublet $\{|\mu_{z,\uparrow}\rangle, |\mu_{z,\downarrow}\rangle\}$ at low energies. Only the term $JS_{i,z}S_{j,z}$ survives after the projection. In addition, the g-factor of the effective μ-spins in a magnetic field is also expected to be significantly anisotropic. For example, the effective μ-spins do not couple with a magnetic field along the $\hat{x}$ (or $\hat{y}$) axis in a linear fashion in this limit. A direct measurement of the magnetic response with respect to the field direction is not possible at this stage because single crystals of $Ag_3LiRh_2O_6$ are not available. However, indirect evidence of such anisotropic interactions may be the positive Curie-Weiss temperature in polycrystalline samples of $Ag_3LiRh_2O_6$ (Fig 5.6b) that indicates FM interactions despite the AFM ordering. Such a behavior has been reported in $Na_3Ni_2BiO_6$ and attributed to a C-type AFM order where the coupling within the layers is AFM and between the layers is FM [137].

5.3.2.1 Quenching of L_x, L_y in e'_g Orbitals and Derivation of $|\mu_{z,\uparrow\downarrow}\rangle$ Kramers Doublet

To prove Eq. 5.7, we show explicitly that the effective angular momentum operator (within t_{2g} orbitals) vanishes for x and y components. The angular momentum matrix for standard 4d-orbitals $\{|d_{xy}\rangle, |d_{yz}\rangle, |d_{zx}\rangle, |d_{z^2}\rangle, |d_{x^2-y^2}\rangle\}$ takes the form of

$$
L_x = \begin{pmatrix}
0 & 0 & -i\hbar & 0 & 0 \\
0 & 0 & 0 & -i\sqrt{3}\hbar & -i\hbar \\
i\hbar & 0 & 0 & 0 & 0 \\
0 & i\sqrt{3}\hbar & 0 & 0 & 0 \\
0 & i\hbar & 0 & 0 & 0
\end{pmatrix},
\tag{5.10}
$$

$$
L_y = \begin{pmatrix}
0 & i\hbar & 0 & 0 & 0 \\
-i\hbar & 0 & 0 & 0 & 0 \\
0 & 0 & 0 & i\sqrt{3}\hbar & -i\hbar \\
0 & 0 & -i\sqrt{3}\hbar & 0 & 0 \\
0 & 0 & i\hbar & 0 & 0
\end{pmatrix},
\tag{5.11}
$$

$$
L_z = \begin{pmatrix}
0 & 0 & 0 & 0 & 2i\hbar \\
0 & 0 & i\hbar & 0 & 0 \\
0 & -i\hbar & 0 & 0 & 0 \\
0 & 0 & 0 & 0 & 0 \\
-2i\hbar & 0 & 0 & 0 & 0
\end{pmatrix}.
\tag{5.12}
$$

The octahedral environment will split the ten-fold degenerate 4d orbitals (spin degeneracy included) into six-fold degenerate t_{2g} orbitals and four-fold degenerate

e_g orbitals. In the usual basis where the t_{2g} subspace is spanned by

$$\left\{ \frac{1}{\sqrt{2}} \left(|d_{zx}\rangle - i|d_{yz}\rangle \right), i|d_{xy}\rangle, \frac{1}{\sqrt{2}} \left(|d_{zx}\rangle + i|d_{yz}\rangle \right) \right\},$$

the 3×3 block of L_x, L_y, and L_z matrices will take exactly the same form as the angular momentum matrix of p-orbitals (with an additional minus sign). This is known as the t_{2g}-p equivalence.

However, for convenience of the study of trigonal distortion, we follow Ref. [119] to choose the coordinate system with the $\hat{z}$-axis perpendicular to the O triangles, as shown in the Fig. 5.1b. Now, the t_{2g} basis becomes

$$|a_{1g}\rangle = |d_{z^2}\rangle, \quad |e'_{g1}\rangle = \sqrt{\frac{2}{3}}|d_{x^2-y^2}\rangle - \sqrt{\frac{1}{3}}|d_{zx}\rangle, \quad |e'_{g2}\rangle = \sqrt{\frac{2}{3}}|d_{x^2-y^2}\rangle + \sqrt{\frac{1}{3}}|d_{zx}\rangle.$$
(5.13)

Projecting the angular momentum matrices (Eqs. 5.10, 5.11, and 5.12) onto the $\{|a_{1g}\rangle, |e'_{g1}\rangle, |e'_{g2}\rangle\}$ basis yields

$$L_{\text{eff},x} = \begin{pmatrix} 0 & 0 & i\hbar \\ 0 & 0 & 0 \\ -i\hbar & 0 & 0 \end{pmatrix}, \quad L_{\text{eff},y} = \begin{pmatrix} 0 & i\hbar & 0 \\ -i\hbar & 0 & 0 \\ 0 & 0 & 0 \end{pmatrix}, \quad L_{\text{eff},z} = \begin{pmatrix} 0 & 0 & 0 \\ 0 & 0 & -i\hbar \\ 0 & i\hbar & 0 \end{pmatrix}.$$
(5.14)

For the $4d^5$ configuration of electrons, the low-energy physics occurs within the subspace of $\{|e'_{g1}\rangle, |e'_{g2}\rangle\}$, in which only the z-component of angular momentum matrix is non-vanishing, reading

$$L_{\text{eff},z}\big|_{e'_g} = \hbar\tau_y, \quad \tau_y \equiv \begin{pmatrix} 0 & -i \\ i & 0 \end{pmatrix}.$$
(5.15)

If we take into account the spin-orbital coupling, the on-site Hamiltonian ma-

115

trix, in the basis of $\{|e'_{g1}\rangle \otimes |s_{z,\uparrow}\rangle, |e'_{g1}\rangle \otimes |s_{z,\downarrow}\rangle, |e'_{g2}\rangle \otimes |s_{z,\uparrow}\rangle, |e'_{g2}\rangle \otimes |s_{z,\downarrow}\rangle\}$, is

$$H_{\text{SOC}} = \lambda_{\text{SOC}} \ \hbar \tau_y \otimes s_z = \begin{pmatrix} 0 & 0 & -\frac{1}{2}i\lambda\hbar^2 & 0 \\ 0 & 0 & 0 & \frac{1}{2}i\lambda\hbar^2 \\ \frac{1}{2}i\lambda\hbar^2 & 0 & 0 & 0 \\ 0 & -\frac{1}{2}i\lambda\hbar^2 & 0 & 0 \end{pmatrix}, \qquad (5.16)$$

with eigen-energies $\{-\frac{\lambda\hbar^2}{2}, -\frac{\lambda\hbar^2}{2}, \frac{\lambda\hbar^2}{2}, \frac{\lambda\hbar^2}{2}\}$. In the $4d^5$ configuration, it is the Kramers pair with energy $\frac{\lambda\hbar^2}{2}$ that describes the low-energy physics. The eigenstates read

$$|\mu_{z,\uparrow}\rangle \equiv \left(-\frac{i}{\sqrt{2}}|e'_{g1}\rangle + \frac{1}{\sqrt{2}}|e'_{g2}\rangle\right) \otimes |s_{z,\uparrow}\rangle, \quad |\mu_{z,\downarrow}\rangle \equiv \left(\frac{i}{\sqrt{2}}|e'_{g1}\rangle + \frac{1}{\sqrt{2}}|e'_{g2}\rangle\right) \otimes |s_{z,\downarrow}\rangle.$$
$$(5.17)$$

Inserting the $4d$-orbital representation of $|e'_{g1}\rangle$ and $|e'_{g2}\rangle$ (from Eq. 5.13), we arrive at Eq. 5.9.

5.3.3 Spectroscopic Evidence

We provide spectroscopic confirmation of the theoretical picture by measuring the branching ratio using x-ray absorption spectroscopy (XAS). Figure 5.8a shows the XAS data from a Li_2RhO_3 sample with the Rh L_3 and L_2 edges near 3.00 and 3.15 keV, respectively. The Rh L_3 shows a shoulder which is an evidence of holes in t_{2g} levels. In order to estimate $\langle \mathbf{L} \cdot \mathbf{S} \rangle$ in each compound we measured the branching ratio. The branching ratio, $BR = I(L_3)/I(L_2) = 3.17(1)$, is evaluated by dividing the shaded areas (difference between the step and Gaussian functions) under the L_3 and L_2 peaks in Fig. 5.8a. A similar analysis in $Ag_3LiRh_2O_6$ yields $BR = 2.22(1)$ (Fig. 5.8b). The branching ratio is related to the SOC through $BR = (2+r)/(1-r)$, where $r = \langle \mathbf{L}\cdot\mathbf{S}\rangle/n_h$ with n_h being the number of holes in the $4d$ shell [138, 139]. Using $n_h = 5$ for Rh^{4+}, we obtain $\langle \mathbf{L}\cdot\mathbf{S}\rangle = 1.40$ in Li_2RhO_3 and
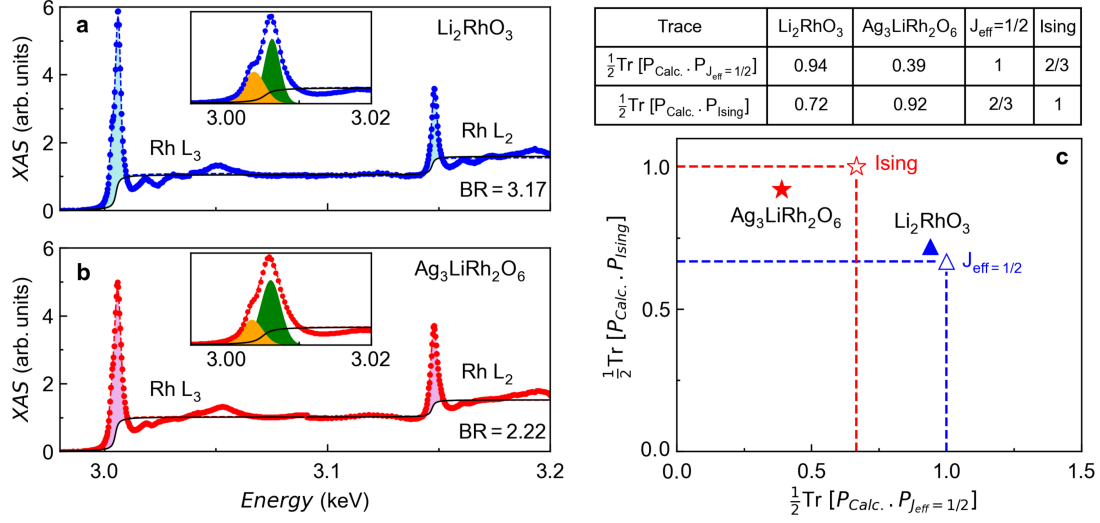
Figure 5.8: **X-ray absorption spectroscopy (XAS).** (**a**) XAS data from Rh $L_{2,3}$ edges of Li_2RhO_3. The data were modeled with a step and two Gaussian functions for the L_3 edge (inset), and one Gaussian function for the L_2 edge. (**b**) Similar data and fits for the Rh $L_{2,3}$ edges of $Ag_3LiRh_2O_6$. (**c**) Theoretically calculated traces of projector products are tabulated and plotted for both the ideal limits (empty symbols) and real materials (full symbols).

0.34 in $Ag_3LiRh_2O_6$. This is consistent with the above theoretical picture based on $\lambda_{SOC} \gg \Delta_T$ and the J_{eff} limit in Li_2RhO_3 compared to $\Delta_T \gg \lambda_{SOC}$ and the Ising limit in $Ag_3LiRh_2O_6$.

Note that the spectroscopic value of $\langle \mathbf{L} \cdot \mathbf{S} \rangle$ is small but non-vanishing in $Ag_3LiRh_2O_6$. The fine structure of Rh L edge with a shoulder near the L_3 peak (inset of Fig. 5.8b) that is absent in the L_2 peak confirms a finite SOC in $Ag_3LiRh_2O_6$ [140]. As illustrated in Fig. 5.7b, a weak SOC is necessary to split the e'_g levels. The fine structure of the Rh L_3 edge can be fitted to two Gaussian curves in both Li_2RhO_3 and $Ag_3LiRh_2O_6$ (insets of Fig. 5.8a,b). A higher ratio between the two Gaussian areas in $Ag_3LiRh_2O_6$ (2.42) than in Li_2RhO_3 (1.53) is consistent with a weaker SOC in the former. Supporting information about the Ag L edge is provided in Fig. 5.9 to confirm the Ag^+ oxidation state [141, 142].
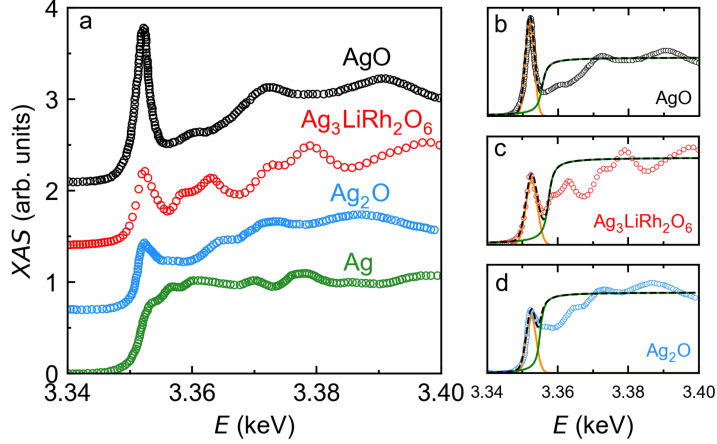
Figure 5.9: **XAS data of the Ag L edge.** (**a**) Comparison of Ag L_3 XAS data for Ag, Ag_2O, $Ag_3LiRh_2O_6$, and AgO. The curves for the oxides are shifted for better visibility. The Ag metal and Ag oxide data are taken from Ref. [142]. The energy scale of $Ag_3LiRh_2O_6$ is arbitrarily shifted by -1.6 eV to align its white line with that of the Ag_2O spectrum (due to different energy calibration compared to Ref. [142]). The XAS data were modeled with a broadened step and a Gaussian function in (**b**) AgO, (**c**) $Ag_3LiRh_2O_6$, and (**d**) Ag_2O.

5.3.3.1 Ag L_3 Edge XAS Data

We focused on the Rh $L_{2,3}$ edges to evaluate the branching ratio and expectation value $\langle \mathbf{L} \cdot \mathbf{S} \rangle$ assuming a Rh^{4+} state. This assumption relies on having the Ag^+ oxidation state in $Ag_3LiRh_2O_6$, which can be confirmed through XAS measurements of the Ag L-edge. Figure 5.9a compares the Ag L_3 edge data from our $Ag_3LiRh_2O_6$ sample to the published data for Ag, Ag_2O, and AgO measured by Kolobov [142], all collected in fluorescence yield mode and corrected for self-absorption. For proper comparison, the edge jumps in all data sets are normalized to unity. Note that metallic Ag has a full $4d^{10}$ shell, hence the absence of a white line in its spectrum. Note also that the size of the white line in $Ag_3LiRh_2O_6$ is closer to that of Ag_2O (Ag^+) than AgO (Ag^{2+}). We fit the AgO, $Ag_3LiRh_2O_6$, and Ag_2O data to a broadened step function (arctan) and a Gaussian peak in Fig. 5.9b,c, d, respectively. The area under the Gaussian is 5.01 for AgO, 3.05 for $Ag_3LiRh_2O_6$, and 2.32 for Ag_2O. Thus, the oxidation state is close to Ag^+ in

$Ag_3LiRh_2O_6$, but with a small fraction (less than 0.2) of additional holes. A more precise estimation of the Ag oxidation state is not possible, because the height of the white line depends also on the degree of Ag-O bond covalency ([141]). Nevertheless, it is clear that Ag is much closer to Ag^+ than Ag^{2+} in $Ag_3LiRh_2O_6$, justifying our assumption of Rh^{4+}.

5.3.4 Density Functional Theory (DFT)
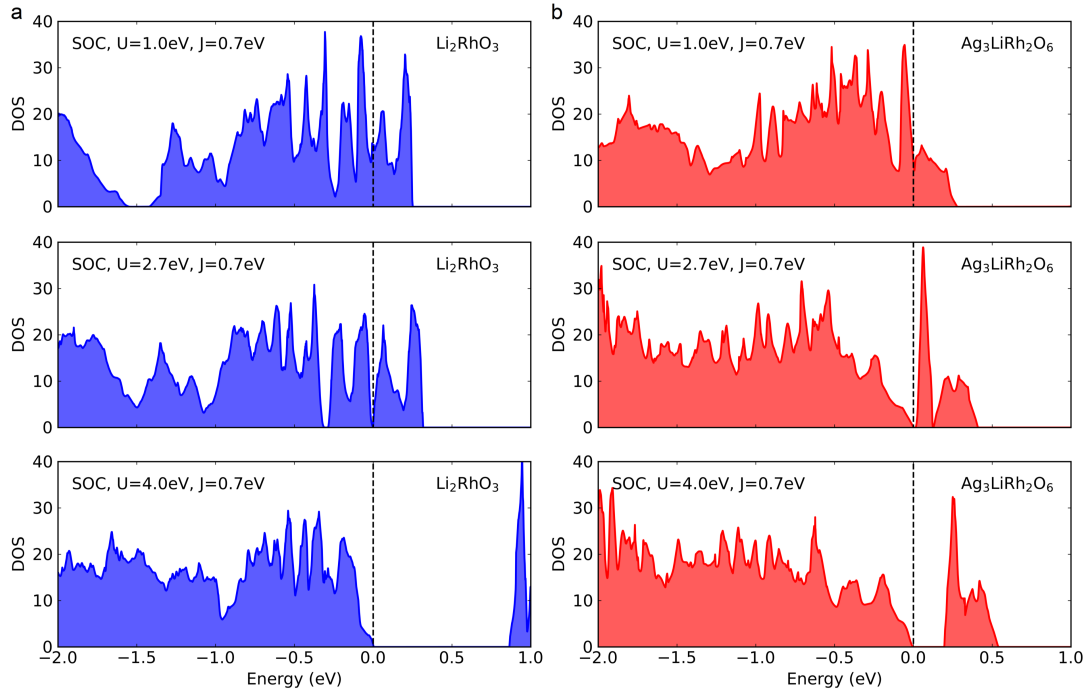
Figure 5.10: **Electronic structure.** Density of states within the t_{2g} manifold is shown for (**a**) Li_2RhO_3 and (**b**) $Ag_3LiRh_2O_6$ from a DFT+U+SOC calculation in the presence of zigzag magnetic order. In both cases, a magnetic gap opens at approximately $U = 2.7$ eV, and it grows with increasing U. The gap is larger in Li_2RhO_3 than in $Ag_3LiRh_2O_6$.

We performed DFT+U calculations in the presence of SOC for the zigzag AFM ordered states in both Li_2RhO_3 and $Ag_3LiRh_2O_6$ (Fig. 5.10a,b). Although the zigzag order is known to be the energetically favorable state in Li_2RhO_3 ([56]), it is unclear whether it is still the ground state for $Ag_3LiRh_2O_6$. The fully first-principle investigation of the magnetic ground state of $Ag_3LiRh_2O_6$ is beyond the

scope of this work, so we choose the zigzag order for this material merely as a demonstration. This calculation still provides important information about the magnetic anisotropy because the magnetic moment direction in our calculation is not constrained. If $Ag_3LiRh_2O_6$ has a large Ising anisotropy, the ground state moment direction will be essentially along the z-direction normal to the honeycomb planes.

We chose Hund's coupling $J_H = 0.7$ eV throughout the calculation, consistent with previous works on Li_2RhO_3 ([56]), while the Hubbard-U is tuned to study the evolution of the band gap due to magnetic ordering. Figure 5.10 shows only the t_{2g} levels since the e_g levels are about 3 eV higher in energy and irrelevant to the problem. We found that, in both materials, the magnetic gap is opened when U is larger than about 2.7 eV. However, the energy gap in Li_2RhO_3 quickly increases as U increases further, while the energy gap in $Ag_3LiRh_2O_6$ is significantly smaller. When $U = 4$ eV, the gap is approximately 0.9 eV for Li_2RhO_3 and 0.2 eV for $Ag_3LiRh_2O_6$. The smaller gap in the silver compound is consistent with the resistivity data shown in Fig. 5.3. We also show the evolution of the gap with increasing U in Fig 5.11.
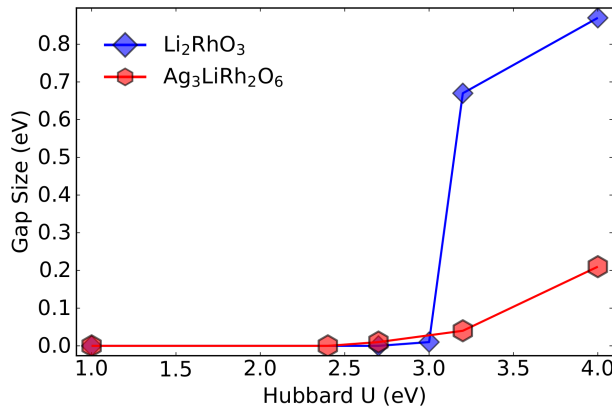
Figure 5.11: **Evolution of the gap.** The magnetic gap is evaluated at several values of Hubbard-U for both Li_2RhO_3 (blue) and $Ag_3LiRh_2O_6$ (red).

In both materials, the DFT value for (spin) magnetic moment is close to 1 μ_B

per Rh-site when $U = 4$ eV, consistent with the low-spin configuration of $4d^5$. To be specific, the absolute magnetization is 3.7 and 3.4 μ_B/cell in Li_2RhO_3 and $Ag_3LiRh_2O_6$, respectively, which yield 0.92 and 0.85 μ_B/Rh since there are 4 Rh atoms/cell. The direction of Rh atomic magnetization in Li_2RhO_3 is at 59° with respect to the z-axis, whereas in $Ag_3LiRh_2O_6$, it is only 2° away from the z-axis. Thus, our DFT results show that in Li_2RhO_3, the magnetic moment of the Rh atom significantly deviates from the z-direction (consistent with the fact that the system is closer to the $J = 1/2$ limit), while in $Ag_3LiRh_2O_6$ the magnetic moment is basically along the z-direction. This indicates that $Ag_3LiRh_2O_6$ has an easy-axis spin anisotropy, consistent with other theoretical evidence reported here.

Finally, we summarize the energy levels and DFT values of $\langle \mathbf{L} \cdot \mathbf{S} \rangle$ for each energy level within the t_{2g} manifold of both compounds in Table 5.5. The six t_{2g} levels in $Ag_3LiRh_2O_6$ split into a low energy a_{1g} doublet, and a high energy e'_g quartet due to the trigonal distortion. The e'_g quartet is further split into two Kramers doublets due to SOC. These CEF assignments are consistent with the crystal symmetries and confirmed by DFT. In Li_2RhO_3, it is better to consider that the six t_{2g} levels first split into a low energy $J = 3/2$ quartet and a high energy $J = 1/2$ doublet due to SOC. Then, the $J = 3/2$ quartet is further split into two Kramers doublets due to the weak lattice distortion.

Table 5.5: Energy levels within the t_{2g} manifold of Li_2RhO_3 and $Ag_3LiRh_2O_6$. The top (half-filled) Kramers doublet energy is set to zero.

Li$_2$RhO$_3$			Ag$_3$LiRh$_2$O$_6$		
Character	Energy (eV)	$\langle \mathbf{L} \cdot \mathbf{S} \rangle$	Character	Energy (eV)	$\langle \mathbf{L} \cdot \mathbf{S} \rangle$
$J = 1/2$	0	0.93	e'_g	0	0.82
$J = 3/2$	-0.18	-0.50	e'_g	-0.15	-0.56
$J = 3/2$	-0.23	-0.58	a_{1g}	-0.38	-0.37

5.4 Discussion and Conclusion

We have demonstrated that a competition between SOC and trigonal distortion could tune a honeycomb structure between the Kitaev ($J_{\text{eff}} = \frac{1}{2}$) and Ising ($\mu = \frac{1}{2}$) limits. Our magnetization, μSR, and XAS data suggest that Li_2RhO_3 is closer to the $J_{\text{eff}} = 1/2$ limit, whereas $Ag_3LiRh_2O_6$ is closer to the Ising limit. We calculated the ideal wave functions and visualized them in Fig. 5.7. However, a realistic material is generally situated on a spectrum between these two ideal limits. For example, minor lattice distortions (e.g. monoclinic) can further break the trigonal point group symmetry and perturb the ideal wave function.

To make our theoretical discussion more realistic, we calculated the band structure of Li_2RhO_3 and $Ag_3LiRh_2O_6$ from first principles and obtained a real-space tight-binding model for each compound. Details of the electronic structure calculations in the presence of Hubbard-U, SOC, and zigzag magnetic ordering are presented in Figs. 5.10 and 5.11, and Table 5.5. The full orbital content of the energy eigenstates was characterized using a combination of Quantum-Espresso and Wannier90 software [131, 132, 135]. This allowed us to quantitatively investigate the regimes being realized in Li_2RhO_3 and $Ag_3LiRh_2O_6$. Specifically, given a Kramers doublet $|\psi_1\rangle$ and $|\psi_2\rangle$, we defined the projectors:

$$P_\psi \equiv |\psi_1\rangle\langle\psi_1| + |\psi_2\rangle\langle\psi_2| \tag{5.18}$$

For example, $P_{J_{\text{eff}}=1/2}$ and P_{Ising} are projectors defined using the Kramers doublets in the $J_{\text{eff}} = 1/2$ limit (Eq. 5.4) and the Ising limit (Eq. 5.5), respectively. We then compute the traces $\frac{1}{2}\text{Tr}[P_{calc.} \cdot P_{J_{\text{eff}}=1/2}]$ and $\frac{1}{2}\text{Tr}[P_{calc.} \cdot P_{\text{Ising}}]$, the probability of projecting the calculated state to Ising limit and the probability of projecting the calculated state to $J_{\text{eff}} = 1/2$ limit. The results are tabulated and visualized in Fig. 5.8c. These traces would be unity if the calculated system was in the ideal

$J_{\text{eff}} = 1/2$ or Ising limit. Figure 5.8c clearly locates Li_2RhO_3 and $Ag_3LiRh_2O_6$ in the vicinity of the $J_{\text{eff}} = 1/2$ and Ising ($\mu = 1/2$) limits, respectively.

Our combined experimental and theoretical results show how to change the fabric of spin-orbit coupled states and dramatically change the magnetic behavior of the Kitaev materials. Despite theoretical proposals for a diverse global phase diagram, the current Kitaev systems are all in the $J_{\text{eff}} = 1/2$ limit [1, 21, 23, 38, 116, 117, 121, 143–145]. Finding an outlier, such as $Ag_3LiRh_2O_6$, in the phase diagram (Fig. 5.1a) provides the first glimpse at the diversity of magnetic phases that can be engineered using topo-chemical methods. Specifically, the interplay between the Kitaev and Ising limits will be a fruitful venue to search for novel non-collinear magnetic orders beyond the familiar Kitaev-Heisenberg paradigm.[5]

CHAPTER VI

Thermodynamic Behavior of the Monoclinic Kitaev Magnet $Na_2Co_2TeO_6$

6.1 Introduction

Achieving an ideal quantum spin-liquid (QSL) with long-range entanglement and fractionalized anyonic excitations has become one of the most sought-after accomplishments in condensed matter physics [1, 3, 4]. One of the most promising theoretical models that can host a QSL phase in its ground-state is the Kitaev model, which features bond-dependent Ising interactions on a honeycomb lattice and an exactly solvable Hamiltonian for spin-1/2 particles [20]. Experimental efforts to materialize the Kitaev model have led to the discovery of honeycomb layered candidates such as α-Li_2IrO_3, Na_2IrO_3, Li_2RhO_3, and α–$RuCl_3$ [35, 36, 38, 56, 57]. Recent progress in intercalation chemistry has led to a second generation of such compounds as Cu_2IrO_3, $Ag_3LiIr_2O_6$, $Ag_3LiRh_2O_6$, $Cu_3LiIr_2O_6$, and $H_3LiIr_2O_6$ [33, 44, 55, 59–61, 64, 90, 108, 124]

In candidate Kitaev materials, the presence of strong spin-orbit coupling (SOC) can provide two crucial criteria for the Kitaev model: the creation of bond-directional Ising interactions as well as producing a spin-orbital Kramers doublet state [23, 29, 32]. Thus, the $4d$ and $5d$ transition-metal honeycomb structures

are heavily studied as potential candidates of the QSL phase compared to the $3d$ transition-metals. In the presence of an octahedral crystal electric field (CEF), the d^5 transition-metals with low-spin electron configuration, such as the Ir^{4+}, Rh^{4+}, and Ru^{3+} ions, fill only the t_{2g}^5 levels and leave the e_g^0 levels empty. The low-energy physics of these edge-shared octahedrally coordinated transition metals can therefore be described by a spin-orbital Kramers doublet or $J_{eff} = 1/2$ state [30–32].

The $3d$ transition metals are lighter compared to $4d$ and $5d$ transition metals thus they are in a weaker SOC limit. Furthermore, they have more localized d orbitals compared to $4d$ and $5d$ transition metals which have higher number of shells, thus the CEF effect is also weaker in this family. However theoretical studies have suggested that the anisotropic exchange interactions and pseudospin-1/2 state criteria can also be realized in $3d^7$ transition-metals such as Co^{2+} and Ni^{3+} ions with high-spin electron configuration $(t_{2g}^5 e_g^2)$, S = 3/2 and L = 1. The octahedral CEF and SOC effects in $3d$ transition metals can also form a pseudospin-1/2 Kramers doublet state with additional t_{2g}-e_g and e_g-e_g hopping interactions [32]. Thus, the $3d^7$ candidate transition metals, Co^{2+}/Ni^{3+} in a honeycomb structure are equally as likely as $4d^5$ and $5d^5$ transition-metal honeycomb materials to host a QSL phase [30–32]. Based on theoretical studies, the $3d^7$ system can be described by a Kitaev-Heisenberg model similar to the case for the $4d^5$ and $5d^5$ systems. For the high-spin d^7 configuration, the anisotropic Kitaev interactions can be only FM while the isotropic Heisenberg interactions can be both FM and AFM [32].

The tantalizing possibility of synthesizing Kitaev QSL candidate materials with earth-abundant and light elements such as Co and Ni instead of rare and heavy transition-metals (Ir and Rh) led to a surge of activity on candidate materials such as $Na_2Co_2SbO_6$ and $Na_2Co_2TeO_6$ [65–69, 146–149]. $Na_2Co_2SbO_6$ crystallizes in the same $C2/m$ space group as the iridates and shows an anti-ferromagnetic

(AFM) order at 8.3 K with a positive Curie-Weiss temperature of $\Theta_{CW} = +2.2$ K. It displays a weak hysteresis in the field dependence of its magnetization at 2 K, which suggests a competition between FM and AFM interactions in this material [65, 146]. The other cobaltate candidate, hexagonal $Na_2Co_2TeO_6$ crystallizes in the space group $P6_322$. It has been produced in both polycrystalline and single crystal forms, displays a clear downturn in the magnetic susceptibility of a polycrystalline sample at 27 K, and shows two anomalies at ∼15 K and ∼7 K. The obtained $\Theta_{CW} = $ -8.3 K for the polycrystalline sample confirms dominant AFM interactions and the absence of magnetic competition between FM and AFM interactions unlike $Na_2Co_2SbO_6$ [66, 150, 151].

Although both $Na_2Co_2SbO_6$ and hexagonal $Na_2Co_2TeO_6$ show honeycomb ordering in their crystal structures, $Na_2Co_2SbO_6$ in space group $C2/m$ has stronger inter-layer connections compared to hexagonal $Na_2Co_2TeO_6$ in space group $P6_322$. The latter space group permits a significant amount of Na deficiency between the honeycomb layers which randomizes the position of O atoms and causes higher levels of bond randomness (Na-O bonds) within the honeycomb layers. It also causes larger amounts of stacking faults in hexagonal cobalt tellurate that a splitting between ZFC and FC magnetic susceptibility data is a direct result of it [66, 151]. This reveals the advantage of synthesizing honeycomb materials in the space group $C2/m$, which allows for stronger inter-layer bonds, less stacking faults, and less bond randomness within the honeycomb layers due to having a fewer number inter-layer Wyckoff sites for Na atoms ($C2/m$ has two inter-layer Wyckoff sites for Na atoms while $P6_322$ has three sites).

In this chapter, I present the effect of crystal symmetry on the physics of a Kitaev material. I introduce a new polymorph of $Na_2Co_2TeO_6$ that crystallizes in the space group $C2/m$ instead of $P6_322$. Distinct from the hexagonal polymorph, it only displays a single AFM ordering peak at 9.6 K. We will show that the large

ZFC/FC splitting in hexagonal $Na_2Co_2TeO_6$, indicative of spin-glass and a higher level of stacking faults, has vanished in the monoclinic structure, confirming lower disorder levels in the monoclinic compound. We will also examine the response of the AFM order in this new polymorph to an applied magnetic field and compare it to the hexagonal cobaltate systems.

6.2   Experimental Methods

Polycrystalline samples of the new honeycomb layered material, monoclinic $Na_2Co_2TeO_6$, were synthesized via a solid-state reaction. The precursor materials sodium carbonate (Na_2CO_3, 99.5%), cobalt oxide (Co_3O_4, 99.7%), and tellurium oxide (TeO_2, 99.99%) were mixed and reacted according to

$$Na_2CO_3 + 0.67\,Co_3O_4 + TeO_2 \rightarrow Na_2Co_2TeO_6 \tag{6.1}$$
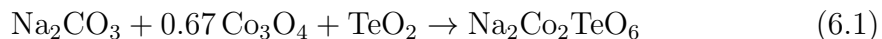
The resulting polycrystalline sample had a purple color and was fairly stable in air. We also synthesized the non-magnetic analog $Na_2Zn_2TeO_6$ with a similar synthesis approach as monoclinic $Na_2Co_2TeO_6$ to remove the phonon background from the heat capacity data. Powder x-ray diffraction (PXRD) measurements were performed using a Bruker D8 ECO instrument. The FullProf suite and VESTA software were used for the Rietveld refinements and crystal visualizations [76, 81]. Magnetization and heat capacity measurements were performed using a Quantum Design MPMS3 and PPMS Dynacool, respectively. Neutron powder diffraction (NPD) was performed on the time-of-flight (TOF) powder diffractometer, POW-GEN, located at the Spallation Neutron Source at Oak Ridge National Laboratory[1]. For NPD analysis, GSAS-II was used for Rietveld refinements [152].

---

[1]The powder neutron diffraction measurement has been done by Dr. Q. Zhang at Oak Ridge National Lab.

6.3   Crystal Structure

To confirm the crystal structure of the monoclinic $Na_2Co_2TeO_6$, we studied the crystal symmetry of this compound via both PXRD and NPD measurements and analysis. Figure 6.1(a) shows the PXRD pattern for the monoclinic polymorph of $Na_2Co_2TeO_6$ (red empty circles) and the result of Rietveld refinement (black solid line) using the $C2/m$ model. The refined values from PXRD refinement such as lattice parameters, Wyckoff site occupancies, and Debye-Waller factors are summarized in Table 6.1 and Table 6.2. The peaks in the region between 19° and 30° give information about the quality of the honeycomb ordering within the Co-Te layers. The well-separated and sharp honeycomb peaks observed in the monoclinic structure indicate proper honeycomb ordering with minimal stacking faults. In the presence of disorder and stacking faults, these peaks merge and form an asymmetric broad feature known as the Warren line shape commonly observed in disordered honeycomb systems [44, 63].

The amount of Na-deficiency at each Wyckoff site between the layers of monoclinic $Na_2Co_2TeO_6$ is significantly less than that of the hexagonal polymorph− a direct result of the change of space group. Therefore, structural disorders such as bond randomness within the honeycomb layers and stacking faults between them are fewer in the newly synthesized monoclinic cobalt tellurate system. The direct result of having fewer stacking faults also appears in the absence of splitting between ZFC/FC curves in the magnetic susceptibility data. The stacking fault disorder is reduced due to a stronger connection between the honeycomb layers in the monoclinic compound and presence of fewer Na-O bond randomness. However, due to the size of Na atoms, the Na atoms can also be located at the center of the honeycomb networks of Co, instead of Te atoms, and replace the Te atoms up to 8% of the total value. This can slightly change the structural properties in the monoclinic $Na_2Co_2TeO_6$.
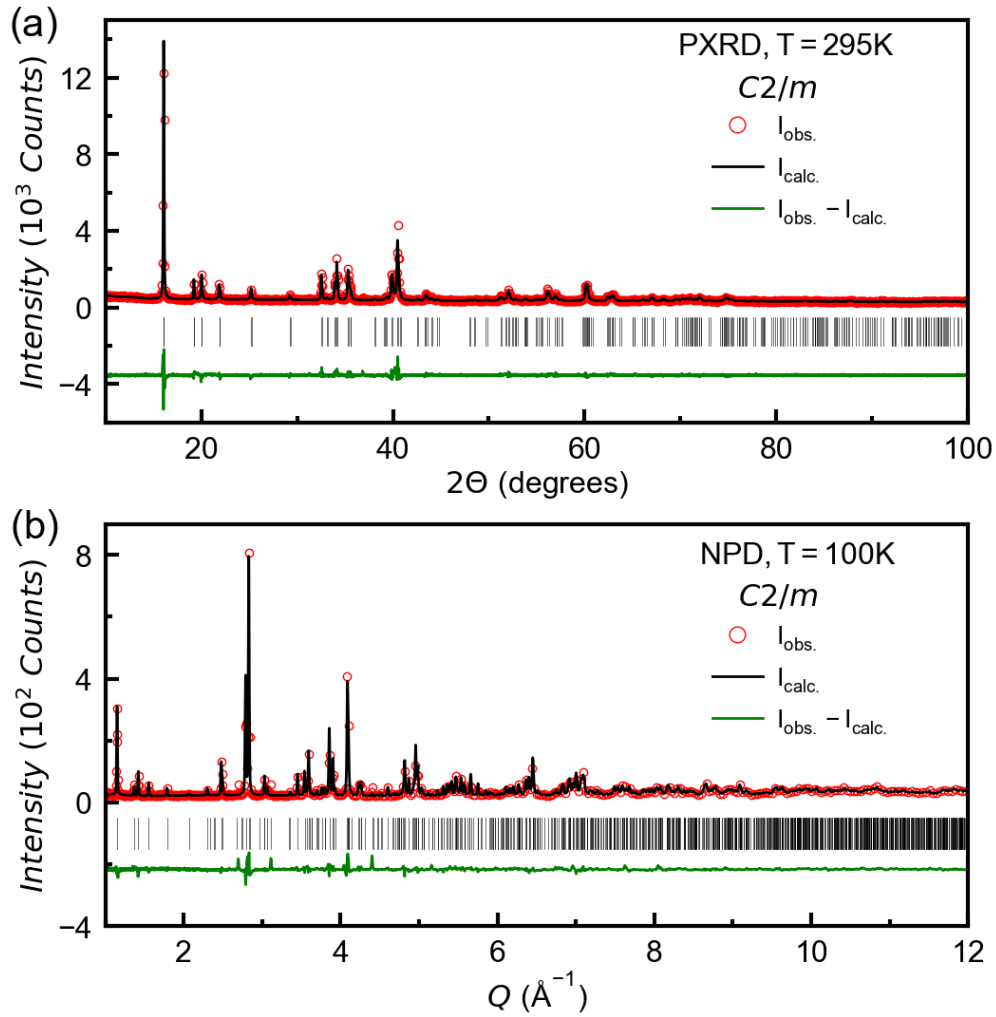
Figure 6.1: (a) Rietveld refinement on the PXRD pattern of monoclinic $Na_2Co_2TeO_6$ using $C2/m$ model. The x-ray source is Cu-K$_\alpha$ with a wavelength of 1.5406 Å. (b) Rietveld refinement on the neutron diffraction pattern of monoclinic $Na_2Co_2TeO_6$ at 100 K confirms the crystal symmetry and chemical composition. The NPD pattern also displays a small amount of Co_3O_4 impurity which is barely visible in the x-ray pattern. The wavelength for this measurement is 1.5 Å.

Table 6.1: Unit cell and Rietveld refinement quality factors for monoclinic $Na_2Co_2TeO_6$ from PXRD Rietveld refinement analysis.

Unit cell parameters		Refinement parameters	
Space Group	$C2/m$	Parameters	20
a (Å)	5.33225(6)	R_{Bragg} (%)	6.92
b (Å)	9.20808(8)	R_F (%)	5.57
c (Å)	5.80718(8)	R_{exp} (%)	5.38
β (°)	108.90837(88)	R_p (%)	5.72
V (Å^3)	269.745	R_{wp} (%)	7.69
Z	2	χ^2	2.04
ρ (gr cm^{-3})	4.770	T (K)	295

Table 6.2: Atomic coordinates, site occupancies, and the isotropic Debye-Waller factors for the Rietveld refinement of the monoclinic $Na_2Co_2TeO_6$ from PXRD Rietveld refinement analysis. The O Wyckoff positions are from the results of Rietveld refinement on neutron diffraction data.

atom	site	x	y	z	occ.	B_{iso} (Å^2)
Na1	$4h$	1/2	0.32122(097)	1/2	0.700	0.45
Na2	$2d$	0	1/2	1/2	0.600	0.45
Co1	$4g$	0	0.66690(33)	0	1.000	0.35
Te1	$2a$	0	0	0	1.000	0.35
O1	$8j$	0.28034	0.34572	0.80322	1.000	0.55
O2	$4i$	0.26464	1/2	0.19172	1.000	0.55

Figure 6.1(b) shows the results of a Rietveld refinement fit (black solid line) to the measured NPD pattern (red open circles). All the Bragg peaks are well indexed in space group $C2/m$ and verify our x-ray analysis. The structural analysis of NPD confirms the chemical composition and the crystal symmetry analysis of the PXRD data. The NPD measurements are very important due to the presence of light elements such as O which are not visible in the x-ray diffraction measurements. The x-ray pattern barely shows signs of impurity in the sample, while we were able to capture the Co_3O_4 (one of the precursors) from the neutron diffraction data.

6.4 Magnetism

Modification of the crystal symmetry and stronger connections between honeycomb layers in the new cobalt tellurate honeycomb polymorph lead to a lower transition temperature (T_N) compared to the hexagonal $Na_2Co_2TeO_6$, which orders at $T_N \sim 27$ K and shows two other AFM anomalies at ~ 15 K and ~ 7 K [14, 150, 151]. Figure 6.2(a) shows the DC magnetic susceptibility (χ) measured as a function of temperature at 0.05 T under the zero-field-cooled (ZFC) and field-cooled (FC) conditions. The ZFC and FC curves lie perfectly on top of each other at temperatures below and above the peak in the $\chi(T)$ data. This indicates a long-range AFM order without spin-glass behavior, consistent with minimal disorder in the monoclinic compound. The Néel temperature $T_N = 9.6$ K is determined from the peak in the derivative of the susceptibility, $d\chi/dT$, in the inset of Fig. 6.2(a).

We performed a Curie-Weiss (CW) analysis $(1/\chi = (T - \Theta_{CW})/ C)$, on the inverse susceptibility data for temperatures above 250 K in Fig. 6.2(a). From the fit, we extract a CW temperature of $\Theta_{CW} = +10.28$ K and an effective magnetic moment of $\mu_{eff} = 4.83\mu_B$. The positive sign of Θ_{CW} in the monoclinic $Na_2Co_2TeO_6$ indicates the presence of dominant FM interactions, unlike in hexagonal $Na_2Co_2TeO_6$ which has a negative CW temperature $(\Theta_{CW} = - 8.3$ K$)$. Thus,
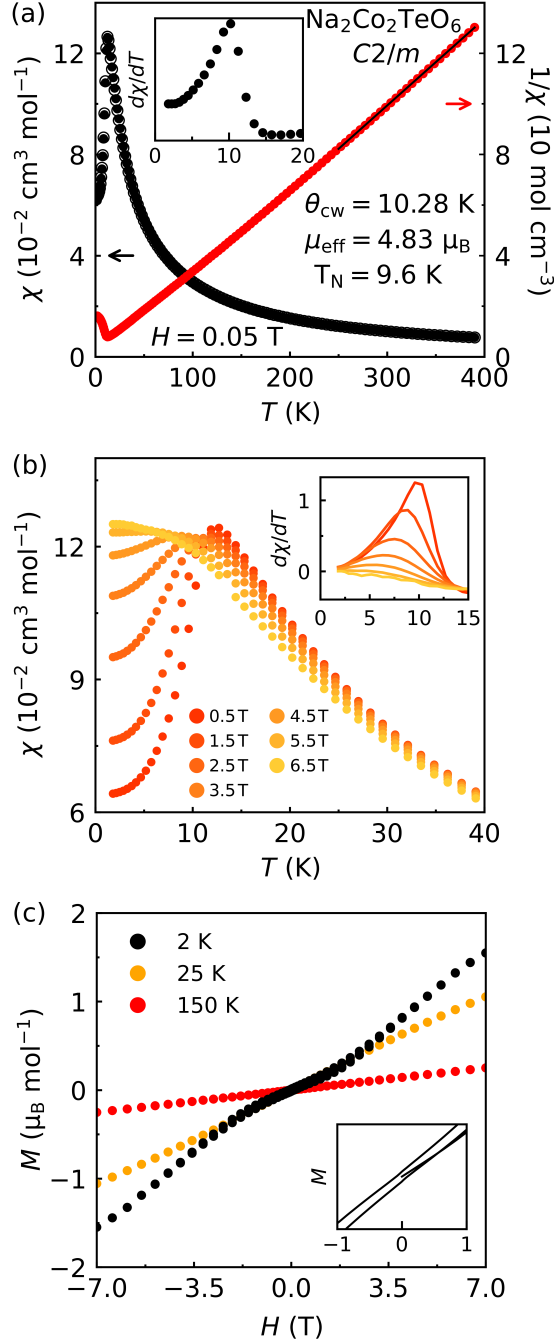
Figure 6.2: (a) Magnetic susceptibility per mole Co atom (black data) and inverse susceptibility (red data) are plotted as a function of temperature. The zero-field-cooled (ZFC) and field-cooled (FC) data are presented in filled and empty black circles, respectively. ZFC and FC curves follow each other very closely. A Curie-Weiss (CW) fit (black solid line) is performed on temperatures above 250 K. The inset shows the $d\chi_{mol}/dT$ vs temperature and is used to identify the transition temperature of the monoclinic polymorph of $Na_2Co_2TeO_6$. (b) Magnetic susceptibility as a function of temperature is plotted up to 6.5 T for $T < 40$ K. The AFM peak is suppressed with increasing magnetic field strength. (c) Magnetization as a function of magnetic field is shown at temperatures 2 K, 25 K, and 150 K. The inset shows a weak hysteresis for small fields at 2 K.

the anisotropy of the exchange interactions in monoclinic $Na_2Co_2TeO_6$ (AFM order and positive Θ_{CW}) must be larger than in hexagonal $Na_2Co_2TeO_6$ (AFM transition with negative Θ_{CW}). In this regards, the behavior of monoclinic $Na_2Co_2TeO_6$ is closer to that of $Na_2Co_2SbO_6$ which has a $\Theta_{CW} = +2.2$ K and AFM order at T_N = 8.3 K. The similar behavior of these two compounds must be related to having the same monoclinic structure ($C2/m$).

The effective moment of $4.83\mu_B$ in monoclinic $Na_2Co_2TeO_6$ is close to the value of $4.73\mu_B$ expected from a high-spin $3d^7$ system with S = 3/2 and L = 1 with unquenched orbital moment ($g = 1.6$ instead of 2). In contrast, the effective moments of hexagonal $Na_2Co_2TeO_6$ and $Na_2Co_2SbO_6$ are, respectively, $5.34\mu_B$ and $5.22\mu_B$, closer to the value $5.9\mu_B$ expected from a high-spin state with $g = 2$ [151]. Thus, the lower effective moment of the monoclinic cobalt tellurate compound is more consistent with a fully unquenched orbital degree of freedom and enough spin-orbit coupling to create a g-value smaller than 2. This can be interpreted as a stronger SOC in monoclinic $Na_2Co_2TeO_6$ compared to the other two cobaltate systems.

Figure 6.2(b) shows the effect of an applied field on the magnetic susceptibility in monoclinic $Na_2Co_2TeO_6$. Increasing the field suppresses the transition peak in χ by enhancing the low-temperature tail until the measured χ at 6.5 T saturates and behaves like a FM transition. A similar behavior is observed in hexagonal $Na_2Co_2TeO_6$ compound and is interpreted as the onset of a magnetically disordered state [66].

In Fig. 6.2(c) the magnetic field dependence of the magnetization in monoclinic $Na_2Co_2TeO_6$ is shown at temperatures 2 K, 25 K, and 150 K for fields up to 7 T. The magnetization in monoclinic $Na_2Co_2TeO_6$ reaches $1.6\mu_B$ at 2 K (black data) and has not saturated at 7 T. In order to achieve saturation of the magnetization, higher magnetic fields are required. As shown in the inset of Fig. 6.2(c),

the magnetization data at 2 K displays a weak hysteresis for very small magnetic fields, which suggests competition between FM and AFM interactions in monoclinic $Na_2Co_2TeO_6$. This is consistent with the observed positive Θ_{CW} and the non-vanishing $\chi(T)$ at $T < T_N$. A competition between FM and AFM correlations, i.e., having an AFM transition despite a positive Θ_{CW}, is generally considered evidence of magnetic frustration which is essential in achieving a QSL phase [65]. Similar behavior, a positive CW temperature and a weak hysteresis, was reported for a polycrystalline sample of $Na_2Co_2SbO_6$ formed in space group $C2/m$ [146].

6.5 Sample Quality

The monoclinic $Na_2Co_2TeO_6$ compound is very sensitive to the synthesis conditions. Adding more excess of Na_2CO_3 precursor or lowering the synthesis temperature can change the inter-layer Na content in the resulting compound. Figure 6.3(a) shows the x-ray patterns for two different $Na_2Co_2TeO_6$ samples with different Na content. S1 is the same quality as the data used in this chapter and S2 refers to a sample with more inter-layer Na atoms and Co deficiencies in the honeycomb layers. The x-ray pattern of S2 shows a shift in the first peak to the right compared to the first peak in the S1 pattern, this difference is due to a small decrease in the inter-layer spacing of S2 due to stronger connections between the honeycomb layers (more inter-layer Na atoms). An increase in the inter-layer Na content happens at the cost of the Co deficiencies in the honeycomb layers due to the charge neutrality condition in the compound. The Co deficiency in S2 enhances the a and b lattice parameters due to a break in the chain of honeycomb networks of Co atoms compared to S1, and as expected we observe a shift to the left in the first two honeycomb peaks. We also compare the magnetic susceptibility as a function of temperature between both S1 and S2 samples. The S2 sample shows a peak in the $d\chi/dT$ at 5.9 K, lower than what is reported for S1 ($T_N =$

Table 6.3: A comparison between the lattice parameters of S1 and S2 samples.

Sample Name	a $(\mathring{A})$	b $(\mathring{A})$	c $(\mathring{A})$	β (deg.)
S1	5.33225(6)	9.20808(8)	5.80718(8)	108.90837(88)
S2	5.35919(4)	9.24795(7)	5.77787(6)	108.92163(60)

9.6 K). Sample S2 also displays an additional upturn at 3 K. Table 6.3 compares the lattice parameters between S1 and S2 samples.

Sample S2 can be a good candidate to study the effect of random vacancies on the Kitaev spin-liquid physics without the adverse effect of stacking faults. Also, the more localized magnetic d orbitals in $Na_2Co_2TeO_6$ make it an ideal system in which to study the role of magnetic vacancies when only nearest-neighbor interactions are present. In $5d$ systems such as iridates, the next-nearest neighbor interactions cannot be neglected, and those interactions often prefer AFM order over the QSL phase [116, 153].

6.6   Heat Capacity

Analyzing the magnetic heat capacity and entropy is helpful in determining the ground-state of an ordered system. As shown in Fig. 6.4(a), the heat capacity has a sharp peak at 12 K, consistent with the magnetic susceptibility data. The inset of Fig. 6.4(a) shows the derivative of the heat capacity as a function of temperature. As was observed for $d\chi/dT$, the AFM peak in the dC/dT curve occurs at 9.1 K and confirms that T_N = 9.6 K in the monoclinic $Na_2Co_2TeO_6$. This 9.6 K AFM peak in the monoclinic structure is at a lower temperature compared to the hexagonal structure, which orders at T_N = 27 K and indicates a stronger magnetic frustration in the monoclinic compound [154].

To isolate the magnetic portion of the heat capacity in monoclinic $Na_2Co_2TeO_6$, we synthesized its non-magnetic analog in the same crystal structure, mono-clinic $Na_2Zn_2TeO_6$, whose measured heat capacity is shown as the black data in
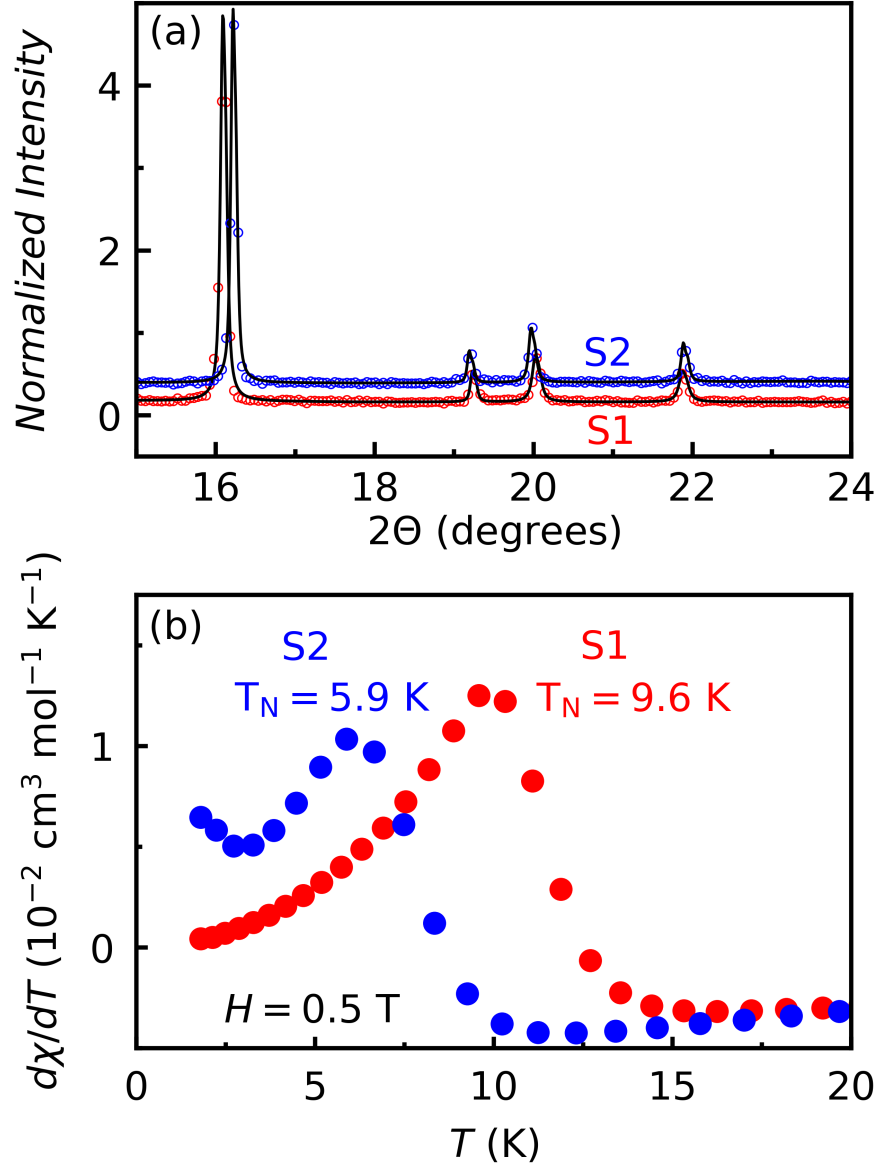
Figure 6.3: (a) A comparison between the x-ray patterns of sample S1 (a high-quality sample) and S2 (Co deficient due to an increase in the inter-layer Na content). (b) The effect of sample quality on the magnetic susceptibility and, accordingly, the transition temperature.
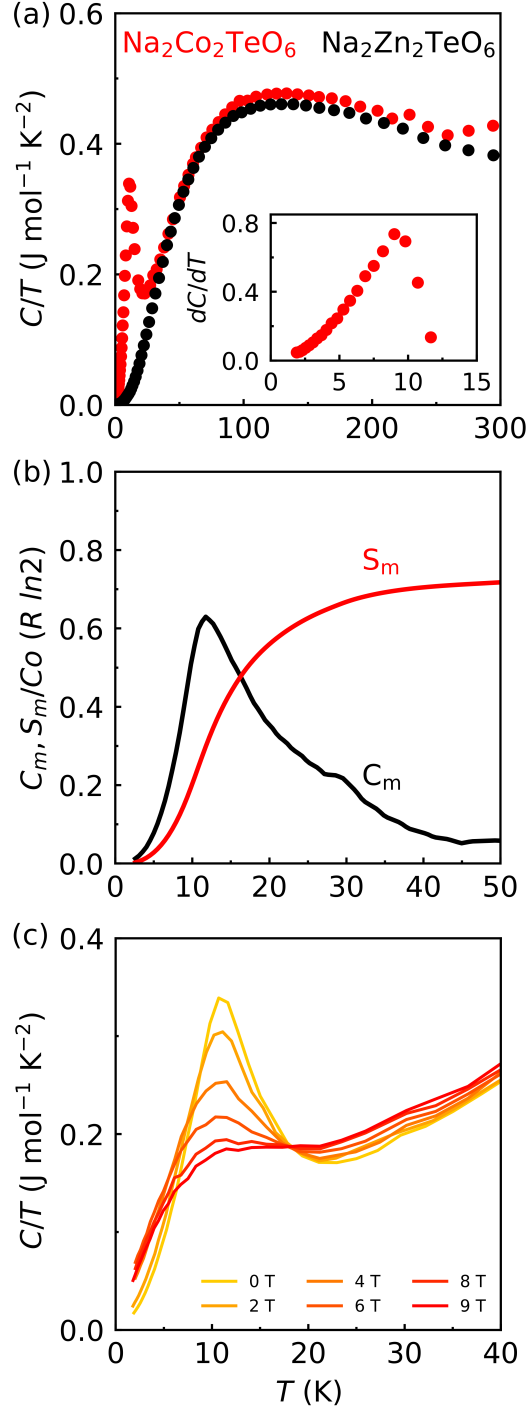
Figure 6.4: (a) The measured heat capacity divided by temperature per mole Co or Zn is plotted as a function of temperature for monoclinic $Na_2Co_2TeO_6$ and $Na_2Zn_2TeO_6$ (lattice contribution). The black data is multiplied by a factor of 0.9 to include the mass correction. Inset shows the derivative of heat capacity as a function of temperature to identify T_N. (b) The magnetic heat capacity (C_m) and magnetic entropy (S_m) of monoclinic $Na_2Co_2TeO_6$ as a function of temperature are shown in units of $R\ln(2)$. (c) Heat capacity (C/T) per mole Co atom as a function of temperature is plotted up to 9 T for $T < 40$ K. The T_N peak is not completely suppressed by increasing the magnetic field in monoclinic $Na_2Co_2TeO_6$.

Table 6.4: Magnetic and thermodynamic properties of $Na_2Co_2SbO_6$, hexagonal and monoclinic polymorphs of $Na_2Co_2TeO_6$.

Material	Structure	T_N (K)	Θ_{CW} (K)	μ_{eff} $(\frac{\mu_B}{mol})$	S_m/Co	Ref.
$Na_2Co_2SbO_6$	$C2/m$	8.3	+2.2	5.22	1.47 $R\ln(2)$	[65]
$Na_2Co_2TeO_6$	$P6_322$	27	−8.3	5.34	0.70 $R\ln(2)$	[65, 151]
$Na_2Co_2TeO_6$	$C2/m$	9.6	+10.28	4.83	0.70 $R\ln(2)$	this work

Fig. 6.4(a). We subtracted the phonon contribution (C/T of monoclinic $Na_2Zn_2TeO_6$) from the total heat capacity of monoclinic $Na_2Co_2TeO_6$ and obtained the magnetic heat capacity for the monoclinic structure, which is plotted in units of $R\ln(2)$ per mole Co in Fig. 6.4(b) (black data). The T_N is clearly resolved in the C_m/T curve. The small change in the slope of the C_m/T curve at 30 K might be due to a small amount of impurity from hexagonal compound inclusions. We also calculated the magnetic entropy by integrating the C_m/T curve as a function of temperature, $S_m = \int (C_m/T)dT$. The calculated magnetic entropy reaches 70% of the expected molar value $R\ln(2)$ per Co atom at 50 K . The molar entropy is expected to be $R\ln(2)$ if the magnetic ground state constitutes pseudo-spin 1/2 degrees of freedom, as theoretically suggested for the Co^{2+} ions ($3d^7$) in the high-spin state with a Γ_7 doublet ground-state [155]. Releasing 70% of this amount across the AFM transition indicates considerable fluctuations of the pseudo-spin 1/2 degrees of freedom due to magnetic frustration. Table 6.4 compares the magnetic and thermodynamic properties of monoclinic $Na_2Co_2TeO_6$ with its predecessors $Na_2Co_2SbO_6$ and hexagonal $Na_2Co_2TeO_6$.

The measured C/T as a function of temperature under applied magnetic field is presented in Fig. 6.4(c). The heat capacity divided by temperature shows similar behavior to the magnetic susceptibility and displays a suppression of the AFM peak with increasing field. However, in contrast to the complete change of behavior seen in χ at 6.5 T, the C/T data still shows a residual peak up to 9 T. Only having access to the χ as a function of temperature measured up to 6.5 T, one can say

the system is in a magnetically disordered state due a complete suppression of the T_N peak. Meanwhile, the measured C/T as a function of temperature shows a residual T_N peak even at 9 T, which suggests that to suppress the T_N peak in the heat capacity a higher field is required. Similar suppression of the AFM peak has been reported for hexagonal $Na_2Co_2TeO_6$ [66, 154].

6.7 Conclusion

The results we have presented here revealed the interesting interplay of structural symmetry and magnetic properties in the $Na_2Co_2TeO_6$ polymorphs. Although both polymorphs possess identical Co-Te honeycomb layers, the magnetic properties of monoclinic $Na_2Co_2TeO_6$ are markedly more similar to the isostructural $Na_2Co_2SbO_6$ in space group $C2/m$ than to its hexagonal polymorph in space group $P6_322$. Both monoclinic $Na_2Co_2TeO_6$ and $Na_2Co_2SbO_6$ have a positive CW temperature and a single AFM transition with evidence of anisotropic interactions and magnetic frustration. These results make a strong case for the crucial role of lattice symmetry in the ongoing search for an ideal Kitaev system.

CHAPTER VII

Challenges of Topo-Tactic Exchange Synthesis

Topo-tactic exchange synthesis is a powerful method to locally and partially modify the structural properties of a material. This method is specifically helpful in the case of Kitaev materials since it affords the possibility of keeping the honeycomb structures intact while the inter-layer chemistry, or sometimes even the intra-layer alkali metal, in the honeycomb layers can be modified. In chapter III, I showed how changing the inter-layer atoms and their coordination can lower the transition temperature in the exchange system. The inter-layer Li atoms in the parent compound α-Li$_2$IrO$_3$ are octahedrally coordinated and make a strong connection between the layers. I was able to change the inter-layer connections with linearly coordinated Ag atoms in Ag$_3$LiIr$_2$O$_6$ via a topo-tactic method. These partial changes in the structural properties of the parent compound led to a reduction in the transition temperature and therefore its proximity to the Kitaev phase.

As discussed earlier in chapter III and IV, the topo-tactic synthesis method can enhance the structural disorder in the compound, and in severe cases can even hide the signatures of long-range order in experimental measurements thus leading to misinterpretation of the data. Figure 4.1 presents the x-ray patterns of both parent compound α-Li$_2$IrO$_3$ and exchange system Ag$_3$LiIr$_2$O$_6$. The peaks in the

range of 19° to 24° provide information about the quality of honeycomb ordering in a sample. The honeycomb peaks for the parent compound are sharp and well-separated which is evidence for less structural disorder, while the honeycomb peaks in the Ag-exchange systems are all merged and form an asymmetric broad peak due to higher levels of stacking fault disorder. We also confirmed our results via TEM measurement of both samples, Fig. 3.14. Due to a weaker inter-layer O-Ag-O connection between the honeycomb layers, the Ag-exchange compound is prone to suffer from more stacking faults compared to its parent compound. In chapter IV, I also showed that the topo-tactic method can create rows of unwanted atoms by breaking the weak honeycomb networks when using a lower-quality parent compound, and that this type of disorder can hide the signs of long-range ordering in the system and lead to misinterpretation of the data.

Here, I present another challenge of using the topo-tactic exchange method for modifying the honeycomb layered systems. One of the candidate elements to replace the alkali metals in the first-generation of Kitaev materials is Cu. Cu atoms can have different oxidation states in a compound, and overall charge neutrality in the compound forces the magnetic element to have a mixed valency as well. The mixed valency of the magnetic element produces a new type of disorder in the system which is not in favor of Kitaev physics.

7.1 Second Example of a Complete Exchange Material

I was able to successfully prepare another complete exchange material, Cu_2RhO_3, via topo-tactic reaction. I used the parent compound Li_2RhO_3 and CuCl (halide compound) as precursors for synthesizing Cu_2RhO_3. A high-quality Li_2RhO_3 sample was mixed with CuCl according to

$$Li_2RhO_3 + 2\,CuCl \rightarrow Cu_2RhO_3 + 2\,LiCl \tag{7.1}$$

141
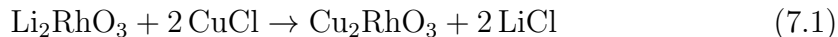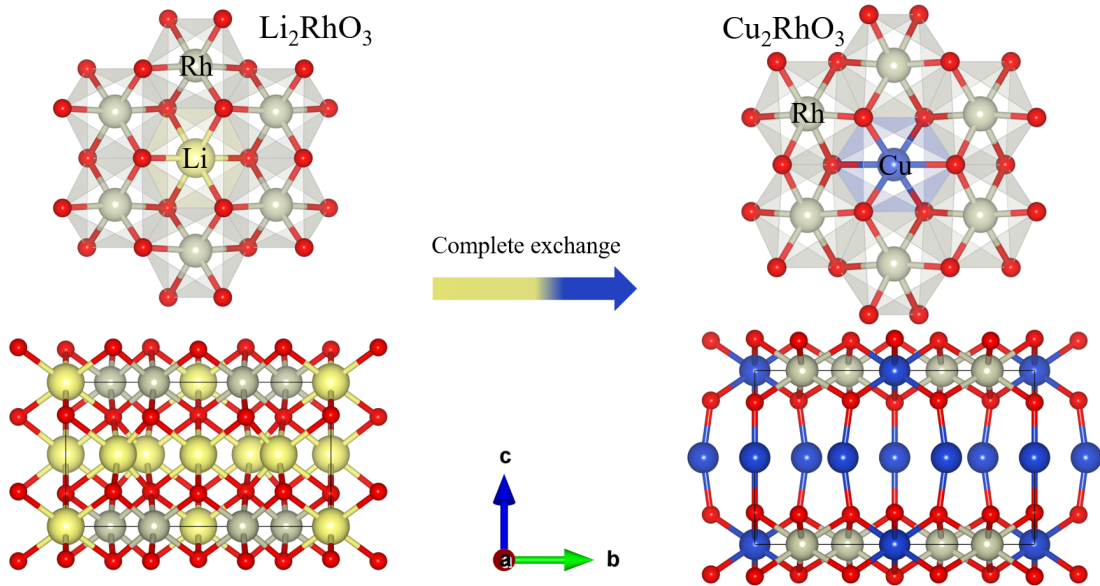
Figure 7.1: Left: The honeycomb network in parent compound Li_2RhO_3 with a Li atom at the center. The inter-layer connections between the honeycomb layers in the parent compound are in an octahedral coordination. Right: The intra-layer and inter-layer alkali atoms are replaced by Cu atoms in Cu_2RhO_3. The inter-layer connections in the exchanged compound are linearly coordinated O-Cu-O bonds.

with excess of CuCl and heated to 400 °C under mild conditions to synthesize Cu_2RhO_3. Figure 7.1 compares the crystal structures of both parent compound and the exchange system. Both intra-layer and inter-layer Li atoms are replaced by Cu atoms in Cu_2RhO_3. The inter-layer Li atoms are octahedrally coordinated and connected to three O atoms on top and three O atoms on the bottom. Meanwhile, the inter-layer connections between the honeycomb layers in Cu_2RhO_3 are weaker and in a dumbbell coordination (O-Cu-O).

7.2   Rietveld Refinement Analysis

Figure 7.2 presents the PXRD pattern of a high-quality sample of Cu_2RhO_3. All the Bragg peaks are well indexed in space group $C2/m$, specifically the characteristic peaks for the honeycomb ordering structure in the range of 19° to 26°. This asymmetric broad peak is barely visible in the x-ray pattern due to more

Table 7.1: Unit cell and Rietveld refinement quality factors for Cu_2RhO_3 from PXRD Rietveld refinement analysis.

Unit cell parameters		Refinement parameters	
Space Group	$C2/m$	Parameters	23
a (Å)	5.29451(6)	R_{Bragg} (%)	6.03
b (Å)	9.15922(10)	R_F (%)	5.32
c (Å)	5.95420(6)	R_{exp} (%)	3.15
β (°)	107.11320(132)	R_p (%)	3.67
V (Å^3)	275.957	R_{wp} (%)	4.97
Z	2	χ^2	2.49
ρ (gr cm^{-3})	6.665	T (K)	295

stacking fault disorder in the system. A similar observation was also reported for the isostructural Ru-based compound [156]. To have a better understanding of the crystal structure of the Cu_2RhO_3 system, I calculated the bond-angle variance (σ) for Cu_2RhO_3, finding a σ value of 8.7°. The σ value for Cu_2RhO_3 is significantly larger than what is observed in parent compound Li_2RhO_3 (3.1°), and large even compared to $Ag_3LiRh_2O_6$ (6.1°) which is partially modified. This increase in the bond-angle variance might be due to more distorted intra-layer Cu atoms at the center of the honeycomb networks. Cu atoms can be in oxidation states of +1 and +2 and the larger distortion may be due to the presence of Cu^{2+} in the honeycomb layers. The summary of the Rietveld refinement of Cu_2RhO_3 such as lattice parameter, R-factors, Wyckoff site occupancies, and Debye-Waller factors are presented in Table 7.1 and 7.2. PXRD measurements were performed using a Bruker D8 ECO instrument with Cu-K_α x-ray source at room temperature. The FullProf suite and VESTA software were used for the Rietveld refinements and crystal visualizations [76, 81].
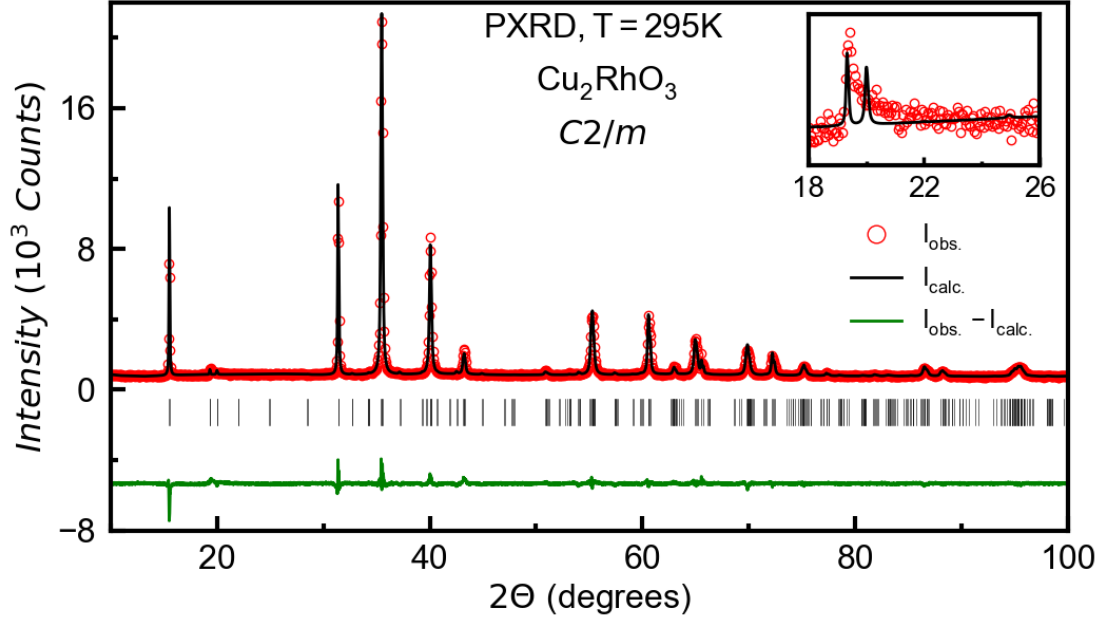
Figure 7.2: The x-ray diffraction pattern of Cu_2RhO_3 (red open circles) and Rietveld refinement analysis using $C2/m$ model (black solid line) are presented. The inset shows the honeycomb ordering peaks in the range of 19° to 26°. This asymmetric broad peak is barely visible which indicates a higher level of stacking faults in the sample.

Table 7.2: Atomic coordinates, site occupancies, and the isotropic Debye-Waller factors for the Rietveld refinement of Cu_2RhO_3 from PXRD Rietveld refinement analysis.

atom	site	x	y	z	occ.	B_{iso} (Å^2)
Rh1	$4g$	0	0.16903(25)	0	0.748	0.42
Cu1	$4g$	0	0.16903(25)	0	0.246	0.42
Rh2	$2b$	0	1/2	0	0.488	0.46
Cu2	$2b$	0	1/2	0	0.500	0.46
Cu3	$4h$	0	0.31506(37)	1/2	1.000	0.53
Cu4	$2c$	0	0	1/2	1.000	0.53
O1	$8j$	0.88100	0.34300	0.17200	1.000	0.55
O2	$4i$	0.91600	0	0.18300	1.000	0.55
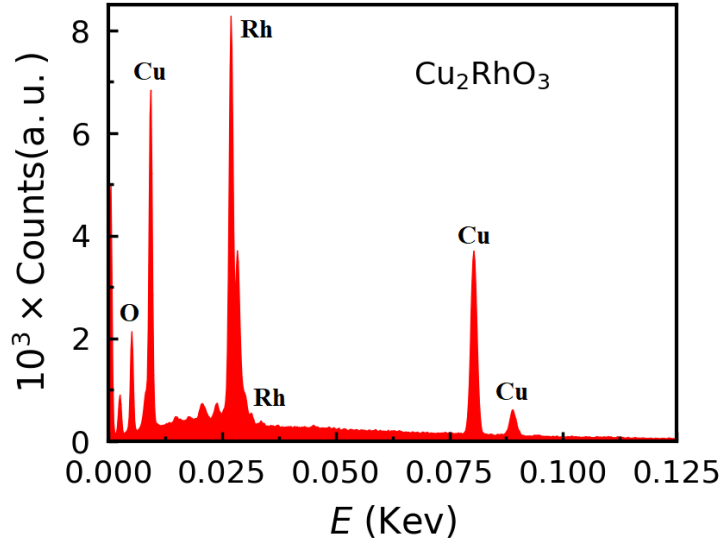
Figure 7.3: EDX spectrum from a pressed pellet of Cu_2RhO_3.

Table 7.3: EDX measurement results on a pressed pellet sample of Cu_2RhO_3, the results obtained from EDX suggest the chemical formula $Cu_{2.005}Rh_{0.994}O_3$.

Atoms	atomic %	atomic %	atomic %	average
Cu	36.7	35.6	36.6	36.3
Rh	18	18	18	18
O	45.3	46.5	45.4	45.7333

7.3 Energy Dispersive X-ray Spectroscopy

We performed energy dispersive x-ray spectroscopy to confirm the chemical composition of the newly synthesized honeycomb Rh compound, Cu_2RhO_3.[1] Figure 7.3 and Table 7.3 present the results of EDX measurements. The obtained chemical formula from the EDX measurement, $Cu_{2.005}Rh_{0.994}O_3$ is in excellent agreement with the results of our x-ray diffraction analysis and we can confirm that Cu_2RhO_3 is the second example of a complete exchange system after Cu_2IrO_3 [55].

---

[1]The EDX measurement has been done by Xiaohan Yao.

145

7.4 X-ray Absorption Spectroscopy

As discussed earlier, Cu atoms tends to be in oxidation states of 1+ or 2+. Cu^{1+} is non-magnetic and forms in a linear or dumbbell coordination, while Cu^{2+} is magnetic with S = 1/2 and it has a square planar form in a compound. For the purpose of Kitaev physics, it is necessary to keep the oxidation state of Rh ions at 4+ to retain the $J_{eff} = \frac{1}{2}$ state in Cu_2RhO_3, similar to its parent compound. However, having a mixed valency in the Cu atoms will force the Rh atoms to have mixed valency as well. Previously in Cu_2IrO_3 [108], it was reported that this compound suffers from a mixed valency of Cu^{1+}/Cu^{2+} and therefore Ir^{4+}/Ir^{3+}. However, we believe the mixed valency in the Cu_2RhO_3 is more severe due to two reasons: barely visible honeycomb ordering peaks in the PXRD pattern, and a large value for the calculated bond-angle variance. The XAS measurement is a powerful technique for determining the oxidation states of elements in a material. We performed XAS measurements on a high-quality Cu_2RhO_3 sample as well as its references, Li_2RhO_3 (Rh^{4+}) and $NaRhO_2$ (Rh^{3+}).[2] Figure 7.4 (a) shows the XAS data of all three Rh compounds for the Rh L_3 edge. The Rh L_3 edge in Li_2RhO_3 shows a shoulder which is a signature for holes in t_{2g} levels and this shoulder is absent in both Cu_2RhO_3 and $NaRhO_2$. The difference between the peak positions of Cu_2RhO_3-Li_2RhO_3 and Cu_2RhO_3-$NaRhO_2$ is 1.22 eV and 0.13 eV, respectively. The absence of the shoulder and proximity of the Rh L_3 edge of Cu_2RhO_3 to the peak for $NaRhO_2$ suggest a large portion of the Rh ions are in an oxidation state of 3+, which is a non-magnetic element. From the XAS data of both Li_2RhO_3 and $NaRhO_2$, we tried to model the XAS data of Cu_2RhO_3 in Figure 7.4(b). According to our model based on the experimental work, we believe about 40% of Rh ions are in the oxidation state of 4+ and the rest are in the oxidation state of 3+. The mixed valency in the oxidation state of Rh ions confirms the presence of mixed

---

[2]The XAS measurements were performed by Dr. D. Haskel at Argonne National Lab.
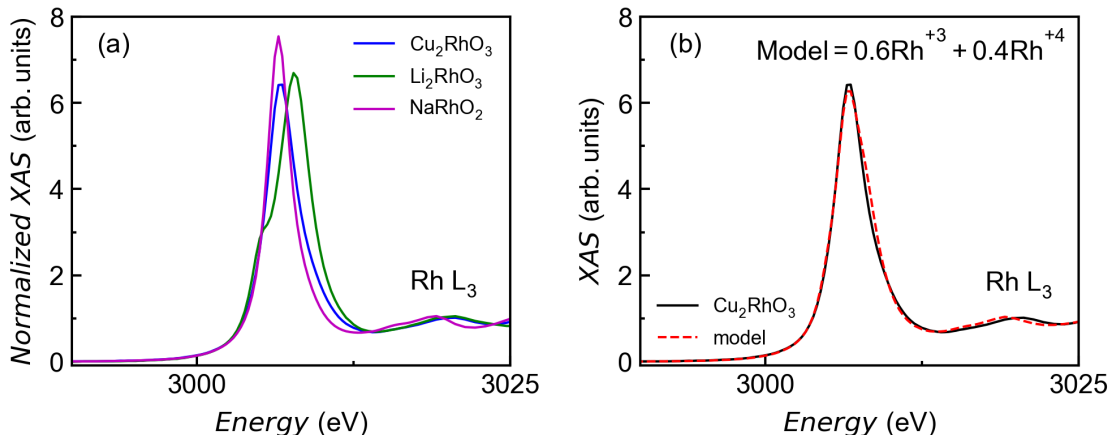
Figure 7.4: (a) We present the results of XAS measurements on Cu_2RhO_3, Li_2RhO_3, and $NaRhO_2$. Li_2RhO_3 and $NaRhO_2$ are used as a reference for Rh^{4+} and Rh^{3+}, respectively. (b) Using Li_2RhO_3 and $NaRhO_2$ XAS results to generate a model for Cu_2RhO_3 to estimate the oxidation state of Rh ions in the honeycomb layers.

valency in the oxidation state of Cu ions as well. We believe all the Cu^{2+} ions are located in the honeycomb layers and their coordination in the compound is the main source of a significant increase in the trigonal distortion in the compound.

7.5 Conclusion

In this chapter, I discussed one of the challenges of the topo-tactic synthesis method. This method is a powerful synthesis technique to partially modify the crystal structure of a compound. However, it is also important to understand the challenges and problems that this technique can cause. In earlier chapters, I discussed the increase in stacking fault disorder in the second-generation compounds, as well as an example of having rows of unwanted atoms in a product compound when using a weak honeycomb-ordering parent compound. Here, I introduced a second example of a complete exchange system which faces a severe level of mixed valency of Rh^{4+}/Rh^{3+} as well as Cu^{1+}/Cu^{2+}. The only examples of complete exchange materials are reported for the Cu-exchange systems Cu_2RhO_3 and

Cu$_2$IrO$_3$. Both compounds suffer from a mixed valency of Cu^{1+}/Cu^{2+}; however, this problem is more pronounced in the case of Cu$_2$RhO$_3$.

CHAPTER VIII

Conclusion

In this dissertation I discussed my experimental studies of the physics related to Kitaev materials from different viewpoints and provided a few examples of important material characteristics in favor of Kitaev interactions. In chapter III, I introduced a new Kitaev candidate material, $Ag_3LiIr_2O_6$. This compound is produced by modification of the inter-layer chemistry in the parent compound α-Li_2IrO_3 via a topo-chemical method. The replacement of light, octahedrally coordinated inter-layer Li atoms in α-Li_2IrO_3 by heavy, linearly coordinated inter-layer Ag atoms increases the inter-layer spacing as well as the effect of SOC in the honeycomb layers. The results of the structural modifications in the product compound lead to a reduction in the long-range ordering temperature compared to the parent compound, which puts $Ag_3LiIr_2O_6$ in closer proximity to the Kitaev limit.

In chapter V I presented the first experimental observation of tuning the low-energy physics of a honeycomb compound from the Kitaev to the Ising limit. It has been theoretically predicted that the physics of Kitaev materials is more diverse beyond what has been studied thus far, and this work represented a first glimpse of this diversity. I was able to introduce a honeycomb-layered compound, $Ag_3LiRh_2O_6$, via modification of the inter-layer connections between the

honeycomb-layered Kitaev material Li_2RhO_3. The structural modification of the parent compound increased the trigonal distortion around the octahedral environment of the Rh atoms in the product system. The combination of trigonal distortion in the presence of weaker SOC led to a change of the spin-orbital state from the $J_{eff} = \frac{1}{2}$ state, which drives Kitaev interactions in Li_2RhO_3, to a novel $\mu = \frac{1}{2}$ state that drives Ising interactions in $Ag_3LiRh_2O_6$. The change in the spin-orbital state of $Ag_3LiIr_2O_6$ is accompanied by a dramatic change of magnetism: a robust AFM ordering transition at 94 K which is one order of magnitude larger than all the other studied Kitaev candidates.

In chapter VI I introduced a new high-spin configuration of $3d^7$ Kitaev candidate material synthesized with transition metal Co^{2+}. The new Kitaev candidate material is another polymorph of hexagonal $Na_2Co_2TeO_6$, which is crystallized in space group $C2/m$, the so-called monoclinic $Na_2Co_2TeO_6$. The monoclinic $Na_2Co_2TeO_6$ shows an AFM ordering peak at 9.6 K, different from the three AFM ordering temperatures at 27, 15, and 7 K in hexagonal $Na_2Co_2TeO_6$. The change in the crystal summery of the $Na_2Co_2TeO_6$ compound from space group $P6_322$ to space group $C2/m$ significantly modifies the thermodynamic properties of the monoclinic system, leading to a reduction in the transition temperature as well as the number of anomalies. I also showed that the thermodynamic properties of monoclinic $Na_2Co_2TeO_6$ are very close to what is reported for its isostructural compound $Na_2Co_2SbO_6$. This is an important finding regarding the importance of crystal symmetry to Kitaev candidates.

In addition to the important material characteristics in favor of Kitaev physics, such as enhancement of SOC, modification of the spin-orbital state, and crystal symmetry, I also studied the challenges and problems that a topo-tactic exchange reaction can produce in the product systems. In chapter IV, I reviewed how the quality of the parent compound used for the exchange reaction can have a direct

role in the overall level of disorder in the product compound. An enhancement in the level of stacking fault disorder in the second-generation of Kitaev materials which are synthesized via a topo-tactic reaction is inevitable; however, a parent compound with a weak honeycomb structure can cause new type of disorders such as unwanted rows of atoms in the honeycomb layers. This type of disorder can conceal the signatures of long-range ordering in the system and lead to misinterpretation of experimental data. Later in chapter VII, I introduced a second example of a complete exchange compound, Cu_2RhO_3. I showed how the mixed valency in the oxidation state of Cu^{1+}/Cu^{2+} can cause mixed valency in the magnetic element Rh^{4+}/Rh^{3+}, where the Rh^{3+} is a non-magnetic element and the presence of a large number of them in the honeycomb layers produces a new type of disorder in the system which disfavors Kitaev physics.

To establish and design a method to synthesize an ideal Kitaev material that can satisfy all the required criteria of the Kitaev model, it is crucial to gather all the important features in favor of Kitaev physics, as well as to understand the experimental challenges in the techniques used for synthesizing these materials. Eventually, this can pave the way towards realizing an ideal Kitaev material.

BIBLIOGRAPHY

[1] J. Knolle and R. Moessner, "A Field Guide to Spin Liquids", Annual Review of Condensed Matter Physics **10**, 451–472 (2019).

[2] L. Balents, "Spin liquids in frustrated magnets", Nature **464**, 199–208 (2010).

[3] L. Savary and L. Balents, "Quantum spin liquids: a review", Reports on Progress in Physics **80**, 016502 (2016).

[4] C. Broholm, R. J. Cava, S. A. Kivelson, D. G. Nocera, M. R. Norman, and T. Senthil, "Quantum spin liquids", Science **367**, eaay0668 (2020).

[5] Y. Zhou, K. Kanoda, and T.-K. Ng, "Quantum spin liquid states", Rev. Mod. Phys. **89**, 025003 (2017).

[6] C. Nayak, S. H. Simon, A. Stern, M. Freedman, and S. Das Sarma, "Non-Abelian anyons and topological quantum computation", Rev. Mod. Phys. **80**, 1083–1159 (2008).

[7] M. A. Nielsen and I. Chuang, *Quantum computation and quantum information*, 2002.

[8] P. Anderson, "Resonating valence bonds: A new kind of insulator?", Materials Research Bulletin **8**, 153–160 (1973).

[9] P. Fazekas and P. W. Anderson, "On the ground state properties of the anisotropic triangular antiferromagnet", The Philosophical Magazine: A Journal of Theoretical Experimental and Applied Physics **30**, 423–440 (1974).

[10] N. Y. Yao, M. P. Zaletel, D. M. Stamper-Kurn, and A. Vishwanath, "A quantum dipolar spin liquid", Nature Physics **14**, 405–410 (2018).

[11] Y. Shimizu, K. Miyagawa, K. Kanoda, M. Maesato, and G. Saito, "Spin Liquid State in an Organic Mott Insulator with a Triangular Lattice", Phys. Rev. Lett. **91**, 107001 (2003).

[12] T. Itou, A. Oyamada, S. Maegawa, M. Tamura, and R. Kato, "Quantum spin liquid in the spin-1/2 triangular antiferromagnet $EtMe_3Sb[Pd(dmit)_2]_2$", Phys. Rev. B **77**, 104413 (2008).

[13] L. Ding, P. Manuel, S. Bachus, F. Grußler, P. Gegenwart, J. Singleton, R. D. Johnson, H. C. Walker, D. T. Adroja, A. D. Hillier, and A. A. Tsirlin, "Gapless spin-liquid state in the structurally disorder-free triangular antiferromagnet $NaYbO_2$", Phys. Rev. B **100**, 144432 (2019).

[14] M. M. Bordelon, E. Kenney, C. Liu, T. Hogan, L. Posthuma, M. Kavand, Y. Lyu, M. Sherwin, N. P. Butch, C. Brown, et al., "Field-tunable quantum disordered ground state in the triangular-lattice antiferromagnet NaYbO2", Nature Physics **15**, 1058–1064 (2019).

[15] S. Sachdev, "Kagomé- and triangular-lattice Heisenberg antiferromagnets: Ordering from quantum fluctuations and quantum-disordered ground states with unconfined bosonic spinons", Phys. Rev. B **45**, 12377–12396 (1992).

[16] J. S. Helton, K. Matan, M. P. Shores, E. A. Nytko, B. M. Bartlett, Y. Yoshida, Y. Takano, A. Suslov, Y. Qiu, J.-H. Chung, D. G. Nocera, and Y. S. Lee, "Spin Dynamics of the Spin-1/2 Kagome Lattice Antiferromagnet $ZnCu_3(OH)_6Cl_2$", Phys. Rev. Lett. **98**, 107204 (2007).

[17] T.-H. Han, J. S. Helton, S. Chu, D. G. Nocera, J. A. Rodriguez-Rivera, C. Broholm, and Y. S. Lee, "Fractionalized excitations in the spin-liquid state of a kagome-lattice antiferromagnet", Nature **492**, 406–410 (2012).

[18] Y. Okamoto, M. Nohara, H. Aruga-Katori, and H. Takagi, "Spin-Liquid State in the $S = 1/2$ Hyperkagome Antiferromagnet $Na_4Ir_3O_8$", Phys. Rev. Lett. **99**, 137207 (2007).

[19] R. Dally, T. Hogan, A. Amato, H. Luetkens, C. Baines, J. Rodriguez-Rivera, M. J. Graf, and S. D. Wilson, "Short-Range Correlations in the Magnetic Ground State of $Na_4Ir_3O_8$", Phys. Rev. Lett. **113**, 247601 (2014).

[20] A. Kitaev, "Anyons in an exactly solved model and beyond", Annals of Physics, January Special Issue **321**, 2–111 (2006).

[21] G. Jackeli and G. Khaliullin, "Mott Insulators in the Strong Spin-Orbit Coupling Limit: From Heisenberg to a Quantum Compass and Kitaev Models", Physical Review Letters **102**, 017205 (2009).

[22] Y. Motome and J. Nasu, "Hunting Majorana fermions in Kitaev magnets", Journal of the Physical Society of Japan **89**, 012002 (2020).

[23] H. Takagi, T. Takayama, G. Jackeli, G. Khaliullin, and S. E. Nagler, "Concept and realization of Kitaev quantum spin liquids", Nature Reviews Physics **1**, 264–280 (2019).

[24] S. M. Winter, A. A. Tsirlin, M. Daghofer, J. van den Brink, Y. Singh, P. Gegenwart, and R. Valentí, "Models and materials for generalized Kitaev magnetism", Journal of Physics: Condensed Matter **29**, 493002 (2017).

[25] J. Knolle, *Dynamics of a Quantum Spin Liquid* (Springer, 2016).

[26] Z. Nussinov and J. van den Brink, "Compass models: Theory and physical motivations", Rev. Mod. Phys. **87**, 1–59 (2015).

[27] J. Zaanen, G. A. Sawatzky, and J. W. Allen, "Band gaps and electronic structure of transition-metal compounds", Phys. Rev. Lett. **55**, 418–421 (1985).

[28] G. Khaliullin, "Orbital order and fluctuations in Mott insulators", Progress of Theoretical Physics Supplement **160**, 155–202 (2005).

[29] W. Witczak-Krempa, G. Chen, Y. B. Kim, and L. Balents, "Correlated Quantum Phenomena in the Strong Spin-Orbit Regime", Annual Review of Condensed Matter Physics **5**, 57–82 (2014).

[30] H. Liu, J. Chaloupka, and G. Khaliullin, "Kitaev Spin Liquid in $3d$ Transition Metal Compounds", Phys. Rev. Lett. **125**, 047201 (2020).

[31] H. Liu and G. Khaliullin, "Pseudospin exchange interactions in d^7 cobalt compounds: Possible realization of the Kitaev model", Phys. Rev. B **97**, 014407 (2018).

[32] R. Sano, Y. Kato, and Y. Motome, "Kitaev-Heisenberg Hamiltonian for high-spin d^7 Mott insulators", Phys. Rev. B **97**, 014408 (2018).

[33] F. Bahrami, X. Hu, Y. Du, O. I. Lebedev, C. Wang, H. Luetkens, G. Fabbris, M. J. Graf, D. Haskel, Y. Ran, and F. Tafti, "First demonstration of tuning between the Kitaev and Ising limits in a honeycomb lattice", Science Advances **8**, eabl5671 (2022).

[34] M. J. O'Malley, H. Verweij, and P. M. Woodward, "Structure and properties of ordered Li2IrO3 and Li2PtO3", Journal of Solid State Chemistry **181**, 1803–1809 (2008).

[35] Y. Singh, S. Manni, J. Reuther, T. Berlijn, R. Thomale, W. Ku, S. Trebst, and P. Gegenwart, "Relevance of the Heisenberg-Kitaev Model for the Honeycomb Lattice Iridates A_2IrO_3", Phys. Rev. Lett. **108**, 127203 (2012).

[36] K. Mehlawat, A. Thamizhavel, and Y. Singh, "Heat capacity evidence for proximity to the Kitaev quantum spin liquid in A_2IrO_3 (A = Na, Li)", Phys. Rev. B **95**, 144406 (2017).

[37] Y. Singh and P. Gegenwart, "Antiferromagnetic Mott insulating state in single crystals of the honeycomb lattice material Na₂IrO₃", Phys. Rev. B **82**, 064412 (2010).

[38] K. W. Plumb, J. P. Clancy, L. J. Sandilands, V. V. Shankar, Y. F. Hu, K. S. Burch, H.-Y. Kee, and Y.-J. Kim, "$\alpha - RuCl_3$: A spin-orbit assisted Mott insulator on a honeycomb lattice", Phys. Rev. B **90**, 041112 (2014).

[39] S.-H. Do, S.-Y. Park, J. Yoshitake, J. Nasu, Y. Motome, Y. S. Kwon, D. Adroja, D. Voneshen, K. Kim, T.-H. Jang, et al., "Majorana fermions in the Kitaev quantum spin system α-RuCl3", Nature Physics **13**, 1079–1084 (2017).

[40] Y. Luo, C. Cao, B. Si, Y. Li, J. Bao, H. Guo, X. Yang, C. Shen, C. Feng, J. Dai, G. Cao, and Z.-A. Xu, "Li₂RhO₃: A spin-glassy relativistic Mott insulator", Phys. Rev. B **87**, 161121 (2013).

[41] P. Khuntia, S. Manni, F. R. Foronda, T. Lancaster, S. J. Blundell, P. Gegenwart, and M. Baenitz, "Local magnetism and spin dynamics of the frustrated honeycomb rhodate Li₂RhO₃", Phys. Rev. B **96**, 094432 (2017).

[42] M. Majumder, M. Schmidt, H. Rosner, A. A. Tsirlin, H. Yasuoka, and M. Baenitz, "Anisotropic $Ru^{3+}4d^5$ magnetism in the $\alpha - RuCl_3$ honeycomb system: Susceptibility, specific heat, and zero-field NMR", Phys. Rev. B **91**, 180401 (2015).

[43] J. T. Heath, F. Bahrami, S. Lee, R. Movshovich, X. Chen, F. Tafti, and K. S. Bedell, "Signatures of a Majorana-Fermi surface in the Kitaev magnet $Ag_3LiIr_2O_6$", arXiv preprint arXiv:2108.03246 (2021).

[44] F. Bahrami, E. M. Kenney, C. Wang, A. Berlie, O. I. Lebedev, M. J. Graf, and F. Tafti, "Effect of structural disorder on the Kitaev magnet $Ag_3LiIr_2O_6$", Phys. Rev. B **103**, 094427 (2021).

[45] R. D. Johnson, S. C. Williams, A. A. Haghighirad, J. Singleton, V. Zapf, P. Manuel, I. I. Mazin, Y. Li, H. O. Jeschke, R. Valentí, and R. Coldea, "Monoclinic crystal structure of $\alpha-RuCl_3$ and the zigzag antiferromagnetic ground state", Phys. Rev. B **92**, 235119 (2015).

[46] S. K. Choi, R. Coldea, A. N. Kolmogorov, T. Lancaster, I. I. Mazin, S. J. Blundell, P. G. Radaelli, Y. Singh, P. Gegenwart, K. R. Choi, S.-W. Cheong, P. J. Baker, C. Stock, and J. Taylor, "Spin Waves and Revised Crystal Structure of Honeycomb Iridate Na_2IrO_3", Phys. Rev. Lett. **108**, 127204 (2012).

[47] F. Ye, S. Chi, H. Cao, B. C. Chakoumakos, J. A. Fernandez-Baca, R. Custelcean, T. F. Qi, O. B. Korneta, and G. Cao, "Direct evidence of a zigzag spin-chain structure in the honeycomb lattice: A neutron and x-ray diffraction investigation of single-crystal Na_2IrO_3", Phys. Rev. B **85**, 180403 (2012).

[48] H. B. Cao, A. Banerjee, J.-Q. Yan, C. A. Bridges, M. D. Lumsden, D. G. Mandrus, D. A. Tennant, B. C. Chakoumakos, and S. E. Nagler, "Low-temperature crystal and magnetic structure of $\alpha - RuCl_3$", Phys. Rev. B **93**, 134423 (2016).

[49] Y. Haraguchi and H. A. Katori, "Strong antiferromagnetic interaction owing to a large trigonal distortion in the spin-orbit-coupled honeycomb lattice iridate $CdIrO_3$", Phys. Rev. Mater. **4**, 044401 (2020).

[50] S. Choi, S. Manni, J. Singleton, C. V. Topping, T. Lancaster, S. J. Blundell, D. T. Adroja, V. Zapf, P. Gegenwart, and R. Coldea, "Spin dynamics and field-induced magnetic phase transition in the honeycomb Kitaev magnet $\alpha-Li_2IrO_3$", Phys. Rev. B **99**, 054426 (2019).

[51] S. C. Williams, R. D. Johnson, F. Freund, S. Choi, A. Jesche, I. Kimchi, S. Manni, A. Bombardi, P. Manuel, P. Gegenwart, and R. Coldea, "Incommensurate counterrotating magnetic order stabilized by Kitaev interactions in the layered honeycomb $\alpha-Li_2IrO_3$", Phys. Rev. B **93**, 195158 (2016).

[52] F. Freund, S. Williams, R. Johnson, R. Coldea, P. Gegenwart, and A. Jesche, "Single crystal growth from separated educts and its application to lithium transition-metal oxides", Scientific Reports **6**, 1–6 (2016).

[53] J. A. Sears, M. Songvilay, K. W. Plumb, J. P. Clancy, Y. Qiu, Y. Zhao, D. Parshall, and Y.-J. Kim, "Magnetic order in $\alpha - RuCl_3$: A honeycomb-lattice quantum magnet with strong spin-orbit coupling", Phys. Rev. B **91**, 144420 (2015).

[54] S. Widmann, V. Tsurkan, D. A. Prishchenko, V. G. Mazurenko, A. A. Tsirlin, and A. Loidl, "Thermodynamic evidence of fractionalized excitations in $\alpha - RuCl_3$", Phys. Rev. B **99**, 094415 (2019).

[55] M. Abramchuk, C. Ozsoy-Keskinbora, J. W. Krizan, K. R. Metz, D. C. Bell, and F. Tafti, "Cu2IrO3: A New Magnetically Frustrated Honeycomb Iridate", Journal of the American Chemical Society **139**, 15371–15376 (2017).

[56] I. I. Mazin, S. Manni, K. Foyevtsova, H. O. Jeschke, P. Gegenwart, and R. Valentí, "Origin of the insulating state in honeycomb iridates and rhodates", Physical Review B **88**, 035115 (2013).

[57] V. Todorova and M. Jansen, "Synthesis, Structural Characterization and Physical Properties of a New Member of Ternary Lithium Layered Compounds – Li_2RhO_3", Zeitschrift für anorganische und allgemeine Chemie **637**, 37–40 (2011).

[58] A. Banerjee, J. Yan, J. Knolle, C. A. Bridges, M. B. Stone, M. D. Lumsden, D. G. Mandrus, D. A. Tennant, R. Moessner, and S. E. Nagler, "Neutron scattering in the proximate quantum spin liquid α-RuCl_3", Science **356**, 1055–1059 (2017).

[59] F. Bahrami, W. Lafargue-Dit-Hauret, O. I. Lebedev, R. Movshovich, H.-Y. Yang, D. Broido, X. Rocquefelte, and F. Tafti, "Thermodynamic Evidence of Proximity to a Kitaev Spin Liquid in $Ag_3LiIr_2O_6$", Phys. Rev. Lett. **123**, 237203 (2019).

[60] A. de la Torre, B. Zager, F. Bahrami, M. DiScala, J. R. Chamorro, M. H. Upton, G. Fabbris, D. Haskel, D. Casa, T. M. McQueen, F. Tafti, and K. W. Plumb, "Enhanced hybridization in the electronic ground state of the intercalated honeycomb iridate $Ag_3LiIr_2O_6$", Phys. Rev. B **104**, L100416 (2021).

[61] J. Wang, W. Yuan, T. Imai, P. M. Singer, F. Bahrami, and F. Tafti, "NMR investigation on the honeycomb iridate $Ag_3LiIr_2O_6$", Phys. Rev. B **103**, 214405 (2021).

[62] J. Rusnačko, D. Gotfryd, and J. Chaloupka, "Kitaev-like honeycomb magnets: Global phase behavior and emergent effective models", Physical Review B **99**, 064425 (2019).

[63] M. Abramchuk, O. I. Lebedev, O. Hellman, F. Bahrami, N. E. Mordvinova, J. W. Krizan, K. R. Metz, D. Broido, and F. Tafti, "Crystal Chemistry and Phonon Heat Capacity in Quaternary Honeycomb Delafossites: Cu[Li1/3Sn2/3]O2 and Cu[Na1/3Sn2/3]O2", Inorganic Chemistry **57**, 12709–12717 (2018).

[64] F. Bahrami, M. Abramchuk, O. Lebedev, and F. Tafti, "Metastable Kitaev Magnets", Molecules **27**, 871 (2022).

[65] L. Viciu, Q. Huang, E. Morosan, H. Zandbergen, N. Greenbaum, T. McQueen, and R. Cava, "Structure and basic magnetic properties of the honeycomb lattice compounds Na2Co2TeO6 and Na3Co2SbO6", Journal of Solid State Chemistry **180**, 1060–1067 (2007).

[66] G. Lin, J. Jeong, C. Kim, Y. Wang, Q. Huang, T. Masuda, S. Asai, S. Itoh, G. Günther, M. Russina, et al., "Field-induced quantum spin disordered state in spin-1/2 honeycomb magnet Na2Co2TeO6", Nature communications **12**, 5559 (2021).

[67] A. K. Bera, S. M. Yusuf, A. Kumar, and C. Ritter, "Zigzag antiferromagnetic ground state with anisotropic correlation lengths in the quasi-two-dimensional honeycomb lattice compound $Na_2Co_2TeO_6$", Phys. Rev. B **95**, 094424 (2017).

[68] C. Kim, J. Jeong, G. Lin, P. Park, T. Masuda, S. Asai, S. Itoh, H.-S. Kim, H. Zhou, J. Ma, and J.-G. Park, "Antiferromagnetic Kitaev interaction in $J_{eff} = 1/2$ cobalt honeycomb materials $Na_3Co_2SbO_6$ and $Na_2Co_2TeO_6$", J. Phys.: Condens. Matter **34**, 045802 (2021).

[69] A. Bera and S. Yusuf, "Magnetic ground state of the layered honeycomb compound Na2Co2TeO6", in Aip conference proceedings, Vol. 1942, 1 (AIP Publishing LLC, 2018), p. 130020.

[70] V. Todorova, A. Leineweber, L. Kienle, V. Duppel, and M. Jansen, "On $AgRhO_2$, and the new quaternary delafossites $AgLi_{1/3}M_{2/3}O_2$, syntheses and analyses of real structures", Journal of Solid State Chemistry **184**, 1112–1119 (2011).

[71] S. Pei, L.-L. Huang, G. Li, X. Chen, B. Xi, X. Wang, Y. Shi, D. Yu, C. Liu, L. Wang, F. Ye, M. Huang, and J.-W. Mei, "Magnetic Raman continuum in single-crystalline $H_3LiIr_2O_6$", Phys. Rev. B **101**, 201101 (2020).

[72] S. Bette, T. Takayama, K. Kitagawa, R. Takano, H. Takagi, and R. E. Dinnebier, "Solution of the heavily stacking faulted crystal structure of the honeycomb iridate $H_3LiIr_2O_6$", Dalton Transactions **46**, 15216–15227 (2017).

[73] M. Aykol, S. S. Dwaraknath, W. Sun, and K. A. Persson, "Thermodynamic limit for synthesis of metastable inorganic materials", Science Advances **4**, eaaq0148 (2018).

[74] K. Kitagawa, T. Takayama, Y. Matsumoto, A. Kato, R. Takano, Y. Kishimoto, S. Bette, R. Dinnebier, G. Jackeli, and H. Takagi, "A spin–orbital-entangled quantum liquid on a honeycomb lattice", Nature **554**, 341–345 (2018).

[75] V. Pecharsky and P. Zavalij, "Fundamentals of Powder Diffraction and Structural Characterization of Materials (2nd Version)", (2009).

[76] J. Rodríguez-Carvajal, "Recent advances in magnetic structure determination by neutron powder diffraction", Physica B: Condensed Matter **192**, 55–69 (1993).

[77] L. Finger, D. Cox, and A. Jephcoat, "A correction for powder diffraction peak asymmetry due to axial divergence", Journal of Applied Crystallography **27**, 892–900 (1994).

[78] J. Rodríguez-Carvajal, *An Introduction to the Program FullProf 2000*, 2001.

[79] B. H. Toby, "R factors in Rietveld analysis: How good is good enough?", Powder Diffraction **21**, 67–70 (2006).

[80] R. Hill and H. Flack, "The use of the Durbin–Watson d statistic in Rietveld analysis", Journal of Applied Crystallography **20**, 356–361 (1987).

[81] K. Momma and F. Izumi, "*VESTA3* for three-dimensional visualization of crystal, volumetric and morphology data", Journal of Applied Crystallography **44**, 1272–1276 (2011).

[82] Quantum Design, Inc., *Magnetic Property Measurement System®, MPMS3 User's Manual*, 2016.

[83] Quantum Design, *Physical Property Measurement System, Heat Capacity Option User's Manual*, 2004.

[84] J. Nasu, M. Udagawa, and Y. Motome, "Thermal fractionalization of quantum spins in a Kitaev model: Temperature-linear specific heat and coherent transport of Majorana fermions", Phys. Rev. B **92**, 115122 (2015).

[85] Y. Yamaji, T. Suzuki, T. Yamada, S.-I. Suga, N. Kawashima, and M. Imada, "Clues and criteria for designing a Kitaev spin liquid revealed by thermal and spin excitations of the honeycomb iridate Na_2IrO_3", Phys. Rev. B **93**, 174425 (2016).

[86] Y. Wang, G. B. Osterhoudt, Y. Tian, P. Lampen-Kelley, A. Banerjee, T. Goldstein, J. Yan, J. Knolle, H. Ji, R. J. Cava, et al., "The range of non-Kitaev terms and fractional particles in α-RuCl3", npj Quantum Materials **5**, 14 (2020).

[87] J. Chaloupka and G. Khaliullin, "Magnetic anisotropy in the Kitaev model systems Na_2IrO_3 and RuCl3", Phys. Rev. B **94**, 064435 (2016).

[88] S. A. J. Kimber, I. I. Mazin, J. Shen, H. O. Jeschke, S. V. Streltsov, D. N. Argyriou, R. Valentí, and D. I. Khomskii, "Valence bond liquid phase in the honeycomb lattice material Li_2RuO_3", Phys. Rev. B **89**, 081408 (2014).

[89] J. G. Rau, E. K.-H. Lee, and H.-Y. Kee, "Generic Spin Model for the Honeycomb Iridates beyond the Kitaev Limit", Phys. Rev. Lett. **112**, 077204 (2014).

[90] J. H. Roudebush, K. Ross, and R. Cava, "Iridium containing honeycomb Delafossites by topotactic cation exchange", Dalton Transactions **45**, 8783–8789 (2016).

[91] R. Kumar, T. Dey, P. M. Ette, K. Ramesha, A. Chakraborty, I. Dasgupta, R. Eremina, S. Tóth, A. Shahee, S. Kundu, M. Prinz-Zwick, A. A. Gippius, H. A. K. von Nidda, N. Büttgen, P. Gegenwart, and A. V. Mahajan, "Structural, thermodynamic, and local probe investigations of the honeycomb material $Ag_3LiMn_2O_6$", Phys. Rev. B **99**, 144429 (2019).

[92] R. Kumar, T. Dey, P. M. Ette, K. Ramesha, A. Chakraborty, I. Dasgupta, J. C. Orain, C. Baines, S. Tóth, A. Shahee, S. Kundu, M. Prinz-Zwick, A. A. Gippius, N. Büttgen, P. Gegenwart, and A. V. Mahajan, "Unconventional magnetism in the $4d^4$-based $S = 1$ honeycomb system $Ag_3LiRu_2O_6$", Phys. Rev. B **99**, 054417 (2019).

[93] A. Suter and B. M. Wojek, "Musrfit: A Free Platform-Independent Framework for μSR Data Analysis", Physics Procedia, 12th International Conference on Muon Spin Rotation, Relaxation and Resonance (μSR2011) **30**, 69–73 (2012).

[94] J. A. Mydosh, "Spin glasses: redux: an updated experimental/materials survey", Reports on Progress in Physics **78**, 052501 (2015).

[95] N. P. Raju, E. Gmelin, and R. K. Kremer, "Magnetic-susceptibility and specific-heat studies of spin-glass-like ordering in the pyrochlore compounds $R_2Mo_2O_7$ (R=Y, Sm, or Gd)", Phys. Rev. B **46**, 5405–5411 (1992).

[96] S. Widmann, V. Tsurkan, D. A. Prishchenko, V. G. Mazurenko, A. A. Tsirlin, and A. Loidl, "Thermodynamic evidence of fractionalized excitations in $\alpha - RuCl_3$", Phys. Rev. B **99**, 094415 (2019).

[97] A. Banerjee, P. Lampen-Kelley, J. Knolle, C. Balz, A. A. Aczel, B. Winn, Y. Liu, D. Pajerowski, J. Yan, C. A. Bridges, et al., "Excitations in the field-induced quantum spin liquid state of α-RuCl3", npj Quantum Materials **3**, 8 (2018).

[98] A. Yaouanc and P. D. De Reotier, *Muon spin rotation, relaxation, and resonance: applications to condensed matter*, 147 (Oxford University Press, 2011).

[99] F. L. Pratt, "Field dependence of μSR signals in a polycrystalline magnet", Journal of Physics: Condensed Matter **19**, 456207 (2007).

[100] Y. Li, K. Foyevtsova, H. O. Jeschke, and R. Valentí, "Analysis of the optical conductivity for A_2IrO_3 A=Na, Li from first principles", Physical Review B **91**, 161101 (2015).

[101] G. Cao and P. Schlottmann, "The challenge of spin–orbit-tuned ground states in iridates: a key issues review", Reports on Progress in Physics **81**, 042502 (2018).

[102] S. Pal, A. Seth, P. Sakrikar, A. Ali, S. Bhattacharjee, D. V. S. Muthu, Y. Singh, and A. K. Sood, "Probing signatures of fractionalization in the candidate quantum spin liquid Cu_2IrO_3 via anomalous Raman scattering", Phys. Rev. B **104**, 184420 (2021).

[103] S. K. Takahashi, J. Wang, A. Arsenault, T. Imai, M. Abramchuk, F. Tafti, and P. M. Singer, "Spin Excitations of a Proximate Kitaev Quantum Spin Liquid Realized in Cu_2IrO_3", Phys. Rev. X **9**, 031047 (2019).

[104] I. Kimchi, J. P. Sheckelton, T. M. McQueen, and P. A. Lee, "Scaling and data collapse from local moments in frustrated disordered quantum spin systems", Nature Communications **9**, 4367 (2018).

[105] Y. S. Choi, C. H. Lee, S. Lee, S. Yoon, W.-J. Lee, J. Park, A. Ali, Y. Singh, J.-C. Orain, G. Kim, J.-S. Rhyee, W.-T. Chen, F. Chou, and K.-Y. Choi, "Exotic Low-Energy Excitations Emergent in the Random Kitaev Magnet Cu_2IrO_3", Phys. Rev. Lett. **122**, 167202 (2019).

[106] W.-H. Kao, J. Knolle, G. B. Halász, R. Moessner, and N. B. Perkins, "Vacancy-Induced Low-Energy Density of States in the Kitaev Spin Liquid", Phys. Rev. X **11**, 011034 (2021).

[107] Y. Li and R. Valentí, "Role of disorder in electronic and magnetic properties of $Ag_3LiIr_2O_6$", Phys. Rev. B **105**, 115123 (2022).

[108] E. M. Kenney, C. U. Segre, W. Lafargue-Dit-Hauret, O. I. Lebedev, M. Abramchuk, A. Berlie, S. P. Cottrell, G. Simutis, F. Bahrami, N. E. Mordvinova, G. Fabbris, J. L. McChesney, D. Haskel, X. Rocquefelte, M. J. Graf, and F. Tafti, "Coexistence of static and dynamic magnetism in the Kitaev spin liquid material Cu_2IrO_3", Physical Review B **100**, 094418 (2019).

[109] A. P. Ramirez, "Strongly Geometrically Frustrated Magnets", Annual Review of Materials Science **24**, 453–480 (1994).

[110] A. A. Tsirlin and P. Gegenwart, "Kitaev Magnetism through the Prism of Lithium Iridate", physica status solidi (b) **259**, 2100146 (2022).

[111] D. Balzar, "X-ray diffraction line broadening: Modeling and applications to high-Tc superconductors", Journal of Research of the National Institute of Standards and Technology **98**, 321 (1993).

[112] J. G. Rau, E. K.-H. Lee, and H.-Y. Kee, "Spin-orbit physics giving rise to novel phases in correlated systems: Iridates and related materials", Annual Review of Condensed Matter Physics **7**, 195–221 (2016).

[113] H.-S. Kim and H.-Y. Kee, "Crystal structure and magnetism in $\alpha - RuCl_3$: An ab initio study", Phys. Rev. B **93**, 155143 (2016).

[114] S. M. Winter, Y. Li, H. O. Jeschke, and R. Valentí, "Challenges in design of Kitaev materials: Magnetic interactions from competing energy scales", Phys. Rev. B **93**, 214431 (2016).

[115] J. G. Rau, E. K.-H. Lee, and H.-Y. Kee, "Generic Spin Model for the Honeycomb Iridates beyond the Kitaev Limit", Physical Review Letters **112**, 077204 (2014).

[116] J. Chaloupka, G. Jackeli, and G. Khaliullin, "Kitaev-Heisenberg Model on a Honeycomb Lattice: Possible Exotic Phases in Iridium Oxides A_2IrO_3", Phys. Rev. Lett. **105**, 027204 (2010).

[117] B. J. Kim, H. Jin, S. J. Moon, J.-Y. Kim, B.-G. Park, C. S. Leem, J. Yu, T. W. Noh, C. Kim, S.-J. Oh, J.-H. Park, V. Durairaj, G. Cao, and E. Rotenberg, "Novel $J_{eff} = 1/2$ Mott State Induced by Relativistic Spin-Orbit Coupling in Sr_2IrO_4", Phys. Rev. Lett. **101**, 076402 (2008).

[118] S. Bhattacharjee, S.-S. Lee, and Y. B. Kim, "Spin–orbital locking, emergent pseudo-spin and magnetic order in honeycomb lattice iridates", New Journal of Physics **14**, 073015 (2012).

[119] P. A. Joy and S. Vasudevan, "Magnetism in the layered transition-metal thiophosphates MPS_3 (M=Mn, Fe, and Ni)", Phys. Rev. B **46**, 5425–5433 (1992).

[120] Y. Kobayashi, T. Okada, K. Asai, M. Katada, H. Sano, and F. Ambe, "Moessbauer spectroscopy and magnetization studies of α- and β-ruthenium trichloride", Inorganic Chemistry **31**, 4570–4574 (1992).

[121] A. Koitzsch, C. Habenicht, E. Müller, M. Knupfer, B. Büchner, H. C. Kandpal, J. van den Brink, D. Nowak, A. Isaeva, and T. Doert, "J_{eff} Description of the Honeycomb Mott Insulator α-$RuCl_3$", Physical Review Letters **117**, 126403 (2016).

[122] A. Banerjee, C. A. Bridges, J.-Q. Yan, A. A. Aczel, L. Li, M. B. Stone, G. E. Granroth, M. D. Lumsden, Y. Yiu, J. Knolle, S. Bhattacharjee, D. L. Kovrizhin, R. Moessner, D. A. Tennant, D. G. Mandrus, and S. E. Nagler, "Proximate Kitaev quantum spin liquid behaviour in a honeycomb magnet", Nature Materials **15**, 733–740 (2016).

[123] S. K. Takahashi, J. Wang, A. Arsenault, T. Imai, M. Abramchuk, F. Tafti, and P. M. Singer, "Spin Excitations of a Proximate Kitaev Quantum Spin Liquid Realized in Cu_2IrO_3", Phys. Rev. X **9**, 031047 (2019).

[124] G. Fabbris, A. Thorn, W. Bi, M. Abramchuk, F. Bahrami, J. H. Kim, T. Shinmei, T. Irifune, F. Tafti, A. N. Kolmogorov, and D. Haskel, "Complex pressure-temperature structural phase diagram of the honeycomb iridate Cu_2IrO_3", Phys. Rev. B **104**, 014102 (2021).

[125] S. K. Takahashi, J. Wang, A. Arsenault, T. Imai, M. Abramchuk, F. Tafti, and P. M. Singer, "Spin Excitations of a Proximate Kitaev Quantum Spin Liquid Realized in Cu_2IrO_3", Physical Review X **9**, 031047 (2019).

[126] V. M. Katukuri, S. Nishimoto, I. Rousochatzakis, H. Stoll, J. van den Brink, and L. Hozoi, "Strong magnetic frustration and anti-site disorder causing spin-glass behavior in honeycomb Li_2RhO_3", Scientific Reports **5**, 14718 (2015).

[127] C. R. Houska and T. M. Smith, "Least-squares analysis of x-ray diffraction line shapes with analytic functions", Journal of Applied Physics **52**, 748–754 (1981).

[128] M. Jenderka, J. Barzola-Quiquia, Z. Zhang, H. Frenzel, M. Grundmann, and M. Lorenz, "Mott variable-range hopping and weak antilocalization effect in heteroepitaxial Na_2IrO_3 thin films", Phys. Rev. B **88**, 045111 (2013).

[129] O. L. Krivanek, M. F. Chisholm, V. Nicolosi, T. J. Pennycook, G. J. Corbin, N. Dellby, M. F. Murfitt, C. S. Own, Z. S. Szilagyi, M. P. Oxley, et al., "Atom-by-atom structural and chemical analysis by annular dark-field electron microscopy", Nature **464**, 571–574 (2010).

[130] A. Amato, H. Luetkens, K. Sedlak, A. Stoykov, R. Scheuermann, M. Elender, A. Raselli, and D. Graf, "The new versatile general purpose surface-muon instrument (GPS) based on silicon photomultipliers for μSR measurements on a continuous-wave beam", Review of Scientific Instruments **88**, 093301 (2017).

[131] P. Giannozzi, S. Baroni, N. Bonini, M. Calandra, R. Car, C. Cavazzoni, D. Ceresoli, G. L. Chiarotti, M. Cococcioni, I. Dabo, et al., "QUANTUM ESPRESSO: a modular and open-source software project for quantum simulations of materials", Journal of Physics: Condensed Matter **21**, 395502 (2009).

[132] P. Giannozzi, O. Andreussi, T. Brumme, O. Bunau, M. B. Nardelli, M. Calandra, R. Car, C. Cavazzoni, D. Ceresoli, M. Cococcioni, et al., "Advanced capabilities for materials modelling with Quantum ESPRESSO", Journal of Physics: Condensed Matter **29**, 465901 (2017).

[133] M. Cococcioni and S. de Gironcoli, "Linear response approach to the calculation of the effective interaction parameters in the LDA+U method", Physical Review B **71**, 035105 (2005).

[134] M. J. van Setten, M. Giantomassi, E. Bousquet, M. J. Verstraete, D. R. Hamann, X. Gonze, and G.-M. Rignanese, "The PseudoDojo: Training and grading a 85 element optimized norm-conserving pseudopotential table", Computer Physics Communications **226**, 39–54 (2018).

[135] G. Pizzi, V. Vitale, R. Arita, S. Blügel, F. Freimuth, G. Géranton, M. Gibertini, D. Gresch, C. Johnson, T. Koretsune, J. Ibañez-Azpiroz, H. Lee, J.-M. Lihm, D. Marchand, A. Marrazzo, Y. Mokrousov, J. I. Mustafa, Y. Nohara, Y. Nomura, L. Paulatto, S. Poncé, T. Ponweiser, J. Qiao, F. Thöle, S. S. Tsirkin, M. Wierzbowska, N. Marzari, D. Vanderbilt, I. Souza, A. A. Mostofi, and J. R. Yates, "Wannier90 as a community code: new features and applications", Journal of Physics: Condensed Matter **32**, 165902 (2020).

[136] D. Haskel, "FLUO: Correcting XANES for self-absorption in fluorescence measurements", Computer program and documentation [online]. Available from http://www. aps. anl. gov/xfd/people/haskel/fluo. html (accessed January 4, 2009) (1999).

[137] E. M. Seibel, J. H. Roudebush, H. Wu, Q. Huang, M. N. Ali, H. Ji, and R. J. Cava, "Structure and Magnetic Properties of the α-NaFeO$_2$-Type Honeycomb Compound Na$_3$Ni$_2$BiO$_6$", Inorganic Chemistry **52**, 13605–13611 (2013).

[138] M. A. Laguna-Marco, D. Haskel, N. Souza-Neto, J. C. Lang, V. V. Krishnamurthy, S. Chikara, G. Cao, and M. van Veenendaal, "Orbital Magnetism and Spin-Orbit Effects in the Electronic Structure of BaIrO$_3$", Physical Review Letters **105**, 216407 (2010).

[139] G. van der Laan and B. T. Thole, "Local Probe for Spin-Orbit Interaction", Physical Review Letters **60**, 1977–1980 (1988).

[140] F. M. F. de Groot, Z. W. Hu, M. F. Lopez, G. Kaindl, F. Guillot, and M. Tronc, "Differences between L_3 and L_2 x-ray absorption spectra of transition metal compounds", The Journal of Chemical Physics **101**, 6570–6576 (1994).

[141] P. Behrens, S. Aßmann, U. Bilow, C. Linke, and M. Jansen, "Electronic Structure of Silver Oxides Investigated by AgL XANES Spectroscopy", Zeitschrift für anorganische und allgemeine Chemie **625**, 111–116 (1999).

[142] A. V. Kolobov, A. Rogalev, F. Wilhelm, N. Jaouen, T. Shima, and J. Tominaga, "Thermal decomposition of a thin AgO$_x$ layer generating optical near-field", Applied Physics Letters **84**, 1641–1643 (2004).

[143] J. P. Clancy, H. Gretarsson, J. A. Sears, Y. Singh, S. Desgreniers, K. Mehlawat, S. Layek, G. K. Rozenberg, Y. Ding, M. H. Upton, D. Casa, N. Chen, J. Im, Y. Lee, R. Yadav, L. Hozoi, D. Efremov, J. van den Brink, and Y.-J. Kim, "Pressure-driven collapse of the relativistic electronic ground state in a honeycomb iridate", npj Quantum Materials **3**, 1–7 (2018).

[144] J. A. Sears, L. E. Chern, S. Kim, P. J. Bereciartua, S. Francoual, Y. B. Kim, and Y.-J. Kim, "Ferromagnetic Kitaev interaction and the origin of large magnetic anisotropy in α-RuCl$_3$", Nature Physics **16**, 837–840 (2020).

[145] H. Gretarsson, J. P. Clancy, X. Liu, J. P. Hill, E. Bozin, Y. Singh, S. Manni, P. Gegenwart, J. Kim, A. H. Said, D. Casa, T. Gog, M. H. Upton, H.-S. Kim, J. Yu, V. M. Katukuri, L. Hozoi, J. van den Brink, and Y.-J. Kim, "Crystal-Field Splitting and Correlation Effect on the Electronic Structure of A$_2$IrO$_3$", Physical Review Letters **110**, 076402 (2013).

[146] C. Wong, M. Avdeev, and C. D. Ling, "Zig-zag magnetic ordering in honeycomb-layered Na3Co2SbO6", Journal of Solid State Chemistry **243**, 18–22 (2016).

[147] M. I. Stratan, I. L. Shukaev, T. M. Vasilchikova, A. N. Vasiliev, A. N. Korshunov, A. I. Kurbakov, V. B. Nalbandyan, and E. A. Zvereva, "Synthesis, structure and magnetic properties of honeycomb-layered Li3Co2SbO6 with new data on its sodium precursor, Na3Co2SbO6", New J. Chem. **43**, 13545–13553 (2019).

[148] E. Vavilova, T. Vasilchikova, A. Vasiliev, D. Mikhailova, V. Nalbandyan, E. Zvereva, and S. V. Streltsov, "Magnetic phase diagram and possible Kitaev-like behavior of the honeycomb-lattice antimonate $Na_3Co_2SbO_6$", Phys. Rev. B **107**, 054411 (2023).

[149] J.-Q. Yan, S. Okamoto, Y. Wu, Q. Zheng, H. D. Zhou, H. B. Cao, and M. A. McGuire, "Magnetic order in single crystals of $Na_3Co_2SbO_6$ with a honeycomb arrangement of $3d^7$ Co^{2+} ions", Phys. Rev. Mater. **3**, 074405 (2019).

[150] S. Mukherjee, G. Manna, P. Saha, S. Majumdar, and S. Giri, "Ferroelectric order with a linear high-field magnetoelectric coupling in $Na_2Co_2TeO_6$: A proposed Kitaev compound", Phys. Rev. Mater. **6**, 054407 (2022).

[151] G. Xiao, Z. Xia, W. Zhang, X. Yue, S. Huang, X. Zhang, F. Yang, Y. Song, M. Wei, H. Deng, et al., "Crystal growth and the magnetic properties of $Na_2Co_2TeO_6$ with quasi-two-dimensional honeycomb lattice", Crystal Growth & Design **19**, 2658–2662 (2019).

[152] B. H. Toby and R. B. Von Dreele, "*GSAS-II*: the genesis of a modern open-source all purpose crystallography software package", Journal of Applied Crystallography **46**, 544–549 (2013).

[153] I. Kimchi and Y.-Z. You, "Kitaev-Heisenberg-J_2-J_3 model for the iridates A_2IrO_3", Phys. Rev. B **84**, 180407 (2011).

[154] W. Yao and Y. Li, "Ferrimagnetism and anisotropic phase tunability by magnetic fields in $Na_2Co_2TeO_6$", Phys. Rev. B **101**, 085120 (2020).

[155] Y. Motome, R. Sano, S. Jang, Y. Sugita, and Y. Kato, "Materials design of Kitaev spin liquids beyond the Jackeli–Khaliullin mechanism", Journal of Physics: Condensed Matter **32**, 404001 (2020).

[156] B. Huang, Z. Liu, Y. Han, S. Zhao, M. Wu, C. E. Frank, M. Greenblatt, M. Croft, N. F. Quackenbush, S. Liu, T. A. Tyson, L. Zhang, J. Sun, P. Shan, J. Dai, X. Yu, J. Cheng, and M.-R. Li, "Nonmetallic metal toward a pressure-induced bad-metal state in two-dimensional Cu3LiRu2O6", Chem. Commun. **56**, 265–268 (2020).